3D geophysical evaluation in the course of the characterization of a municipal waste deposit site

Auteur : Debouny, Tom
Promoteur(s) : Nguyen, Frederic
Faculté : Faculté des Sciences appliquées
Diplôme : Master en ingénieur civil des mines et géologue, à finalité spécialisée en ressources minérales et recyclage
Année académique : 2018-2019
URI/URL : http://hdl.handle.net/2268.2/8320

UNIVERSITY OF LIÈGE-FACULTY OF APPLIED SCIENCES

3D GEOPHYSICAL EVALUATION IN THE COURSE OF THE CHARACTERIZATION OF A MUNICIPAL WASTE DEPOSIT SITE

GRADUATION STUDIES CONDUCTED FOR OBTAINING
THE MASTER'S DEGREE IN MINING AND GEOLOGICAL ENGINEERING
BY

DEBOUNY TOM

Supervisor : Prof. Dr. Frédéric NGUYEN
Academic year: 2018-2019

ACKNOWLEDGEMENT

Many persons deserve my deepest gratitude for their participation in the achievement of this master thesis.

First of all, I would like to thank the SPAQuE for offering me the possibility to take part in the RAWFILL project and Mr. Nonet for allowing me the access to the site. My deepest gratitude also goes to the members of the British Geological Survey for the instructive internship and especially to Dr. Arnaud Watlet for his technical support in the frame of this master thesis.

I would also like to thank all the people, without which this work would have never been achieved : Prof. Dr. Frédéric Nguyen for his availability and his mindful supervision; Itzel Isunza Manrique for her advice and expertise in the field of HVSNR and Hadrien Michel, who tries to guide me through the multiple mysteries of the inversion since my first year of master. I would also like to particularly thank Dr. David Caterina. The list of things for which he deserves my gratitude is way too long to be completely mentioned here but can be resumed as : his support during the field works, allowing me to stay hours in his office to solve the many challenges that occurred, his answer to all my silly questions and his constructive comments and corrections during the writing of this report.

In a less formal way, I would like to thank my parents and my sisters for always believing in me, even after my first year at university. I would also like to thank all my friends for sharing all the hard working moments as well as the good ones.

Last but not least, I would like to thank my girlfriend, Julie. She have been more than a mental support since the first day. Her daily motivation rubbed off on me and pushed me to work the best as I could. She also deserves most of the credits in the correction of the many English mistakes.

ABSTRACT

Due to the overconsumption and the insufficient waste management in the past, old landfills are today part of the Belgian landscapes. Besides the growing interest in old landfills from an environmental perspective, their exploitation, in terms of material extraction and reuse, perfectly adheres to the growing concept of circular economy and is further supported by the benefits coming from land recovery. The characterization of landfills is consequently becoming an operation key nowadays.

The present master thesis tends to evaluate the pertinence of three different geophysical methods for the characterization of a former landfill located in Onoz. For this purpose, 2D and 3D models of physical properties are computed. The Electrical Resistivity Tomography (ERT) and the Induced Polarization (IP) enables the detection of highly conductive lenses of lime and ashes within a layer of backfill and waste. Moreover, in the northern part of the landfill, the transition between the bedrock and the overlying waste layer is being brought to light. Unfortunately, in the southern part of the landfill, both methods show an overestimation of the highly conductive lime and ashes body, which impacts the detection of the bedrock, in the 3D models as well as in the 2D models. This limitation of the methods was expected thanks to the synthetic model previously computed, avoiding any misinterpretation even in the absence of an adequate model appraisal tool. The Horizontal to Vertical Noise Spectral Ratio (HVNSR) demonstrates different uses in the landfill characterization. Firstly, in the lower part of the site, the HVNSR is used to delineate the different waste zones by simply crossing the information from the H/V graphs obtained with the boreholes. In the upper part of the site, the HVNSR is combined with two available boreholes in order to compute the approximate average shear wave velocity of the lime and ashes. Following some assumptions, it is possible to calculate the thickness of the layers of lime and ashes, allowing the approximation of their total volume in this zone.

Keywords: Geophysics, landfill, Electrical Resistivity Tomography (ERT), Induced Polarization (IP), Horizontal to Vertical Noise Spectral Ratio (HVNSR), forward modelling.

RESUME

En raison de la surconsommation et de la gestion insuffisante des déchets dans le passé, les anciennes décharges font aujourd'hui partie intégrante du paysage belge. Outre l'intérêt croissant que suscitent les décharges d'un point de vue environnemental, leur exploitation, en termes d'extraction et de réutilisation des matériaux, s'intègre parfaitement dans le concept grandissant d'économie circulaire et s'appuie de plus sur les avantages tirés de la réhabilitation des terres. La caractérisation des décharges devient par conséquent une opération clé de nos jours.

Le présent mémoire a pour objectif d'évaluer la pertinence de trois méthodes géophysiques différentes pour la caractérisation d'un ancien site d'enfouissement situé à Onoz. Pour cela, des modèles 2D et 3D de propriétés physiques sont générés. La tomographie de résistivité électrique (ERT) et la polarisation induite (IP) permettent la détection de lentilles hautement conductrices composées de chaux et de cendres, au sein d'une couche de remblai et de déchets. De plus dans la partie nord de la décharge, la transition entre le substrat rocheux et la couche de déchets sus-jacente est mise en évidence. Malheureusement dans la partie sud de la décharge, les deux méthodes indiquent une surestimation du corps hautement conducteur de chaux et cendres, ce qui a un impact sur la détection du substrat rocheux, tant dans les modèles 3D que dans les modèles 2D. Cette limitation des méthodes était attendue grâce au modèle synthétique précédemment généré, évitant toute interprétation erronée, même en l'absence d'un outil d'évaluation de modèle adéquat. Le rapport spectral du bruit horizontal sur vertical (HVNSR) démontre différentes utilisations dans la caractérisation des décharges. Premièrement, dans la partie inférieure du site, le HVNSR est utilisé pour délimiter les différentes zones de déchets, en croisant simplement les informations obtenues à partir des graphiques H/V avec les forages. Dans la partie supérieure du site, le HVNSR est associé à deux forages disponibles, dans le but de calculer approximativement la vitesse moyenne des ondes de cisaillement de la couche de chaux ainsi que de la couche de cendres. Suivant certaines hypothèses, il est possible de calculer l'épaisseur des couches de chaux et de cendres, permettant éventuellement l'approximation de leur volume total dans cette zone.

Mots-clés: Géophysique, décharge, tomographie de résistivité électrique (ERT), polarisation induite (IP), Rapport spectral du bruit horizontal sur vertical (HVNSR), modélisation prédictive.

TABLE OF CONTENT

1 INTRODUCTION 13

1.1 Objective of the master thesis 15

1.2 Organisation of the manuscript 15

2 CHARACTERIZATION OF LANDFILLS BY GEOPHYSICAL METHODS 16

2.1 Electrical methods 16

2.1.1 The Electrical Resistivity Tomography technique (ERT) 17

2.1.2 The Induced Polarization technique (IP) 23

2.2 Data quality assessment 25

2.3 The inversion procedure 28

2.3.1 Forward model 28

2.3.2 Inverse problem 29

2.3.3 Model appraisal 32

2.4 The Horizontal to Vertical Noise Spectral Ratio technique (HVNSR) 34

3 REVIEW OF THE SELECTED METHODS FOR THE CHARACTERIZATION OF LANDFILLS 37

3.1 Electrical Resistivity Tomography technique (ERT) 37

3.2 Induced Polarization technique (IP) 38

3.3 The Horizontal to Vertical Noise Spectral Ratio technique (HVNSR) 39

4 THE CASE STUDY OF ONOZ TO ASSESS ERT/IP AND HVNSR FOR LANDFILL CHARACTERIZATION 40

4.1 Historical context of the site 40

4.2 Geological and hydrogeological context 41

4.3 Current sectorial situation 42

4.4 Previous investigations 43

5 GEOPHYSICAL SURVEY DESIGN 49

5.1 ERT/IP design 49

5.1.1 Data processing of the 3D model 51

5.1.2 Meshing 53

5.1.3 Forward model 54

5.1.3.1 Smoothness constrained model 55

5.1.3.2 Blocky inversion model 62

5.1.3.3 DOI 63

5.1.4 Data processing of the 2D models 64

5.2 HVNSR design 66

6 RESULTS AND DISCUSSION 69

6.1 Inversion of the real ERT/IP data 69

6.1.1 3D Interpretation 69

6.1.1.1 3D ERT 69

6.1.1.2 3D IP 76

6.1.1.3 3D DOI 77

6.1.2 2D interpretation 80

6.1.2.1 2D ERT 80

6.1.2.2 2D IP 82
6.1.2.3 2D DOI 83
6.2 HVNSR 85
6.2.1 Lower part 85
6.2.2 Upper part 93
7 PERSPECTIVES AND CONCLUSION 102
7.1 On the site future development 103
8 REFERENCES 105
9 ANNEXES 113
9.1 Previous investigations 113
9.1.1 Invasive investigations 113
9.1.2 FDEM mapping 115
9.1.3 ERT profiles and corresponding results 116
9.2 Parametric analyses on the forward model 118
9.3 Resulting DOI from the different types of inversion 122
9.4 HVNSR maps 123
9.5 H/V graphs of the entire measurements 124

TABLE OF FIGURES

***Figure 1**. Landfill rate of waste, excluding major mineral wastes (Generated from Eurostat, 2018)_____ 13*
***Figure 2**. Vertical section of the equipotential and current flow lines for two point sources at the surface for a homogeneous ground (Telford et al., 1990)_____ 18*
***Figure 3**. Main electrode arrays a) Wenner b) Dipole-Dipole c) Pole-Pole d) Pole-Dipole e) Wenner-Schlumberger (Loke et al., 2013) _____ 18*
***Figure 4**. Proportion of current flowing below a certain depth Z depending on the ratio of the electrodes spacing, L to the Z (Telford et al., 1990)._____ 20*
***Figure 5**. Typical electrodes arrangement for 2D survey and the relating measurements sequence (From Loke, 2016) _____ 21*
***Figure 6**. Crossline dipole-dipole measurement procedure (Modified from Van Hoorde et al., 2017)_____ 22*
***Figure 7**. Evolution of the voltage depending on time (Modified from Reynolds et al., 2011) _____ 23*
***Figure 8**. Membrane polarization mechanism (From Kearey et al., 2002) _____ 24*
***Figure 9**. Electrode polarization mechanism (From Kearey et al., 2002)_____ 25*
***Figure 10**. Error model (Slater et al., 2000) _____ 27*
***Figure 1**1. Error model (Koestel et al., 2008) _____ 27*
***Figure 12**. Representation of the forward and inverse problem (From Binley & Kemna., 2005) _____ 28*
***Figure 13**. Typical HVNSR graph (From Oubaiche et al., 2002) _____ 35*
***Figure 14.** Aerial photo of the site in 1963 (Adapted from Verdi, 1995) _____ 40*
***Figure 15**. Aerial photo of the site in 1976 (Modified from Verdi, 1995)_____ 41*
***Figure 16**. DEM of the studied zone (Modified from Service Public de Wallonie, 2018)_____ 42*
***Figure 17**. Sectorial plan around the site. The extension of the site is delimited in blue, the purple area represents the mix economic activities zone, while the light green represents the green area zone (Adapted from Service Public de Wallonie, 2018) _____ 43*
*F**igure 18**. Location of the cross-sections of the conceptual model (Adapted from Service Public de Wallonie, 2017) _____ 47*
*F**igure 19**. Cross-sections of the conceptual model (Modified from Verdi, 1995) _____ 48*
***Figure 20**. Aerial view of the site showing the configuration of the four ERT profiles (Adapted from Service Public de Wallonie, 2018)_____ 49*
***Figure 21**. Example of crossline measurements between two lines of the protocol used for the ERT measurements_____ 50*
***Figure 22**. Histogram of the variance of each measurement given the ABEM Terrameter LS _____ 51*
***Figure 23**. Histogram of the reciprocal relative errors_____ 52*
***Figure 24**. Error model following Slater's model _____ 52*
***Figure 25**. Generated mesh for the inversion _____ 54*
***Figure 26**. Numerical model used for the forward modelling _____ 55*
***Figure 27**. North to South cross-section of the forward model _____ 55*
***Figure 28**. Results of the smoothness constraint inversion of the synthetic data. **(A)** Global vision of the resistivity distribution **(B)** cross-section along the dashed line of (A). The dashed line rectangles inside the cross-section indicates the position of the highly conductive lenses and the bedrock and are displayed to get a better idea of the reconstruction of the lenses._____ 56*
***Figure 29.** Application of a maximum resistivity threshold of 250 Ω.m on the model (zone in blue), **(A)** shows the horizontal extension, **(B)** the vertical extension _____ 57*
***Figure 30**. Results of the smoothness constraint inversion of the synthetic data with implementation of the error model. **(A)** Global vision of the resistivity distribution **(B)** cross-section of the dashed line of **(A)**. The dashed line rectangles inside the cross-section indicate the position of the highly conductive lenses and the bedrock and are displayed to get a better idea of the reconstruction of the lenses. _____ 58*
***Figure 31**. Results of the smoothness constraint inversion of the synthetic data with implementation of the error model. **(A)** Global vision of the resistivity distribution **(B)** cross-section of the dashed line of **(A)**. The dashed line rectangles inside the cross-section indicate the position of the highly conductive lenses and the bedrock and are displayed to get a better idea of the reconstruction of the lenses. _____ 59*
***Figure 32**. Evolution of the resistivities of the model depending on the resistivity of the two highly conductive layers _____ 61*

***Figure 33**. Cross-section of the inversed synthetic model obtained from a blocky inversion. The dashed line rectangles inside the cross-section indicate the position of the highly conductive lenses and the bedrock and are displayed to get a better idea of the reconstruction of the lenses. _____ 63*
***Figure 34**. Methodology applied for the obtention of the best dataset for the 2D inversion, using P1 as example _____ 65*
***Figure 35**. Position of the different HV measurements in Onoz (adapted from Service Public de Wallonie, 2018) _____ 66*
***Figure 36**. Map of the delineation of the waste in the upper part of Onoz landfill based on the FDEM results (Adapted from Caterina et al., 2019) _____ 68*
***Figure 37**. Resulting resistivity images of the inversion of the real dataset. **(A)** Global vision of the resistivity distribution **(B)** cross-section of the dashed line of **(A)**. Borehole F12 was made in 2012 and trench T1 in 2018 70*
***Figure 38**. Histogram of the resistivities occurring in the model of Onoz _____ 70*
***Figure 39**. Photography of the surficial lime occurring in the central part of the survey in Onoz _____ 71*
***Figure 40**. Resulting resistivity images of the "blocky" inversion of the real dataset. **(A)** Global vision of the resistivity distribution **(B)** cross-section of the dashed line of **(A)**. Borehole F12 was made in 2012 and trench T1 in 2018 _____ 72*
***Figure 41**.Histogram of the resistivities occurring in the blocky model of Onoz _____ 73*
***Figure 42.** Application of a maximum resistivity threshold of 40 Ω.m on the mode from the smoothed inversion (zone in blue), **(A)** shows the horizontal extension, **(B)** the vertical extension _____ 74*
***Figure 43.** Application of a maximum resistivity threshold of 40 Ω.m on the model from the blocky inversion (zone in blue), **(A)** shows the horizontal extension, **(B)** the vertical extension _____ 74*
***Figure 44**. Comparison of the lateral extension given by the ERT and the FDEM surveys at a depth of 0.5 m (Adapted from Caterina et al., 2019). _____ 75*
***Figure 45**. Comparison of the lateral extension given by the ERT and the FDEM surveys at a depth of 2.5 m (Adapted from Caterina et al., 2019). _____ 75*
***Figure 4**6. Coverage of the FDEM survey (Adapted from Service Public de Wallonie, 2018) _____ 76*
***Figure 47**. 3D IP model performed using BERT _____ 77*
***Figure 48**. Resistivity model from an blocky inversion enforced by a reference model of 5 000 Ω.m _____ 78*
***Figure 49**. DOI from the smoothness constrained inversion _____ 78*
***Figure 50**. DOI from the blocky constrained inversion _____ 79*
***Figure 51**. Resistivity models obtained after inversion of in-line measurement for **(A)** P1 **(B)** P2 (C) P3 (D) P4 _ 80*
***Figure 52**. Resistivity profiles obtained from cross-sections of the 3D model corresponding to the 2D profiles for (A) P1 (B) P2 (C) P3 (D) P4 _____ 81*
***Figure 53**. Chargeability models obtained after inversion of in-line measurement for **(A)** P1 **(B)** P2 (C) P3 (D) P4 _____ 82*
***Figure 54**. Normalized Chargeability models obtained after inversion of in-line measurement for **(A)** P1 **(B)** P2 (C) P3 (D) P4 _____ 83*
***Figure 55**. DOI of profile **(A)** 1 **(B)** 2 (C) 3 (D) 4 _____ 84*
***Figure 56**. HVNSR measurements map of the lower part and representative graphs of the different zones (Adapted from Service Public de Wallonie, 2018) _____ 85*
***Figure 57**. Comparison of the HVNSR curve of measurement 185 and the closest trench (Modified from RECOsol, 2012) _____ 86*
***Figure 58**. HVNSR curve for measurements 172 and 174 _____ 86*
***Figure 59**. Comparison of the HVNSR curve of measurement 162 and the closest boreholes (Modified from IRCO, 2018) _____ 87*
***Figure 60**. Comparison of the HVNSR graph of measurement 150 and the closest trench (Modified from RECOsol, 2012) _____ 88*
***Figure 61**. Comparison of the HVNSR graph of measurement 142 and the closest trench (Modified from RECOsol, 2012) _____ 88*
***Figure 62**. Comparison of the HVNSR graph of measurement 169 and the closest trench (Modified from RECOsol, 2012) _____ 89*
***Figure 63**. Map of the 3D HVNSR profiles displayed for the lower part (Adapted from Service Public de Wallonie, 2018) _____ 90*
***Figure 64.** HVNSR cross-section **(A)** corresponding to the cross-section displayed during the ERT interpretation **(B)** _____ 91*
***Figure 65**. HVNSR profile of the measurements performed previously by the geophysical team of ULiège and myself _____ 92*

***Figure 66**. HVNSR perpendicular profile _____ 93*
***Figure 67**. HVNSR measurements map of the upper part and representative graphs of the different zones (Adapted from Service Public de Wallonie, 2018) _____ 94*
***Figure 68**. HVNSR graph of measurement 156 compared to the scheme of the corresponding boreholes _____ 94*
***Figure 69**. HVNSR graph of measurement 157 compared to the scheme of the corresponding boreholes _____ 95*
***Figure 70**. HVNSR graph of measurement 189 _____ 95*
***Figure 71**. HVNSR graph of measurement 195 _____ 96*
***Figure 72**. HVNSR graph of measurement 200 _____ 97*
***Figure 73**. Map of the 3D HVNSR profiles displayed for the upper part (Adapted from Service Public de Wallonie, 2018) _____ 97*
***Figure 74**. HVNSR profile in the north-south direction in the upper part of the site _____ 98*
***Figure 75**. HVNSR profile in the east-west direction in the upper part of the site _____ 98*
***Figure 76**. Location of the two cross-sections used as conceptual model. _____ 100*
***Figure 77**. W-E cross-section _____ 101*
***Figure 78**. N-S cross-section _____ 101*
***Figure 79**. Map from the previous invasive investigations (Adapted from Service Public de Wallonie, 2018) _ 113*
***Figure 80**. Borehole n° 4 (Adapted from IRCO, 2018) _____ 113*
***Figure 81**. Borehole n° 4 (Adapted from IRCO, 2018) _____ 114*
***Figure 82**. Map of both EM campaigns (Adapted from Caterina et al, 2019) _____ 115*
***Figure 83**. Map of the ERT profiles from 2018 (Adapted from Caterina et al., 2019) _____ 116*
***Figure 84**. Results of the ERT profiles from 2018 (From Caterina et al., 2019) _____ 117*
***Figure 85**. Results of the parametric analysis, considering a change in the thickness of the conductive layers 118*
***Figure 86**. Results of the parametric analysis, considering a change in the resistivity of the conductive layers 119*
***Figure 87**. Resulting model for a relative weight of 0.5 _____ 120*
***Figure 88**. Resulting model for a relative weight of 0.2 _____ 120*
***Figure 89**. Resulting model for a relative weight of 0.1 _____ 121*
***Figure 90**. DOI of the smooth constrained inversion _____ 122*
***Figure 91**. DOI of the inversion applied with a relative of 0.2 _____ 122*
***Figure 92**. DOI of the blocky inversion _____ 122*
***Figure 93**. Map of the HVNSR measurements in the lower part of the site (Adapted from Service Public de Wallonie, 2018) _____ 123*
***Figure 94**. Map of the HVNSR measurements in the upper part of the site (Adapted from Service Public de Wallonie, 2018) _____ 123*
***Figure 95**. H/V graphs of the HVNSR measurements in the lower part of the site _____ 126*
***Figure 96**. H/V graphs of the HVNSR measurements in the upper part of the site _____ 128*

LIST OF TABLES

***Table 1**. Names of the main electrode configuration and their geometric factor calculation (adapted from Loke et al., 2013) _____ 19*
***Table 2**. Recording recommendations (Modified from SESAME, 2004)_____ 36*
***Table 3**. Summary of the methods used in the frame of this mater thesis and their main purposes in landfills characterization_____ 37*
***Table 4**.Contaminants found in the different wastes in Onoz, with TV, LV and VI being respectively the Threshold Value, the Limit Value and the Value of Intervention (Generated from IRCO, 2018) _____ 46*
***Table 5**. Number of measurements used for each 2D profiles_____ 65*
***Table 6**. Thickness calculated from the HVNSR measurements_____ 99*

LIST OF ABBREVIATIONS

AC = Alternative Current
BERT = Boundless Electrical Resistivity Tomography
BGS = British Geological Survey
CST = Constant Separation Traversing
DC = Continuous Current
DEM = Digital Elevation Model
DOI = Depth of Investigation Index
ELFM = Enhanced Landfill Mining
ERT = Electrical Resistivity Tomography
EU = European Union
FDEM = Frequency Domain Electromagnetic induction
GBI = Great Biological interest
H/V = Horizontal to Vertical ratio
HVNSR = Horizontal to Vertical Noise Spectral Ratio
IP = Induced Polarization
IRLS = Iteratively Reweighted Least Squares
LTA = Long Term Average
LV = Limit Value
MASW = Multichannel Analysis of Surface Wave
PAH = Polycyclic Aromatic Hydrocarbon
PCB = Polychlorinated biphenyl
RMSE = Root Mean Square Error
SESAME = Site Effects using Ambient Excitations
SNCB = Société Nationale des Chemins de fer Belges
SPAQuE = Société Publique d'Aide à la Qualité de l'Environnement
SPW = Service Public de Wallonie
STA = Short Term Average
S-wave = Shear wave
TDIP = Time-Domaine Induced Polarization
TOC = Total Organic Carbon
TV = Threshold Value
ULiège = Université de Liège
VES = Vertical Electrical Sounding
VI = Value of Intervention
VOHC = Volatile Organic Halogenated Hydrocarbon

1 INTRODUCTION

Today, old landfills are part of the Belgian landscapes. Due to the overconsumption and the insufficient management of wastes in the past, they flourished in many different areas. Landfills can be considered as potential threats for the environment, due to the contaminants they may contain which may potentially affect natural resources and/or human health. Another important aspect is that, part of what was previously considered as waste, can nowadays be reused in many domains thanks to the development or adaptation of recycling technologies, especially in terms of sorting (Sigmund, 2018). Therefore, there is a growing interest in landfills from an economical and environmental perspective.

The council directive 1999/31/EC defines landfills as "*a waste disposal site for the deposit of waste onto or into land, including internal waste disposal sites and a permanent site which is used for temporary storage of waste*". Landfills can be separated into three different classes, respectively hazardous, non-hazardous and inert waste. Furthermore, choosing a location for a new landfill must take different criteria into account, such as the distance between the site and residential and recreation areas, water bodies and other agricultural or urban sites. A special attention should also be paid to the existence of nature protection zones, to the geological and hydrogeological conditions, to the risk of flooding or landslides on the sites and to the protection of the cultural patrimony in the area (The Council of the European Union, 1999).

The European directives led to a decreased number of operating landfills as well as to the reduction of the environmental impacts of such operation (Hogland et al., 2011). Focusing on the volume percentage of waste landfilled between 2010 and 2014 in EU countries, (excluding major mineral wastes) (***Figure 1***), it can be highlighted that the percentage is, on average, decreasing for the Europe of the 28 member states. It should also be underlined that Belgium is one of the exemplary countries with a percentage of only 3% in 2014 (Eurostat, 2018).

Figure 1. Landfill rate of waste, excluding major mineral wastes (Generated from Eurostat, 2018)

The number of landfill sites in Europe has been estimated between 150 000 and 500 000 (Jones et al., 2013). Around 90% of these are considered as non-sanitary, meaning that they could possibly be considered as future environmental threats and would require drastic and expensive remediation improvements. Although this situation appears to be problematic and complex, it may represent a great opportunity if the chosen remediation strategy is combined with a resource recovery. This could reduce the remediation costs and allow to reclaim valuable land, but also to recover a large amount of valuable resources contained in landfills (Särkkä et al., 2018). Indeed, it has been estimated that the recovery of these resources could provide economic revenue for the rehabilitation project, while depending on the quality of the separated fraction, the local situation and the market (Hogland et al., 2011). In fact, although the environmental considerations should prevail in theory, the economic aspect is often at stake in practice. It is necessary for such projects to be economically viable or to be driven by political will in order to attract private companies to invest. Nowadays, many studies have highlighted the difficulty to reach a financial profit in the mining of landfill sites and that projects have to be cautiously selected (Van Passel et al., 2013; Winterstetter et al., 2015). It has been previously determined that for an optimal material recovery, projects should focus on landfills that operated between 1960 and 1995 (Hogland et al., 2011). This represents between 3 300 * 10^6 and 11 000 * 10^6 tons of available material in the EU, which could constitute around 5% of the yearly consumption of the EU in terms of non-energy, non-food materials and minerals, during 25 years (Jones et al., 2013).

Furthermore, the exploitation of historic landfill sites perfectly adheres to the growing concept of circular economy and, in this perspective, different landfill mining strategies are currently being developed. Jones et al., (2013) subdivided these strategies into two main categories. The first category is the *in situ* landfill mining. It refers to recovery activities not necessitating the excavation of the waste. With this type of strategy, methane can be extracted, water and soil contaminants can also be eliminated. The second category is the *ex situ* landfill mining, involving the partial or full excavation of the waste. One important concept, part of the ex situ strategy, is the “Enhanced Landfill Mining” (ELFM), which combines the valorization of landfilled waste as material as well as energy. It achieves this goal bearing in mind strict environmental and social criteria. The social criterion has been underestimated in the past, but is now fully considered, with the fact that the support of local communities plays a crucial role in this type of project. The ELFM concept can be applied on historic landfill as well as on future ones. Indeed, it is important to understand that today’s waste could be considered as valuable material in a near future. In fact, it is highly conceivable that next generation technologies will be developed, enabling the recycling of materials, which are nowadays considered as non-recyclable due to technological or economic limitations (Jones et al., 2013).

Whether environmental or economic interests are at stake, characterization of landfills is a key operation to forecast the sustainability of landfill mining operations. The types of waste and their amount need to be estimated along with their uncertainties. Their localization should also be determined. It is also important to assess their potentiality of recovery and their treatability for further valorization (Särkkä et al., 2018). Unfortunately, this information is lacking for most of historic landfills and this is where invasive and non to minimally invasive geophysical techniques intervene. Invasive methods based on drilling/trenching, sampling and analyzes have been used

for a long time. Nevertheless, even if they provide direct and analytic information, their spatial coverage or representability are not optimal. They can become costly and can also be the cause of an added threat to the environment, for example by breaking impervious liners while conducting boreholes or trenches. It has been acknowledged that noninvasive geophysical methods might help with the decision of the drilling location and might also provide broader indirect information on the internal properties, such as composition, temperature, humidity, density or compaction of the waste material, while being also less costly (Nguyen et al., 2018). It can also help to determine the precise extension of a landfill (Dumont et al.,2017). The waste occurring in landfills often show the same type of characteristics, such as low seismic wave propagation and low electrical resistivity (Dumont et al., 2017). These aspects will be further developed in ***chapter 2 and 3***.

1.1 Objective of the master thesis

The aim of the thesis is to evaluate the pertinence of three different non-invasive geophysical techniques, that already proved their robustness, for the characterization of a former landfill. For this purpose, 2D and 3D models of physical properties will be computed, in order to enable the comparison between the different techniques and to establish a conceptual model thanks to the cross-measurements. The probable heterogeneity encountered in landfills renders the computation of 3D models practically unavoidable, while 2D models are mainly used for a comparison, validating the results obtained during the 3D modelling. Two electrical measurement methods , i.e. Electrical Resistivity Tomography (ERT) and Induced polarization (IP), and the Horizontal to Vertical Noise Spectral Ratio (HVNSR), were performed in the frame of this thesis. To perform the comparison, a former limestone quarry in Onoz, small village situated in the province of Namur, in Wallonia, will be investigated.

1.2 Organisation of the manuscript

The first part (***chapter 2 and 3***) will contextualize the problem of landfills in Europe, describe theoretically the different geophysical methods used and underline their applications in landfills. The second part describes a case study: Onoz and the previous investigations performed in this landfill (***Chapter 4***). Thereafter, the methodology of the surveys performed in Onoz during the master thesis will be reviewed (***Chapter 5***), followed by the presentation and the interpretation of results (***Chapter 6***). Finally, a conclusion with the different perspectives of the landfill site and the applications of geophysical methods in landfill characterization will complete this report (***Chapter 7***).

2 CHARACTERIZATION OF LANDFILLS BY GEOPHYSICAL METHODS

Several studies have recently investigated and assessed the usefulness of multiple geophysical techniques for the characterization or monitoring of old landfills (e.g. Dumont et al., 2017; Balia, 2018; Di Maio et al., 2018). Geophysical methods often enable to delineate properly the extension of the landfill and to gather information on the physiochemical properties of the inner material as well as on the potential pollution plume due for example to leachate formed from a degradation process on the discarded materials (Soupios & Ntarlagiannis, 2017). The gravimetric method is an acknowledged technique for the identification of the external boundaries of old landfills. Seismic techniques are useful to get a better insight of the thickness and compaction of the waste, while electrical methods can be used to determine the moisture content and the presence of leachate (Di Maio, 2018). Magnetic and electromagnetic methods are suitable to rapidly identify the lateral extension of the landfills.

In this master thesis, only electrical and one seismic methods were developed and the following sections (***Sections 2.1*** and ***2.4***) will aim to lay the foundation for an optimal understanding of these methods and their use in the characterization of landfills. Besides their ease of use in the field and their robustness, the selected methods have already proven their value in landfill characterization. Indeed, different types of waste and pollution plumes often present distinctive differences in their resistivity or chargeability, to which electrical methods are sensitive. Seismic techniques also have already proven to be useful in the characterization of waste deposits (Soupios & Ntarlagiannis, 2017). The relationship demonstrated between the resonance frequency of a soil determined during HVSNR measurements and its thickness has already been established (Delgado et al., 2000) and could be interesting to be applied in the current context of landfill.

2.1 Electrical methods

Electrical techniques are routinely used in environmental geophysics. They allow estimating the electrical properties of the subsurface in a minimally invasive way at the soil surface. The electrical properties depend on several factors. Indeed, besides being related to the mineral composition and the rock porosity, they also depend on fluid content and water saturation (Loke, 2018). Two techniques are presented: “Electrical Resistivity Tomography” (ERT) and “Time-Domain Induced Polarization” (TDIP or IP). Both need an injection of electrical current into the ground through one or two electrodes and the measure of the electrical potential at one or two other electrodes. ERT makes use of the potential measured during the current injection to determine the subsurface electrical resistivity distribution. IP uses the decay of the electrical potential after the current injection to determine the subsurface chargeability distribution (ADEME et al, 2016).

2.1.1 The Electrical Resistivity Tomography technique (ERT)

The constitutive equation in the field of electrical surveys is the Ohm's law. In a continuous medium, the current flow equation based on the Ohm's law in vector form is the following (***equation 1***):

$$\boldsymbol{J} = \sigma \boldsymbol{E} \qquad (1)$$

Where **J**, σ, **E** represent, the current density (A.m^{-2}), the conductivity of the medium (S.m^{-1}) and the intensity of the electric field (V.m^{-1}) respectively. In ERT, the resistivity of the medium (ρ), which is the reciprocal of the conductivity and is expressed in Ω.m, is mostly used, leading to ***equation 2***.

$$\boldsymbol{J} = \frac{1}{\rho} \boldsymbol{E} \quad (2)$$

As previously mentioned, during an ERT acquisition, the electric potential is measured at discrete points, i.e. electrodes, and is related to the intensity of the electric field following ***equation 3*** (Loke, 2018). For the ERT method, in order to avoid any polarization, an alternating power source is employed. Commonly, the current waveform is a switched square wave and is applied in an interval of frequencies from 0.5 to 2 Hz. Such waveform allows to remove the drift induced by the self-potential voltage (Binley & Kemna, 2005).

$$E = -\nabla \mathrm{V} \quad (3)$$

It has been shown that in a homogeneous half-space and with a single point as current source at the ground surface, the current will flow radially away from the source. Furthermore, the potential will vary inversely with the distance, following ***equation 4***.

$$\mathrm{V} = \frac{\rho I}{2 \pi r} \quad (4)$$

Where I is the current injected through the source (in A) and r is the distance from a point in the medium to the source (in m).

In case of two current electrodes (modelled as two point sources), the spherical potential distribution will be distorted, mainly between the two electrodes (***Figure 2***) (Telford et al., 1990). The calculation of the potential will be given by ***equation 5***, where r_{C1} and r_{C2} are the distances from the chosen point to both current electrodes (Loke, 2018).

$$\mathrm{V} = \frac{\rho I}{2 \pi} \left(\frac{1}{r_{C1}} - \frac{1}{r_{C2}} \right) \qquad (5)$$

The inverse of the expression within the brackets time 2π, can be replaced by k, which is the so-called geometric factor, which accounts for the arrangement of the electrodes (Daily et al., 2005). Thereupon, knowing the position of the electrodes, the current injected and the resulting electric potential, it is possible to compute the apparent resistivity following ***equation 6*** (Loke et al., 2013).

$$\rho_a = k \frac{\mathrm{V}}{I} \qquad (6)$$

Except for a homogenous surface, the apparent resistivity is not the true resistivity. The inversion problem represents the capability of computing the true resistivity from the apparent one (Loke, 2018).

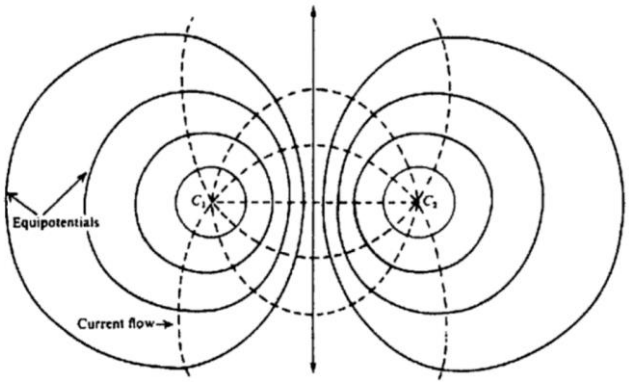

Figure 2. Vertical section of the equipotential and current flow lines for two point sources at the surface for a homogeneous ground (Telford et al., 1990)

As already discussed, during an electrical survey, measurements are often taken in a "quadrupole", with a pair of current electrodes and a second pair of potential electrodes. In this case, the geometric factor "k" depends on the configuration of the four electrodes. Different types of array have been used over the years and they not only have an impact on the geometric factor but also on the maximal depth of investigation, the sensitivity and on the intensity of the signal (ADEME et al, 2016). ***Table 1*** summarizes the main electrode arrays and the formula used to compute the geometric factor, while ***figure 3*** shows their configuration, with "a" representing a distance between two neighboring electrodes and "n", a multiplying factor. "C" represents the current electrodes and "P" indicates the potential electrodes.

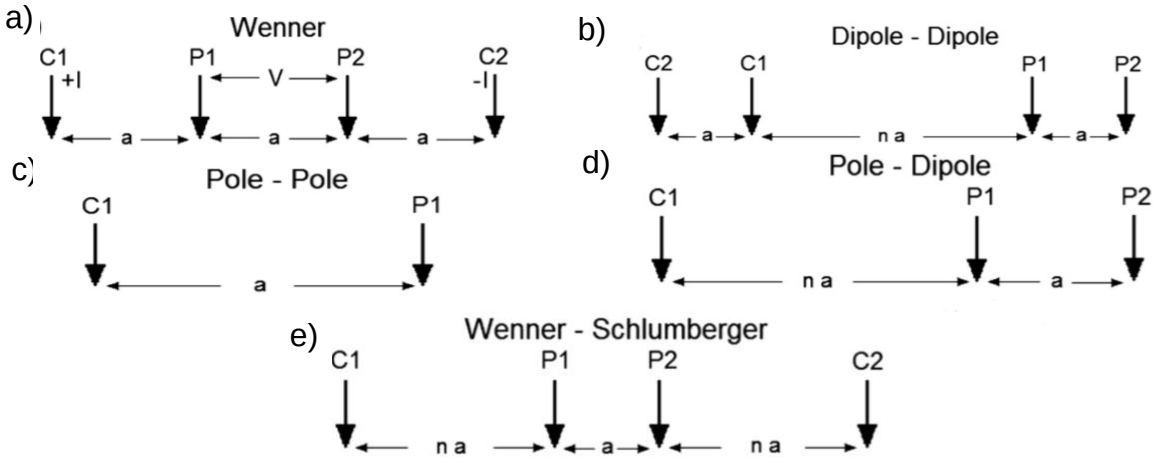

Figure 3. Main electrode arrays a) Wenner b) Dipole-Dipole c) Pole-Pole d) Pole-Dipole e) Wenner-Schlumberger (Loke et al., 2013)

Table 1. Names of the main electrode configuration and their geometric factor calculation (adapted from Loke et al., 2013)

CONFIGURATION NAME	K FORMULA
Wenner	k = 2πa
Dipole-Dipole	k = π na (n+1) (n+2) (n+3)
Pole-Pole	k = 2πa
Pole-Dipole	k = 2π na (n+1) (n+2)
Wenner-Schlumberger	k = π na (n+1) (n+2)

Understandably, advantages and drawbacks can be found for each type of configurations. The Wenner configuration (***Figure 3A***) is suitable in noisy environments due to its large signal (low k). It is also highly sensitive to vertical variations, while less sensitive to horizontal variations in the resistivity. The mean depth of investigation is approximately the half of the span between the current electrodes, which is modest compared to other configurations. The dipole-dipole configuration (***Figure 3B***) is less appropriate when the environment is considered as noisy (due to rapid increase of k for large 'n' values). Furthermore, it sometimes has a higher spatial resolution than the Wenner configuration (Dahlin & Zhou, 2004). In contrast to the Wenner configuration, it is less sensitive to vertical variations but more sensitive to horizontal variations. In addition, it offers a good horizontal resolution. The pole-pole configuration (***Figure 3C***), which is not a quadrupole method, is also less suited for noisy environments and has the lowest resolution in both horizontal and vertical directions. The advantages of the method are a greater depth of investigation and a high horizontal coverage within the subsurface. The pole-dipole configuration (***Figure 3D***), which is only composed of three electrodes is less sensitive to environmental noises than the pole-pole array. It is also sensitive to vertical variations. The depth of investigation is often slightly better to the one of Wenner configuration. One of its main drawbacks is the difficulty of setup due to the extensive distance needed between the electrodes (also the case for the pole-pole configuration). The last presented configuration is the Wenner-Schlumberger (***Figure 3E***). This configuration has many advantages with a high sensitivity to horizontal as well as vertical variations. The depth of investigation is comparable to the one of the pole-dipole configuration. The concept of depth of investigation is not absolute. Indeed, it depends on the true distribution of the subsurface resistivity regarding all the arrays. Therefore, in highly heterogeneous environments such as landfills, it is important to bear in mind that the most important criterion for the selection of arrays, is probably the sensitivity. For each method, the larger the distance between the electrodes, the greater the depth of investigation, but also, the lower the measured signal and the resolution (Loke, 2018). ***Figure 4*** shows how the proportion of current reaching a given depth "Z" compared to the ratio of the current electrodes separation (L) to Z evolves in a homogenous ground. The current electrodes separation should be at least equal to the depth, which represents a proportion of the current flow around 30%. This should permit to reach the requirements to adequately energize the ground at the required depth. This implies that one of the practical limits of the resistivity methods is laying long cables generating enough power to reach a higher depth of investigation (Kearay et al., 2002).

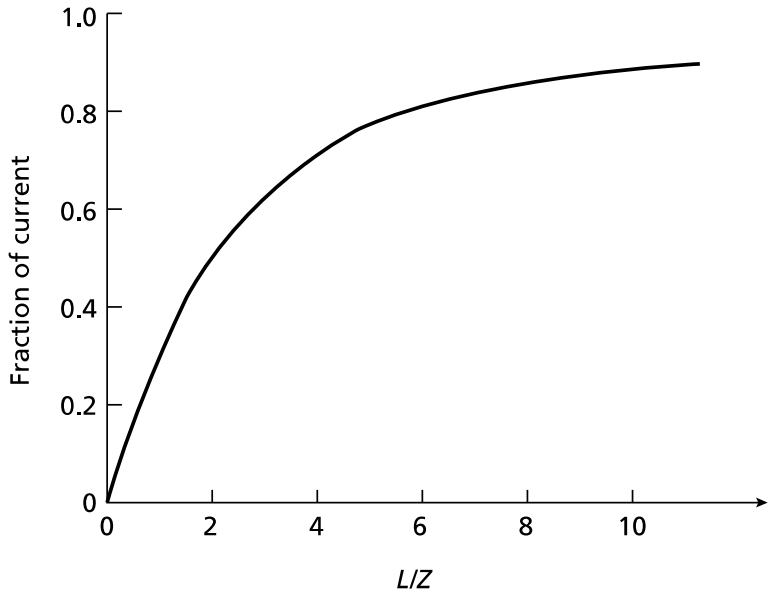

Figure 4. Proportion of current flowing below a certain depth Z depending on the ratio of the electrodes spacing, L to the Z (Telford et al., 1990).

Until the late 1980's, geoelectrical measurements implied mainly Vertical Electrical Sounding (VES) and Constant Separation Traversing (CST) using only 2 to 4 electrodes. The development of multi-electrodes systems enabled 2D imaging surveys, which somehow combine the information provided by the aforementioned methods in an automated way. In these systems, the connection of all the electrodes to the resistivity meter is made possible by a multi-core cable. Usually, it is appropriate to keep the electrodes equally spaced all along the profile. It is possible to directly import a tailor-made survey file with, for example, the sequence of measurements, the type of array used and a specified amplitude of current. The internal program of the system will then automatically select the appropriate electrodes for the measurements. Almost all types of array configurations mentioned previously can be used within these systems (Loke et al., 2013). ***Figure 5*** shows a typical arrangement of a 2D survey and the linked sequence of measurements for 20 electrodes using a Wenner configuration. In the present case, the first data acquisition will consist in taking all the possible measurements with an electrode spacing of 1a, with "a" being the space between neighboring electrodes. The first acquisition will use electrodes 1 and 4 as current electrodes, while the electrodes 2 and 3 will measure the potential. The next acquisition step simply consists in switching to the next electrodes in the sequence, i.e. an injection of current through electrodes 2 and 5, and a measure of potential at electrodes 3 and 4. When all the measurements with spacing of 1a are performed, a 2a spacing sequence is achieved following a similar pattern. The survey will continue until the last acquisition, consisting of a 6a spacing sequence (Loke, 2018).

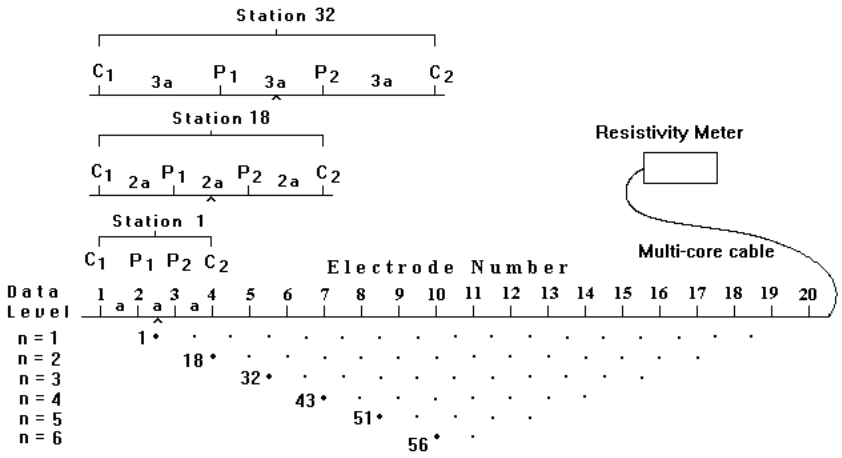

Figure 5. Typical electrodes arrangement for 2D survey and the relating measurements sequence (From Loke, 2016)

Nowadays, acquisition along a profile is probably the most widely used type of acquisition as it offers a good spatial coverage (both in horizontal and vertical directions) at reasonable cost. However, it is based on a strong assumption that the geological structures do not vary in the direction perpendicular to the set-up line. Obviously, this is not always valid (Loke et al., 2013), particularly in heterogeneous environments such as landfills. One way to bypass this limitation is to set up a grid with multiple 2D survey lines in different directions (Di Maio et al., 2018), even in very unusual shapes such as “stars” (Clément et al, 2011). Another possible method, called the “quasi-3D manner”, consists in collecting the measurements in 2D mode and to invert the data with a 3D software (Rucker et al., 2009). However, more and more surveys are now directly carried out in 3D mode which is made possible by the development of multichannel systems reducing drastically acquisition time. However, 3D surveys remain more expensive and time consuming than 2D surveys (Rucker et al. 2009) and are consequently used only when the heterogeneity of the site requires it (Bentley & Gharibi, 2004). An indication of the heterogeneity can be provided by historical information, previous invasive or geophysical surveys. In 3D, the electrodes used can be either placed randomly in space or placed in well-designed grids, which often consist in parallel lines of electrodes. The main difference with 2D surveys is the complementary acquisition of crossline measurements, with the current electrodes in one line while the potential electrodes are within another line (Dahlin et al., 2002). The survey coverage is often limited by the fact that instruments are only able to deal with a certain number of electrodes, typically between 64 and 128 (Maurya et al., 2017). To cope with this limitation, different strategies have been adopted. One of them is called the “maximum yield grid”. It is designed in such a way that the number of electrodes used for data acquisition is minimized without a loss of resolution, which is also useful on vulnerable surfaces (Fiandaca et al., 2010). Another developed method is the so-called “roll-along methodology”, where 2D measurements and crossline measurements are simultaneously acquired. For this purpose, several parallel lines are set up and when the entire data acquisition from the first line is finished, it can be removed and placed once again parallel to the last line (Dahlin et al., 2002). This enables the reduction of acquisition time but also limits the amount of acquired data. Van Hoorde et al., (2017) proposed a more complex procedure based on the roll-along methodology consisting in acquiring more crossline measurements in different direction in order to increase the size of the final dataset (***Figure 6***).

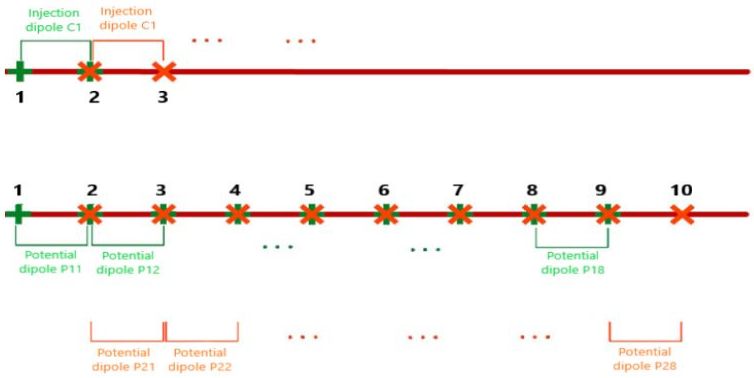

Figure 6. Crossline dipole-dipole measurement procedure (Modified from Van Hoorde et al., 2017)

It is possible that spatial constraints due to natural or anthropogenic obstacles render the deployment of usual 3D settings impossible, especially in environments such as landfills, where the vegetation or waste could limit the access to certain locations. This can be overcome by designing a special acquisition procedure. Chavez et al., (2018) invented one of these tailor-made procedures to investigate the subsoil under pyramids, using three different types of array and this had led to promising results. Concerning the electrodes arrays, they are the same as for 2D surveys most of the time. Rucker et al., (2009) summarized many 3D surveys in the literature and showed that the most suitable arrays for pure 3D data acquisition were the pole-pole, the pole-dipole and the dipole-dipole configurations. Moreover, it has been demonstrated that the combination of different configurations could show interesting results. Indeed, Chamber et al., (2006) combined the Wenner and Schlumberger techniques to benefit from both the right signal strength of the Wenner array and the superior lateral resolution of the Schlumberger array. Chavez et al., (2018) used a combination of three arrays using the Wenner-Schlumberger-perimeter methodologies to cover the external part as well as a Minimum Coupling to retrieve information in deeper parts and finally a Wenner-Schlumberger gradient to get information of the central portion below the pyramid.

The difficulty to access a survey zone and the choice of the most suited configuration are not the only limitations that a geophysicist may encounter when designing an ERT survey. Indeed, the resistivity measurements will also be strongly affected by topographical effects. Concentration of the current will arise in valleys, while current will disperse beneath hills. This will consequently create a distortion of the equipotential surfaces, leading to the generation of false anomalies or the masking of actual anomalies (Telford et al., 1990). In such cases, topography must be specifically taken into account in the inversion process. It seems also logical that the anisotropy of the media will produce a significant distortion. As it will be later developed in ***section 2.2***, data quality will also be affected by phenomena having different origins such as poor electrode contact, electrode polarization or indeterminate external parameters. To validate models, it is always interesting to combined intrusive techniques to the ERT method that only provides indirect information on the subsurface (Loke et al., 2013). In field investigation, the methods used can be, for example, drilling or cone penetration test (Vargemezis et al., 2015). Other limitations concern the inverse problem and will be approached in ***section 2.3***.

2.1.2 The Induced Polarization technique (IP)

A technique often used in addition to the ERT method is the “Induced Polarization” (IP). The type of electrodes array used during IP surveys is the same as for the ERT, given that the IP measurement is taken directly after the corresponding ERT measurement. It has been demonstrated that, when the current is abruptly switched off, the potential measured between the potential electrodes does not drop directly to zero. As a sudden decrease from the initial state occurs, the voltage will consecutively progressively dissipate. The same phenomenon occurs, but this time with an increase of voltage, when the current is turned on. This is principally due to the capacitive nature of the ground, which is capable to store and release electrical charges (Telford et al., 1990). Moreover, the capacitive nature of the ground also has an impact when a variable low frequency alternative current (AC) is used in place of a continuous current (DC) source. The capacitance allows the alternating current to pass, while blocking the direct current. This will induce a decrease of the apparent resistivity, while the frequency of the current source increases. The two phenomena presented above enabled the development of two different types of measurements for the IP technique (Kearey et al., 2002).

The first type of measurement is called the “time-domain IP surveying”, which measures the decay of voltage. The second one, is named “frequency-domain IP surveying” (Kearey et al., 2002). Given that only the time-domain IP was applied in the frame of this master thesis, the frequency-domain IP will not be further developed. To ensure that the measured signal is only related to the ground, the electrodes preferentially used for IP surveys should be non-polarizable, even if it is not always required (Reynolds, 2011).

Figure 7 displays the usual evolution of the voltage for time-domain surveying technique.

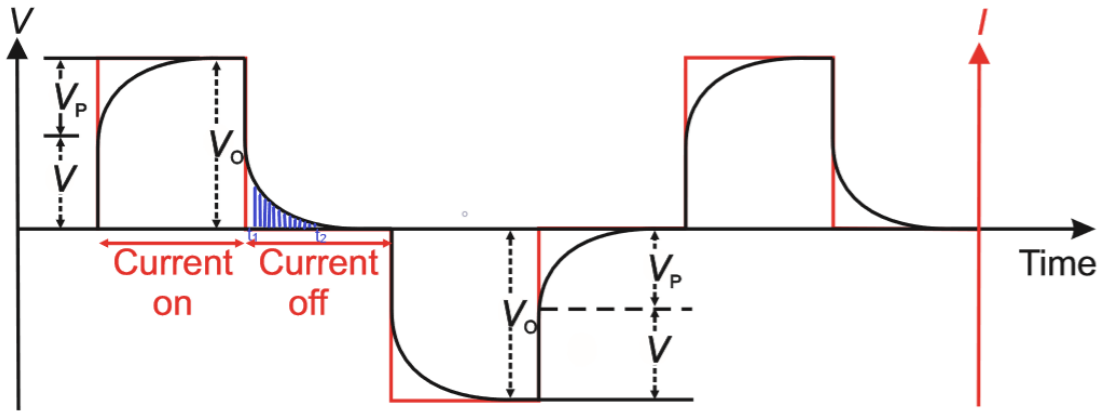

Figure 7. Evolution of the voltage depending on time (Modified from Reynolds et al., 2011)

The ability of the ground to release and store electrical charge refers to the chargeability property. Data collected during time-domain IP acquisition is called the apparent chargeability, symbolized by η_a, which is typically expressed in mV/V and can be defined by (Seigel, 1959):

$$\eta_a = \frac{V}{V_0} \qquad (7)$$

Where V is the voltage measured after switching off the current and V_0 the steady-state voltage. The time frame to measure V is a trade-off. On one hand, it is not advised to measure the potential directly after turning off the current because of large induced current. On the other hand, the potential needs to be measured before its complete decay (Telford et al., 1990).

To overcome this problem, the apparent chargeability can be defined following (Binley & Kemna, 2005):

$$\eta_a = \frac{1}{(t_2 - t_1)} \frac{1}{V_0} \int_{t_1}^{t_2} V(t)\, dt \qquad (8)$$

Where the apparent chargeability is now the integral of the voltage curve in a chosen time frame, from t_1 to t_2, divided by V_0 (***Figure 7***). It is now easy to understand that the chargeability is affected by the nature of the ground but also by the initial input current. Therefore, for an appropriate comparison between different IP survey, the chargeability is often normalized to a standard current (Reynolds, 2011).

The induced polarization is driven by two main mechanisms, linked to electrochemical processes. The first one is the so-called “membrane polarization”, which is due to an electrolytic flow in the pore fluid, imposing a certain voltage into the rock. Due to the fact that most minerals composing a rock have an external surface negatively charged, positive ions are attracted and accumulate in the pore space. The accumulation at the pore constrictions, of positive charges provokes the inhibition of the negative ions movement (***Figure 8***). When the current is stopped, the system tends to go back to its steady state, causing a gradual decay of the voltage (Kearet et al., 2002). Given that the membrane polarization is affected by the size of pores, it is not surprizing to discover that this effect is especially accentuated in presence of clay and depends on the type of minerals present. Another factor increasing the polarization membrane effect is the salinity of the fluid flowing through the pores of the rock (Telford et al., 1990).

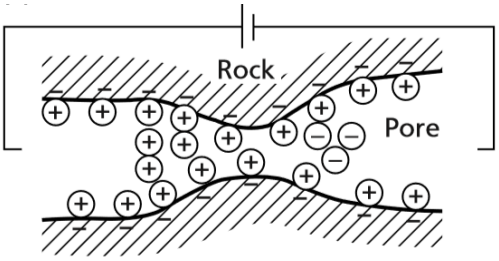

Figure 8. Membrane polarization mechanism (From Kearey et al., 2002)

The second mechanism is called the “electrode polarization”. This effect applies in presence of metallic minerals in the rock, in which the external voltage is imposed

and where part of the current flow is electronic, through the mineral grain, while the other current part is electrolytic (Telford et al., 1990).

As displayed in ***figure 9***, the applied voltage induces an accumulation of positive and negative charges on each side of the mineral grain. An exchange occurs at the interface with the grain, where the negative ions will attempt to release electrons through the grain, while the positive ions will catch these same electrons. Nevertheless, the rate of electrons exchanged at the interface is higher than the electrons flow in the pore, generating a piling up of ions at the interface. This phenomenon keeps on going until the imposed current is switched off. Once again, the interruption of the current causes the diffusion of the ions back to their natural locations, producing a slow dissipation of voltage (Kearey et al., 2002). The mineral required for this mechanism is an electronic conductor.

Moreover, considering that this is a surface mechanism, the phenomenon will be accentuated if the mineral is disseminated and not massive. The polarization is also influenced by the type of fluid flowing through the rock, with IP measurement showing high results in medium where 75% of the pores are filled with water (Telford et al., 1990).

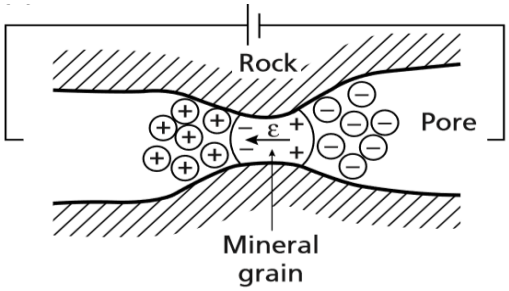

Figure 9. Electrode polarization mechanism (From Kearey et al., 2002)

2.2 Data quality assessment

As briefly described in ***section 2.1.1***, a multitude of errors can affect the measured data and the subsequent models. In this way, it is important to fully investigate the different types of errors affecting data to understand how they could impact the final results (Zhou & Dahlin, 2003).

One of the main errors occurring in data measurements is defined as the “injection electrode overprinting” by Merriam (2005) or also as the “electrode polarization” by Wilkinson et al., (2012). This polarization is due to a charge build-up at the interface between the conducting metal, of which the electrodes are made, and the surrounding ground with a smaller conductance. This effect mainly occurs when the same electrode is being used to measure potentials after being used as current injector. This may have for effect to generate much larger unwanted potentials than the real induced potentials (Dahlin, 2000). It has already been demonstrated that modern equipment easily deals with this issue and that it only remains problematic in case the decay of the polarization potential is much higher than the amplitude of the received pulse (Merriam, 2005). However, in order to maintain data quality, a few precautions should be taken. The first one is to avoid the acquisition of any measure of potential on an electrode that was previously used to inject current, without a

sufficient time lapse. This consideration needs to be directly taken into account for the survey design (Dahlin, 2000). Another possibility is to use non-polarizing electrodes although they remain more expensive and are more challenging to use than traditional metallic (usually steel) electrodes (Wilkinson et al., 2012).

Another error that should be pinpointed is called the electrode spacing error and is caused by the inaccuracy generated when the electrodes are being set up for the investigation campaign. Understandably, this inaccuracy will affect the quality of the image computed from the measurements (Zhou & Dahlin, 2003).

As already highlighted in ***section 2.1.1***, another deterioration of data quality can take place directly during the measurement due to a poor electrode contact. Such error can be minimized by wetting the electrodes before the acquisition or by using non-conventional electrodes (Athanasiou et al., 2007).

An adequate noise estimation is essential for reliable results. Indeed, an overestimation of the noise will lead to a decrease of image resolution, while an underestimation will generate the apparition of artificial structures. More generally, a poor quantification of noise estimation can lead to misinterpretation of the resulting model as demonstrated by LaBrecque et al., (1996).

Concerning the noise estimation, two main approaches are generally used. The first one makes use of the repetition of measurements. However, it has been shown that this approach greatly underestimates the true noise levels (LaBrecque et al., 1996). Another approach, leading to a more accurate estimation consists in comparing the acquired data with reciprocal measurements. These reciprocal measurements are computed by switching the injection and potential electrodes. According to the principle of reciprocity (Parasnis, 1988), exchanging the electrodes should not lead to a change in the measured resistance. However, in practice, a difference between the two acquisition modes is observed. This leads to the computation of the reciprocal error, *e,* which is defined as (**equation 9**):

$$e = R_n - R_r \qquad (9)$$

Where, R_n is the normal resistance measurement and R_r is the reciprocal measurement. Slater et al., (2000) pointed that the reciprocal error could be used to detect inaccuracies which remained undetected by repeating measurements. Nevertheless, the reciprocal error approach has for major drawback to only gives an individual variance, without tacking the possible correlation between errors (Koestel et al., 2008).

LaBrecque et al., (1996) also pointed the fact that both repetition and reciprocal approaches measure the precision and not the accuracy. Therefore, there remains many sources of systematic error that will not be taken into account. They also highlighted the fact that the noise estimation will not account for some field procedural or modelling errors.

One way to incorporate noise estimation in the inversion process is to build the so-called “error model”. Nowadays, two different methods are widely used. The first one was proposed by Slater et al., (2000) and considers a Gaussian error model. It is

because when |*R*|, namely the mean of the measured resistances, increases, the magnitude of the reciprocal error |*e*| increases proportionally following:

$$|e| = a + b|R| \qquad (10)$$

Where, the parameter *a* represents the minimum error and *b* the increase in |*e*| with |*R*|, which can also be defined as the relative error. After removing the obvious outliers, the parameters are defined by choosing an envelope encompassing all remaining measurements (**Figure 10**).

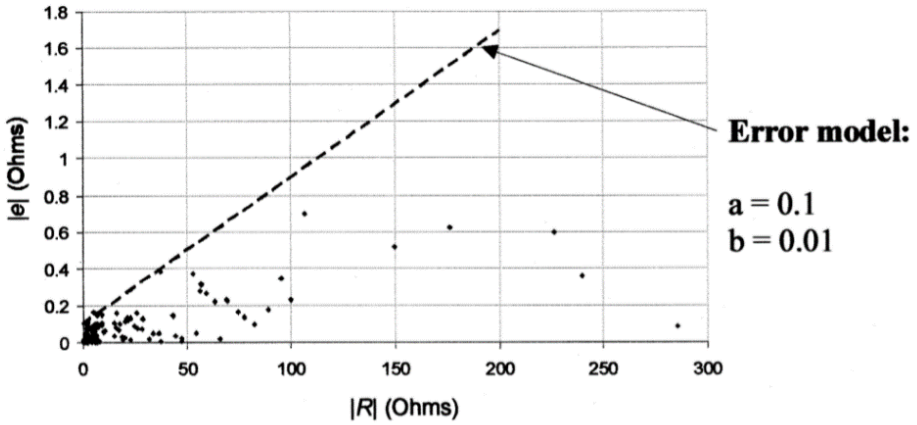

Figure 10. Error model (Slater et al., 2000)

Another approach was developed by Koestel et al., (2008). It is based on **equation 10**, but differs in the way of computing the parameters. For this approach, the range of measured resistance is subdivided into logarithmically, equally sized bins. Furthermore, the standard deviation of the reciprocal error, s_{bin} is computed for each bin. Finally, as shown ***figure 11***, the parameters are determined by a curve fitting s_{bin}.

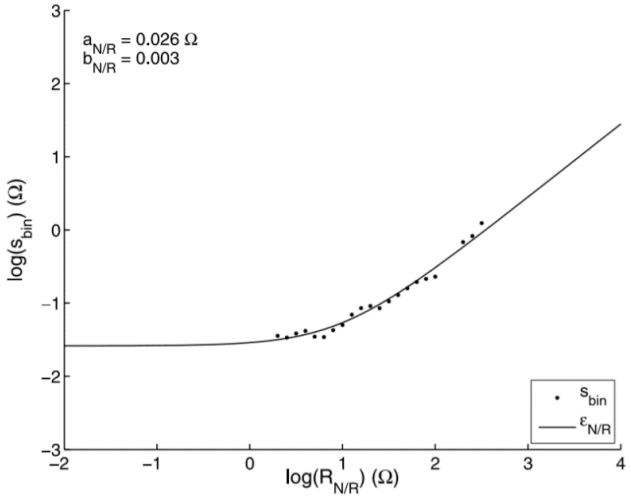

Figure 11. Error model (Koestel et al., 2008)

It is important to notice that even with an acceptable data quality and with a satisfactory noise estimation, the resulting image does not exactly fit the geological representation but always has undergone some distortions. Therefore, it is recommended to understand the basic principal of the inversion method for a proper interpretation of the obtained image (LaBrecque et al., 1996).

2.3 The inversion procedure

In order to compute the distribution of intrinsic electrical properties, i.e. the resistivity, conductivity and chargeability, it is necessary to carry out the mathematical procedure called inversion. The aim of the inversion procedure is to produce a model that optimally fits the acquired data, while satisfying other enforced constraints. If ***m*** represents the physical parameters of the medium and ***d*** the acquired data, the mathematical representation of the problem can be formulated as:

$$\mathbf{d} = G(\mathbf{m}) \qquad (11)$$

Where G is defined as forward operator or forward function. Finding **d** given **m** is called the forward problem, while finding **m** given **d** is the inversion problem (***Figure 12***) (Aster et al., 2013)

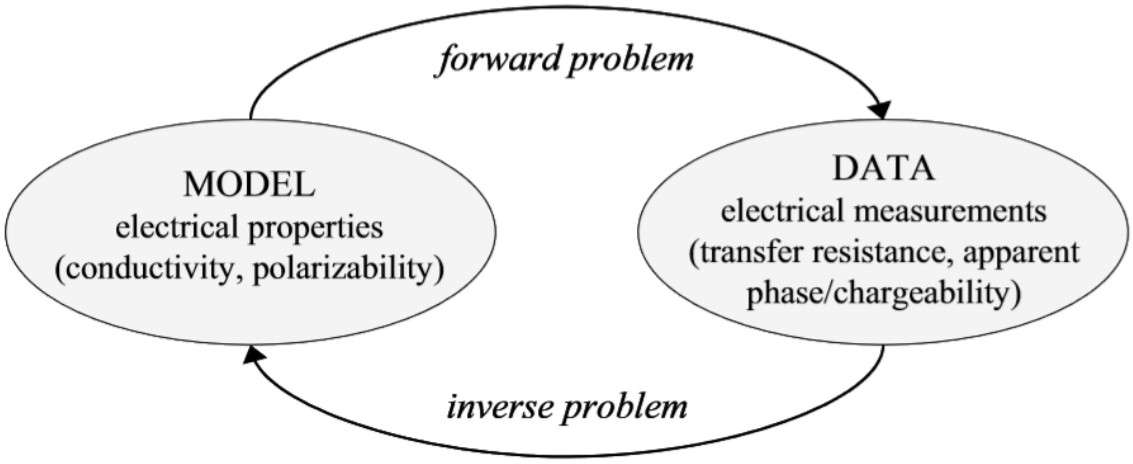

Figure 12. Representation of the forward and inverse problem (From Binley & Kemna., 2005)

2.3.1 Forward model

Following Daily et al., (2005), for a point source current I and a 3D distribution of isotropic conductivity σ, the forward model can be mathematically represented by:

$$\frac{\partial}{\partial x}\left(\sigma\frac{\partial V}{\partial x}\right)+\frac{\partial}{\partial y}\left(\sigma\frac{\partial V}{\partial y}\right)+\frac{\partial}{\partial z}\left(\sigma\frac{\partial V}{\partial z}\right)=-I\,\delta(x)\delta(y)\delta(z) \qquad (12)$$

and subject to boundary conditions:

$$\sigma\frac{\partial V}{\partial n}+\beta V=0 \qquad (13)$$

Where δ is the Dirac delta function, n the outward normal, V the potential and β a variable defining the boundary type. If β is equal to 0, it indicates that we are dealing with Neumann boundary conditions, which is the case at the surface. For the remaining boundaries, the conditions are mixed and β remains finite and nonzero. When dealing with a half-space region, it has been demonstrated, that having mixed boundary conditions enables the omission of modelling current flow at significant distances from the zone (Daily et al., 2005).

The inversion of induced polarization data can be achieved by two different strategies. For the one applied in the time domain approach, in a chargeable medium defined with a conductivity σ_{DC} and an intrinsic chargeability η, it has been demonstrated the measured voltage can be seen as the decreasing conductivity of a non-polarizable medium, σ_{IP} (Seigel, 1959):

$$\sigma_{IP} = (1 - \eta)\sigma_{DC} \quad (14)$$

And following Oldenburg & Li (1994), the computation of the apparent chargeability, η_a, can be achieved by performing two resistivity forward models with σ_{IP} and σ_{DC}. Therefore, the apparent chargeability can be formulated as:

$$\eta_a = \frac{G\,(\sigma_{IP}) - G(\sigma_{DC})}{G\,(\sigma_{IP})} \quad (15)$$

2.3.2 Inverse problem

In the frame of this thesis, different software will be used to perform the different inversions. For the 3D ERT inversion, the software called E4D will be used. Nevertheless, due to logistical limitation another software will have to be used to perform the 3D IP inversion. This software is named BERT, for Boundless Electrical Resistivity Tomography. Finally, for the 2D ERT and IP inversion RES2DINV will be used.

It has been acknowledged that geophysical forward problems are nonlinear. The corresponding inverse problems are also nonlinear, which significantly complicates the computation.

When it comes to inversion, three main issues should be addressed: the existence, the uniqueness and the instability. Concerning the existence, it has been proved that for linear problem, the question could always be answered through regularization. However, for non-linear problems, the theory remains quite elusive (Parker, 1994). The inexistence of a model fitting the data can occur in case of noisy data set or in case of an approximated mathematical representation of the physics of the system (Aster et al., 2013a). Even though the existence of the solution is granted, the question of its uniqueness remains. If only a finite number of elements constraining the distribution of some physical parameter is used, it will lead to the non-uniqueness of the solution. This means that different models will lead to the same response. Therefore, the construction process of the solution needs to be taken into account. The restriction of the model computation by predefined characteristics during the inversion, can lead to the generation of a relevant unique solution. This is made possible by formulating the inverse problem as a regularized optimization problem, involving the minimization of an objective function. This function takes into account two components, which are a data misfit and a penalty term highlighting the deviations from the predefined model, which is the so-called regularization (Binley & Kemna, 2005). The regularization is also practical to deal with instability. Indeed, a small change in measurement often leads to a completely different estimated model during inversion processing. In those cases, the inverse problem is defined as ill-posed for a continuous system or ill-conditioned for a discretized linear system. The role of the regularization

is therefore to stabilize the inversion process and to produce an acceptable solution (Aster et al., 2013a).

To compute the inverse problem, the region of interest is discretized and a parameter m is assigned to each elements. Due to the large interval in which the conductivity evolves, the conductivity is most often expressed under its logarithmic form in inverse problem:

$$m_j = \ln \sigma_j \quad (16)$$

with j = 1,2,…, M and with M being the number of elements used to discretize the region. All the calculated m_j are resumed in a vector **m**.

For the measured data, **d**, the same log-transformation is applied on the measured resistance, R, once again due to the wide range of resistance that can occur:

$$d_i = -\ln(R_i) \quad (17)$$

with i= 1,2,…, N and with N being the number of measurements. All the acquired data are resumed in a vector **d**.

It is important to emphasize that the use of a log-transformation goes with several repercussions. Indeed, it requires that the polarity of the measured and modeled resistance is identical., which is not always the case. If measurements do not satisfy this criterion, they will be, either definitively or temporarily, neglected during the inversion (Daily et al., 2005).

As already mentioned, the inverse problem involves the minimization of an objective function accounting for a data misfit. The data misfit term in the objective function can be calculated using the L_2 norm corresponding to the least squares solution and is expressed as:

$$\Psi_d(\boldsymbol{m}) = \|\boldsymbol{W}_d[\boldsymbol{d} - \boldsymbol{G}(\boldsymbol{m})]\|^2 \quad (18)$$

Where, $\boldsymbol{W}_d$ is the data weighting matrix. If uncorrelated data are assumed, it is possible to express it in terms of data errors, ε_i, with i = 1,2,…,N. This leads to:

$$\boldsymbol{W}_d = diag\left(\frac{1}{\varepsilon_1}, \ldots, \frac{1}{\varepsilon_N}\right) \quad (19)$$

Another function that can be used is the L_1 norm, which is formulated as:

$$\Psi_d(\boldsymbol{m}) = \|\boldsymbol{W}_d[\boldsymbol{d} - \boldsymbol{G}(\boldsymbol{m})]\| \quad (20)$$

The use of L_2 norm should be preferred when data noise follows a Gaussian distribution. However, in case of noisy data with outliers, this norm, induces a disproportionately large contribution of high-valued residuals as it squares the difference between observed and simulated data. The main negative effect is that outliers will deviate the predicted data from the remaining data set. The effect on the final model is that any significant change between two neighboring cells is ruled out. Contrariwise, the L_1 norm does not square the elements, inducing a proportional contribution, which reduces the effect of outliers. The L_1 norm is consequently defined

as more robust and will not discriminate any significant change between two neighboring cells in the resulting model (Farquharson, 2008).

As discussed, if the objective function was only composed of ***equations 18*** or ***20***, the resulting solution might be unstable since the inverse problem is ill-posed. The regularization requires the introduction of a stabilizing term in the objective function. The added term will represent a measure of the model misfit. Therefore, it will indicate how neighboring parameter values vary, which is defined as the roughness, but also how the values will differ from a specified model. It can be formulated as:

$$\Psi_m(\boldsymbol{m}) = \alpha \|\boldsymbol{W}_m[\boldsymbol{m} - \boldsymbol{m_0}]\|^2 \qquad (21)$$

Where α is the regularization, or trade-off, parameter. Its role is to assign the relative contributions of the data misfit term and of the model complexity term (Farquharson,2008). $\boldsymbol{W}_m$ is called the roughness matrix and defines the spatial extent and nature of the constraint applied on the model parameters. It is possible to construct $\boldsymbol{W}_m$, to avoid smoothing between neighboring cells, by defining $\boldsymbol{W}_m$ as a unit diagonal matrix, or also to permit anisotropic smoothing. $\boldsymbol{m}_0$ is the reference model parameter, which is not especially uniform and can be removed by defining $\boldsymbol{m}_0$ as the null vector (Daily et al., 2005). The choice of the model constraint to apply will depend on the objectives of the study and on the geological knowledge.

The final objective function can be now written as:

$$\Psi(\boldsymbol{m}) = \Psi_d(\boldsymbol{m}) + \Psi_m(\boldsymbol{m}) \qquad (22)$$

To deal with non-linear problems the standard strategy is to use an iterative procedure that linearly approximate the inverse problem at each iteration. Subsequently, all the terms of the objective function need to be linearized. Moreover, the use of other norms than L_2 also introduces a non-linearity that needs to be treated (Farquharson,2008). In such case the procedure used is called the iteratively reweighted least squares (IRLS) and is the one used by the software E4D that will be used for the inversion in the frame of this master thesis (Johnson et al., 2010).

The final linear system of equations that needs to be solved at each iteration can be expressed as:

$$[\boldsymbol{J}^T\boldsymbol{W}_d{}^T\boldsymbol{R}_d\boldsymbol{W}_d\boldsymbol{J} + \alpha\boldsymbol{W}_m{}^T\boldsymbol{R}_m\boldsymbol{W}_m]\Delta\boldsymbol{m} = \boldsymbol{J}^T\boldsymbol{W}_d{}^T\boldsymbol{R}_d\boldsymbol{W}_d(\boldsymbol{d} - \boldsymbol{G}(\boldsymbol{m})) + \alpha\,\boldsymbol{W}_m{}^T\boldsymbol{R}_m\boldsymbol{W}_m(\boldsymbol{m}_0 - \boldsymbol{m}) \quad (23)$$

With **J** being the Jacobian, or sensitivity, matrix for the current model, which is expressed (Farquharson,2008):

$$J_{ij} = \frac{\partial G(m)_i}{\partial m_j} \qquad (24)$$

$\mathbf{R}_d$ and $\mathbf{R}_m$ are diagonal weighting matrix, which contain the absolute values of the reciprocal of the residual (Aster et al., 2013b).

$\Delta\boldsymbol{m}$ is the update vector and is, in fact, a solution to ***equation 23*** that tends to minimize the objective function. Moreover, **J**, $\mathbf{R}_d$ and $\mathbf{R}_m$ depend on **m** and will therefore be recomputed at each iteration, which requires a large amount of available memory and

an extensive computational effort. The number of iterations depends on a criterion fixed by the data noise. It is also important to note that during the process, α varies in order to keep the trade-off between the data fit and the model constraints. To estimate the most appropriate α, E4D provides two possibilities. Although a line search is provided, the default method relies on a reduction factor provided by the user, impacting the regularization parameter between two iterations (Johnson, 2014).

As aforementioned, besides the 3D inversion performed with E4D, 2D inversions will be carried out using the RES2DINV software (Loke, 2018). The inversion iterative algorithm used to deal with the non-linear inverse problem is, this time, the Gauss-Newton algorithm with the Marquardt-Levenberg modification, to avoid any singularity problem, when the matrix $\mathbf{J}^T\mathbf{J}$ is computed (Loke, 2018).

For the inversion of IP data, Oldenburg & Li (1994) developed three different methods. Two of them can be used when the chargeability is small. The first approach consists in the linearization of ***equation 15***, using the conductivity obtained after inverting DC potentials. Subsequently, the chargeability is recovered by solving a linear inverse problem. The second method consists in producing a chargeability model, by the manipulation of conductivities, that were the results of the previous inversion of two dataset coming from an ERT/IP survey. The third strategy, more general and precise, as it is not limited by a defined chargeability, solves the problem as a non-linear IP problem similarly to ERT

Concerning the inversion of IP data in 2D, RES2DINV offers two possibilities. The first possibility is to carry out a first inversion of the resistivity independently of the IP data. Then, using the model resistivity, the IP data are computed following ***equation 15***. Finally, an IP inversion is performed (Loke,2018). This corresponds in fact to the first approach proposed by Oldenburg & Li (1994). The second possibility offered is to use a complex resistivity, where a joint inversion using both apparent resistivity and IP data is performed (Loke, 2018).

Unfortunately, E4D required a license that is not free of charge to invert IP data, which was not available at the time of the master thesis. The 3D IP inversion was therefore performed with BERT, which is more oriented to frequency-domain data, but still can be used to treat other type of data (Günther & Rucker, 2018). The algorithm starts with the inversion of the magnitude resistivity. Then, using Cauchy-Schwarz equation, it is possible to linearize the inversion of the imaginary part of the resistivity. The last step consists in transforming back the imaginary resistivity into a phase shift. The regularization parameter is chosen in order to fit the data within the level of noise (Martin & Günther, 2013).

2.3.3 Model appraisal

A proper interpretation of the results requires to estimate the inverse model reliability.

A well-known way to assess the reliability of the model for linear inverse problem is to calculate the resolution matrix, ***R***. It is a highly complex function accounting for a wide number of parameters such as the type of regularization, the electrode array, the block size, the noise estimation and resistivity. It can be used to determine the effect of the regularization and the effect of the constraints imposed by data for each model

parameter (Daily et al., 2005). The resolution matrix can be estimated for non-linear problem as:

$$\boldsymbol{R} = (\boldsymbol{J}^T \boldsymbol{W}_d{}^T \boldsymbol{W}_d \boldsymbol{J} + \alpha \boldsymbol{W}_m{}^T \boldsymbol{W}_m)^{-1} \boldsymbol{J}^T \boldsymbol{W}_d{}^T \boldsymbol{W}_d \boldsymbol{J} \quad (25)$$

A more obvious definition of **R** is:

$$\boldsymbol{m} = \boldsymbol{R}\, \boldsymbol{m}_{true} \quad (26)$$

Where **m** represents the vector resuming the parameters of the model obtained after the inversion and $\mathbf{m}_{true}$, the same vector but this time with the actual parameters (Binley & Kemna, 2005). In case of a perfect resolution of the complete model, the resolution matrix is defined by the identity matrix. This is obviously ideal, although unrealistic. If the matrix differs from identity, it indicates that the parameters resulting from the inversion have undergone an averaging process. Even if there are not usual, the terms which are not placed on the diagonal of ***R*** may indicate consequences of a blurring on each pixel value. Although the resolution matrix has been demonstrated to be an appropriate representation of reliability, its computation is numerically expensive. Unfortunately, the computation of the resolution matrix was not provided by the software used during this master thesis.

Due to the presented limitation of **R**, one may use the sensitivity matrix to appraise model reliability. Following Kemna (2000), the sensitivity matrix can be defined as:

$$\boldsymbol{s} = \boldsymbol{J}^T \boldsymbol{W}_d{}^T \boldsymbol{W}_d J \quad (27)$$

The values of the elements within the vector ***s*** are elevated where the sensitivity of the measurement is good and low otherwise. Furthermore, the sensitivity matrix being directly computed during the inversion, it is consequently time inexpensive. Such tool was used in Nguyen et al. (2009) or Caterina et al. (2013) with success.

An alternative strategy to assess the model reliability is to resort to the depth of investigation (DOI) index (Oldenburg & Li, 1999). This approach consists in performing an inversion process with two reference models named $\mathbf{m}_{01}$ and $\mathbf{m}_{02}$. After computing the final models, $\mathbf{m}_1$ and $\mathbf{m}_2$, the DOI for a certain block i, can be calculated from the following equation:

$$DOI_i = \frac{|m_{1,i} - m_{2,i}|}{|m_{01,i} - m_{02,i}|} \quad (28)$$

Zones of the model where DOI is low indicate that data still constrain the model.

Oldenborger et al., (2007) has also demonstrated the use of DOI for assessing the reliability of 3D models. They proved that, even if there was a discrepancy between the DOI and the resolution matrix, they were clearly related. They also indicated that due to the fact the DOI is having more distinct regions, it was hard to compare the two tools. Furthermore, their results showed that the sensitivity was not providing any information of the potential for near-electrode artefacts.

2.4 The Horizontal to Vertical Noise Spectral Ratio technique (HVNSR)

The horizontal to vertical noise spectral ratio is a passive method taking advantage of the ambient seismic vibrations, that is now of great interest for near-surface geophysicists since its use by Nakamura (1989). It proved to be an attractive method for estimating the dynamic characteristics, mainly the resonance frequency, of surface layers when two horizontal and one vertical components of the noise propagation are known, by the use of microtremors. The measurement consists in recording the ambient vibration noise during an adapted time-lapse. The time required will depend on the targeted frequency and the required data quality. The technique to process the recorded data is to estimate the proportion of the Fourier amplitude spectra of the horizontal component of the ambient noise against those of the vertical components acquired at a certain point (Oubaiche et al., 2012). ***Figure 13*** displays a typical graph obtained after applying the Fourier transformation.

Once processed, one needs to assess where the HVNSR peak frequency is reached and how it is distributed.

As the validity of this method relies on the mechanical contrast between two layers, it has to be assumed that the waste layer in a landfill presents a mechanical difference with the underlying bedrock. This contrast is often pinpointed by the computation of shear wave (S-wave) velocity, being much lower for waste layers than for the underlying substratum (Dumont et al., 2017). Nevertheless, the heterogeneity often encountered in landfills, complicates the interpretation of such measurement (Soupios et al., 2007).

The frequency of the peak will depend on the resonance frequency of the upper layer, while its distribution will reflect the spatial variation. In fact, the peak frequency will give an indication on the thickness of the surficial layer, while the amplitude will indicate the importance of the contrast in the S-wave velocity between the top layer and the probable bedrock (Oubaiche et al., 2012). It has been shown that appropriate results were obtained when the S-wave contrast was elevated (Haghshenas et al., 2008). Furthermore, Guéguen et al., (1998) showed that in some cases, a second peak could arise. This can happen in places where three layers, with a significant S-wave velocity contrast, occur with, for example, a soft sediment layer above a more consolidated sediment layer, overlying itself the bedrock. However, Oubaiche et al., (2012) showed that this peak could be explain by another phenomenon described as *“the contribution of the odd harmonic of the vertical incident S-wave transfer function of a third, deeper layer with the fundamental mode linked to the first two upper most layers*”.

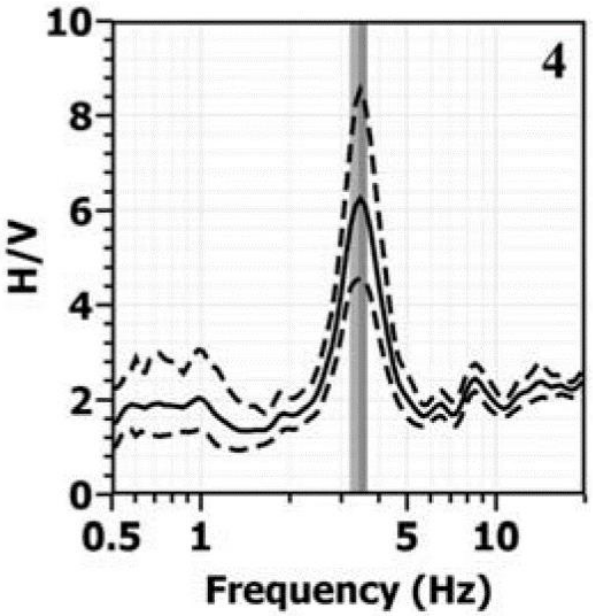

Figure 13. Typical HVNSR graph (From Oubaiche et al., 2002)

If the thickness of the overlying layer is known, it is possible to find the S-wave velocity of the layer following:

$$f_0 = \frac{V_s}{4\,H} \qquad (29)$$

Where, f_0, V_s and H are the resonance frequency, the average S-wave velocity and the thickness of the surficial layer respectively. In fact, if the S-wave velocity had been previously measured with another method, such as the multichannel analysis of surface wave dispersive behavior (MASW), it is possible to go the other way around and to compute the approximate thickness (Dumont et al., 2017). In practice, the relation described in ***equation 29*** is verified under certain assumptions i.e. one-dimensional velocity subsurface conditions and a homogenous and isotropic layer of sediments over a homogenous half-space. Such conditions are rarely met in practice. If the ground contains internal structures, anisotropy or low velocity layers, the previous assumptions are transgressed, as the HVNSR spectrum is impacted. One way to deal with such complex geology is to perform an inversion of the spectrum (Yan et al., 2018).

Bonnefoy-Claudet et al., (2006) performed a study on the effect of the distribution of noise sources for idealized conditions. They firstly showed that the peak frequency is time-independent, while the amplitude of the peak was only impacted by the time constraint. However, they showed how crucial the spatial location of the noise sources on the HVNRS spectra was. They highlighted three main source's locations. For sources located in the bedrock, the S-wave resonance of the head waves is mainly responsible for the peaks in the spectra. For distant sources, located into the sedimentary layer, two peaks appear, respectively due, for the first, to the fundamental mode of Rayleigh waves and the resonance of head S-wave and, for the second, to head waves. For source located in the same layer but closer, only one frequency peaks, due to the "*horizontal ellipticity of fundamental mode of Rayleigh waves*" (Bonnefoy-Claudet et al., 2006).

The processing of data can be divided in several steps. First, it is necessary to select stable windows in the obtained graph and to perform a spectral analysis (Brûlé & Javelaud, 2013). ***Table 2*** summarizes all the recommendations in terms of minimum length of the stability window, minimum number of windows and the recommended recording time for the targeted resonance frequency (SESAME, 2004).

Table 2. Recording recommendations (Modified from SESAME, 2004)

Resonance frequency of interest [Hz]	Minimum window length [s]	Minimum number of windows	Minimum recommended recording time [min]
0.2	50	10	30
0.5	20		20
1	10		10
2	5		5
5	5		3
10	5		2

For a practical perspective, the ambient noise is recorded by an acoustic velocimeter, enabling the measurement of the noise propagation in three directions. Different types of courses exist with different bandwidths. It is therefore of interest to have an elusive notion of the actual geology in order to select the appropriate device (Brûlé & Javelaud, 2013). The Site Effects Assessment Using Ambient Excitations (SESAME) European research project (2004) provided a detailed study of this type of measurements. In addition to some theoretical aspects, the SESAME project especially deals with the experimental conditions and advices on how to interpret the different obtained results. For the experimental conditions, they give recommendations on the type of soil on which the sensor should lay, but also recommends to place the sensor away from any structures (e.g. buildings, trees, etc.) and provides information on weather conditions for an optimal data acquisition. Moreover, they provide an adapted methodology to assess the reliability of peaks in the H/V spectrum.

3 REVIEW OF THE SELECTED METHODS FOR THE CHARACTERIZATION OF LANDFILLS

This section introduces the different possible applications of the geophysical methods chosen in this thesis for the characterization of landfills. Soupios & Ntarlagiannis (2017) summarized the different outcomes obtained by applying various geophysical methods on landfills. First, it is possible to define the extent and the geometry of landfills. Besides, the monitoring and characterization of numerous parameters such as moisture, gas content and leachate distribution, is rendered possible by geophysical methods. The composition of certain material can be recognized as well with geophysics. Moreover, it can help with the monitoring of the quality of the liner and eventual leaks in new landfills. The present section will mainly focus on the applications of the three methods that have been presented, namely the ERT, IP and HVNSR techniques.

Table 3 summarizes the main applications of the three different electrical methods used in the frame of this mater thesis.

Table 3. Summary of the methods used in the frame of this mater thesis and their main purposes in landfills characterization

GEOPHYSICAL METHOD	APPLICATION
Electrical Resistivity Tomography (ERT)	▪ Presence of waste ▪ Spatial delimitation (*vertical and horizontal*) ▪ Water content ▪ Contamination
Induced Polarization (IP)	▪ Spatial delimitation (*vertical and horizontal*) ▪ Biodegradation
Horizontal to Vertical Noise Spectral Ratio (HVNSR)	▪ Lateral extension ▪ Depth

3.1 Electrical Resistivity Tomography technique (ERT)

The Electrical Resistivity Tomography (ERT) technique remains most certainly the principal method used in environmental geophysics, mainly due to its robustness and the wide range of resistivity values observed in near-surface environments. The resistivity, which is the parameter obtained from ERT surveys, highly depends on various factors, i.e. the mineralogy, the lithology, the presence of fractures, the porosity, the hydrogeological environment, the salinity, the compaction, the presence of clay, a possible contamination, etc. (Balia, 2018). It is therefore plausible that a variation of resistivity could arise for many different sources.

Yannah et al., (2017) summarized various information that can be provided by the resistivity contrasts encountered during ERT survey in landfills. It allows to estimate the heterogeneity level as well as to detect of the bottom of the landfill. Nevertheless, ERT is not the best method to discriminate different types of materials as their resistivity may overlap due to various parameters, such as the fluid saturation, porosity and so on. Moreover, Dumont et al., (2017) expressed some concerns about the ability of ERT to estimate the thickness of a landfill, unless it is not too thick, the electrical conductivity of the waste material not too high and if there is a sufficient contrast

between the resistivity of the waste and the bedrock. Usually, the waste will be characterized by a much lower resistivity than the surrounding bedrock notably due to the presence of highly conductive leachate (Harjito et al., 2018). Nevertheless, higher resistive zones can occur within the waste. This could be explained by either more aerated material or a massive presence of inert (Di Maio et al., 2018).

Another aspect that can be highlighted by the ERT technique is the water content. As discussed, the resistivity is affected by the presence of water. It is therefore possible to differentiate saturated zones from unsaturated ones within the waste by observing changes in the resistivity (Dumont et al., 2016)

ERT final images can also display highly conductive zones far below the assumed depth of the waste within the bedrock which can be considered as leachate leaking out of the landfill (Chambers et al., 2006; Di Maio et al., 2018). Indeed, ERT can also be used to investigate polluted area in groundwater. Polluted zones will be characterized by very low resistivity values due to the increasing number of ions in groundwater, consecutive to an inlet of leachate generated by the waste (Harjito et al., 2018). Considering the infiltration and diffusion processes, it is possible to observe an increase of the conductivity in the deepest parts of the waste (Di Maio et al., 2018).

The greatest limitation of ERT is that although it identifies the presence of waste and contamination, it cannot differentiate them from each other (Elis et al., 2016). As explained in ***section 2.1.2***, this distinction can be achieved by coupling an IP survey to ERT. The ERT technique can also determine the spatial extension of the waste although certain conditions are required to get an appropriate representation of the bottom interface.

3.2 Induced Polarization technique (IP)

The Induced Polarization (IP) technique is also a promising method to characterize landfill and has been widely used in the past. Up to that time, anomalous chargeability values were associated mostly with metallic scraps in the waste. Even if metal impacts IP values, it has been recently demonstrated, that the anomalies could arise from many different sources such as organic matter, wood (Thierry et al., 2001) or vegetative matter (e.g. peat) (Slater & Reeve, 2002). Due to the elevated isolating surface, plastic can also lead to high chargeability value (Leroux et al., 2007). Carlson et al., (2015) demonstrated that a biodegradation process affecting the waste, could generate a higher IP response. They showed that asbestos had a weak effect on the IP response, although still perceivable. In this way, the overall chargeability of waste can reach hundreds of mV/V (Dahlin et al., 2010).

One of the limitations of the IP technique lies in the spatial delimitation of the waste, especially in the bottom of the landfill. It remains sometimes challenging to precisely define the limits of the waste. A way to by-pass the problem is to compute the normalized chargeability, which is the ratio of the chargeability by the electrical resistivity. This will produce an image with a better delimitation of the waste (Dahlin et al., 2010). Moreover, the normalized chargeability allows performing a distinction between the waste and contamination plume (Elis et al., 2016).

The combination of IP and ERT can provide a lot of valuable information. It remains complicated to define the spatial extension of waste with the single ERT method as explained above. If a doubt subsists with the ERT results, the high chargeability values measured by IP can confirm the waste delimitation (Leroux et al., 2007; Dahlin et al., 2010). If the combined survey displays high resistivity and an intermediate IP response, the materials lying underground possibly are a coarse geological material or waste mainly composed of debris from the construction sector (Leroux et al., 2007).

Used in this way, IP surveys remain, to some extent, a useful tool to characterize the waste composition (even though it is challenging), to define its spatial distribution and to highlight a probable biodegradation.

3.3 The Horizontal to Vertical Noise Spectral Ratio technique (HVNSR)

The use of the Horizontal to vertical noise spectral ratios technique (HVNSR) in landfills is rather new. Indeed, it is mainly used to assess the ground response during an earthquake event and this, for topmost soft layers in particular (Nguyen et al., 2004; Singh et al., 2017; Subiyo et al., 2018). However, some authors pinpointed the interest of the technique to estimate the thickness of the ice sheet in the Antarctic (Yan et al., 2018), demonstrating its use in different environments. Looking at ***equation 29***, it is possible to provide a S-wave velocity model of the waste deposit (Soupios et al., 2005; Soupios et al., 2007). When the average S-wave velocity has been estimated, either by HVNSR or by MASW, it is possible to go the other way around to calculate the waste depth (Soupios et al., 2007; Dumont et al., 2017).

HVNSR is therefore appropriate to get an approximate insight of the ground internal structure and especially of the depth of waste deposit. Nevertheless, the value of HVNSR measurements in landfill surveys, relies on the mechanical contrast between the waste layer and the underlying bedrock. This contrast needs to be sufficient enough to show interpretable results in the H/V graph. Furthermore, the thickness computed using ***equation 29*** is often impacted by an error due to the complexity of the structure encountered in landfills (Soupios et al., 2007). Moreover, due to the spatial heterogeneity of the subsurface in landfills, the validity of the interpretation of the H/V graph obtained from a measurement in the field, remains only very localised. Consequently, the proper modelling of landfills by the HVNSR, requires a high number of measurement points.

4 THE CASE STUDY OF ONOZ TO ASSESS ERT/IP AND HVNSR FOR LANDFILL CHARACTERIZATION

4.1 Historical context of the site

The landfill investigated in the frame of this master thesis is located in the village of Onoz, in the province of Namur. The total surface of the site is about 17 hectares. Initially, the site was exploited as a quarry, from which the high-quality limestone of the "*Viséen*" was extracted. Simultaneously, a battery of lime kilns was performing on the site. The site operated as such from 1902 to 1966. (SPAQuE, 2009). In 1959, up to 48 people were employed in the exploitation (Verdi, 1995). ***Figure 14*** displays an aerial photography of the site taken in 1963 and shows the space configuration of the former landfill site.

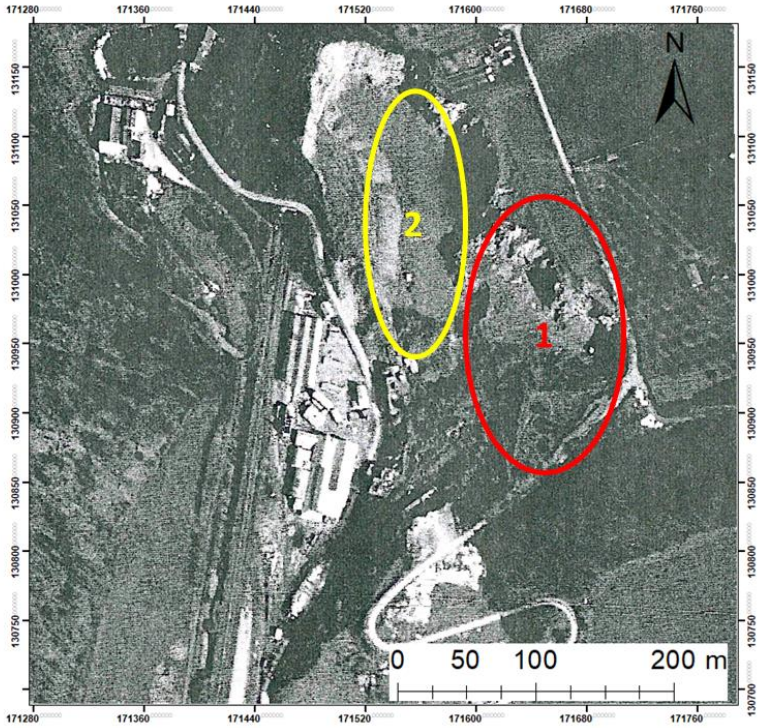

Figure 14. Aerial photo of the site in 1963 (Adapted from Verdi, 1995)

In 1967 the site began to be used for landfilling. The first wastes discarded were residues of the production of acetylene coming from the "*Solvay"* company. Subsequently, ashes were massively landfilled. Although there is no evidence confirming the hypothesis, it was postulated that these ashes were coming from the "*Auvelais*" power plant. Most of the waste was disposed until 1976 and is principally located in the area approximately defined by the *zone 1* in ***figure 14*** (Verdi, 1995) An aerial photography of the situation in 1976 (***Figure 15***) allows a clearer view of the extent of waste deposited in that zone of the site. Considering *zone 2* (***Figure 14***), defined as the lower part of the site, the type of waste encountered was more heterogeneous, disposed in this area from 1987. It is important to notice that zone 1 and 2 are separated by a steep slope, rendering a continuous measurement between both parts complex.

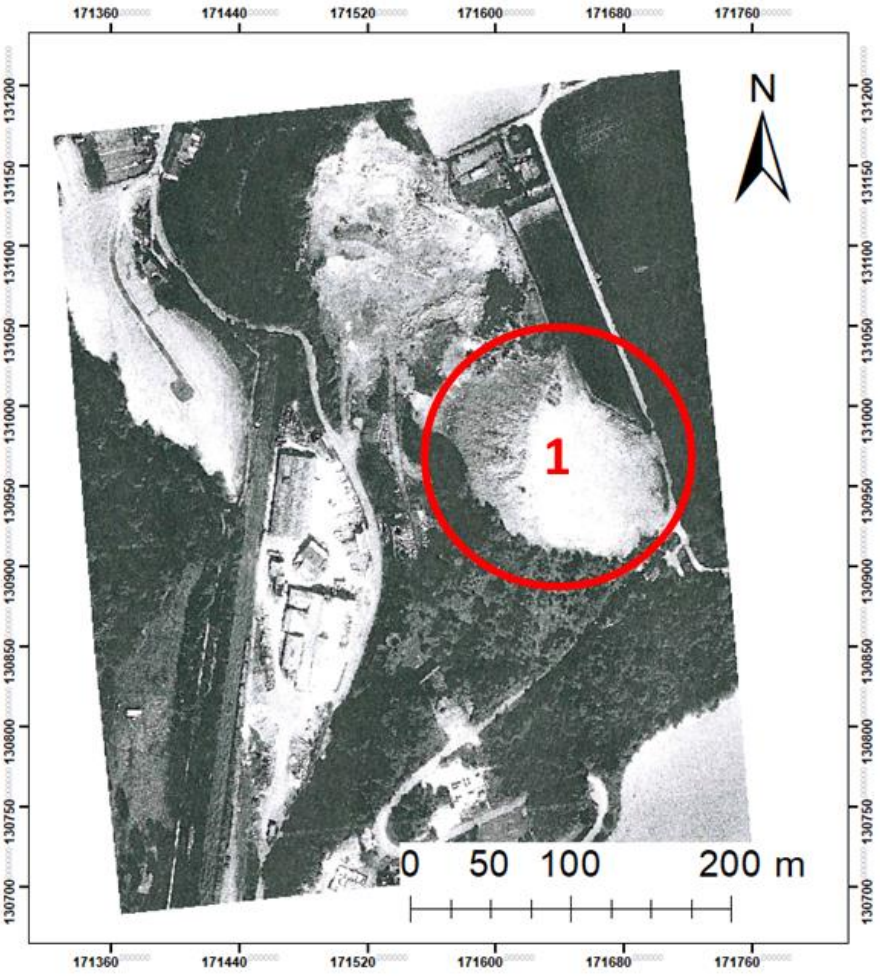

Figure 15. Aerial photo of the site in 1976 (Modified from Verdi, 1995)

In 1992, SPAQuE was given the responsibility of the site. In that scope, a first major investigation was undertaken in 1995 (Verdi 1995). Part of the site is classified as of *Great Biological Interest* (BGI) (SPAQuE, 2009), given that it has a well-developed flora and even hosts an Eagle Owl. Many investigations were performed in Onoz, such as trenches, boreholes and geophysical exploration, as it will be presented in the ***section 4.4***.

4.2 Geological and hydrogeological context

As already mentioned in ***section 4.1***, the material exploited in the quarry of Onoz was limestone of the "*Viséen*". More precisely, the formations outcropping in the region are called "*Onoz*" and "*Lives*". The formation of "Onoz" has a thickness from 120 to 150 meters at some locations. The basis of the formation is a black dolomitic clayey limestone, overlapped by a layer of massive limestone benches interrupted by small layers of dolomite. Closer to the surface, a layer of well-stratified and fine black limestone occurs, showing sometime clayey limestone, breccia or cherts (Delcambre & Pingot, 2008).

The formation of "*Lives*", which has a variable thickness that can reach around 100 meters, is mainly composed of stratified limestone interrupted with breccia all along the formation (Delcambre & Pingot, 2008).

From a hydrogeological perspective, the "*Onoz*" and "*Lives*" formations are part of a group of carboniferous limestones, forming a fractured aquifer with local karstification. However, the presence of some clayey limestone layers tends to decrease the hydraulic conductivity, which is usually considered as high. In the "Orneau" valley, i.e. the closest river to which the water coming from the landfill is flowing (Aeneryes, 2013), the aquifer can reach a thickness of around 400 meters (Ruthy & Dassargues, 2014). According to SPAQuE (2009), the aquifer is relatively close to the bottom of the quarry in the lowest part of the site (***Figure 16***). Nevertheless, the trenches excavated in the layer of wastes in the lower part, did not seem to reach the aquifer, within the first five meters (IRCO, 2018).

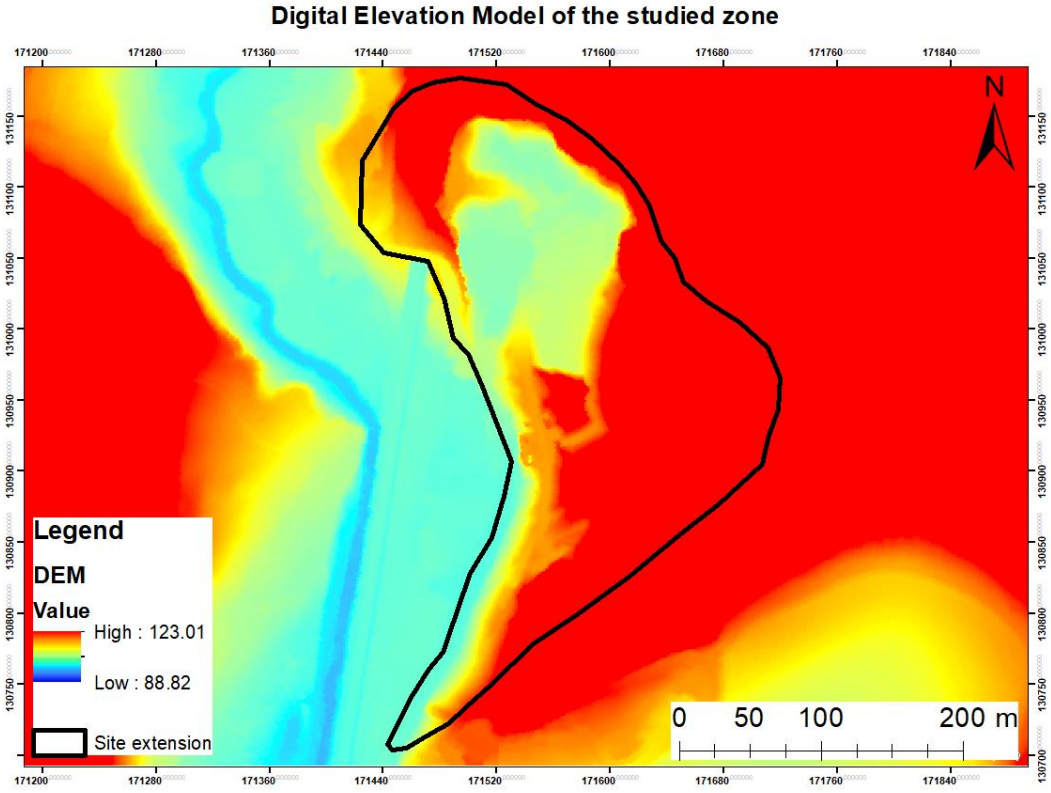

Figure 16. DEM of the studied zone (Modified from Service Public de Wallonie, 2018)

4.3 Current sectorial situation

From a sectorial point of view, the situation in Onoz is quite complex, given that the site is separated into two different zones. The western boundary, with the entry of the site, in considered as a mixed economic activities zone whereas the east part is considered as a green area, where the GBI zone is located and which is also considered a Natura 2000 zone (***Figure 17***). The complexity of the situation will therefore have to be taken into account for any future rehabilitation of the site.

Figure 17. Sectorial plan around the site. The extension of the site is delimited in blue, the purple area represents the mix economic activities zone, while the light green represents the green area zone (Adapted from Service Public de Wallonie, 2018)

4.4 Previous investigations

The first investigations in Onoz started in 1993 and ended in 1995 (Verdi, 1995). The first step of the survey consisted in 9 trenches dug with a mechanical shovel and a visual interpretation of the excavated wastes. Subsequently, chemical analyses were performed on 6 samples collected on the heaps of waste previously extracted (Verdi, 1995). The visual inspection allowed the distinction of different types of waste such as, shredders, waste coming from workshops of the "*Société Nationale des Chemins de fer Belges*" (SNCB), in addition to municipal and industrial wastes, along many others. Besides the elevated concentrations in minerals, the chemical analyses highlighted the presence of organic compounds, mainly in samples collected in the lower part of the waste deposit. Volatiles, semi-volatiles but also hydrocarbons were observed in several samples. Furthermore, leaching tests were carried out and demonstrated that Onoz wastes could be considered as dangerous, considering the different elements observed. Moreover, it was also determined that the groundwater was affected by the pollution occurring in Onoz. Indeed, analyses from 1993 mentioned that many elements such as aluminium, iron, cyanide, mercury concentrations exceeded the regulatory norms in the groundwater, especially downstream of the site (SPAQuE, 2009) The locations of the four piezometers is shown in ***annex 9.1.1*** Besides, no radioactivity was encountered on the site (Verdi, 1995). At this time, the waste deposit volume was estimated at around 185 000 m^3, with 168 800 and 14 700 m^3, in the upper and lower parts respectively (Verdi, 1995).

After some hydrogeological investigations, it appeared that the aquifer was located around the surface of the lowest point in the quarry. The average permeability from 1.03 10^{-3} m/s to 10^{-5}, could have led to some risks of contamination (SPAQuE, 2009). Therefore, from 2002 until 2015, SPAQuE verified the groundwater quality through samples taken at the four piezometers with one located upstream and the three others downstream of the site with one of these nearby the "*Orneau*" river. The analyses were achieved in different time-lapses, meaning in 2002, 2005, 2008 and 2015 (IRCO, 2018). They showed that although some contaminations in aluminium, mercury, nickel, chrome, nickel and zinc occurred (Aenergyes, 2013), the plume was quite diluted when it reached the river (SPAQue, 2009).

In 2012 another survey took place on the site. The survey ordered by “S.A Nonet” aimed to detect if any substance measured in the collected samples, was exceeding the new standards. These investigations, driven by RECOsol, were once again invasive and consisted in 15 trenches spread between the lower and the upper parts of the quarry. From the ten trenches, exacted to 5 m depth, three of them revealed a massive presence of lime in the lower part of the quarry, with a depth comprised between 1 to 3 m (RECOsol, 2012). The excavations also led to an estimation of the waste volume. RECOsol estimated the total volume of waste in the lower part at around 11 875 m^3 and with an averaged depth of 2.5 m. These 11 875 m^3, overlying 4 000 m^3 of lime are composed, for half, of municipal wastes, for a third of contaminated soil, while the rest is considered as inert (RECOsol, 2012).

In the upper part, the five remaining trenches were performed within a 5 to 6 m depth. After 50 cm of soil, the trenches brought to light a thick layer of grey ashes. The investigations delimited the surface of the ashes layer to 5 000 m^2, while the trenches never reached the bedrock. Consequently, only a minimal estimation of 25 000 m^3 of ashes in the upper part of the deposit could be hypothesized (RECOsol, 2012).

Chemical analyses were also performed on samples taken on the site. They demonstrated elevated concentrations, exceeding the required standard, for different substances and for some of them a concentration value that would normally require severe actions. These substances were heavy metals, mineral oils, chlorinated solvents, polycyclic aromatic hydrocarbons (PAH) and volatile organic halogenated hydrocarbons (VOHC). The highest concentration values were mainly observed in the lower part of the site and only highlighted heavy metal, mineral oils and chlorinated solvents (RECOsol, 2012).

The next investigation campaign was the first non-invasive survey and consisted in the application of different geophysical methods in the Onoz landfill. It was performed in the frame of the RAWFILL project by the *University of Liège* (ULiège). The project, funded by Interreg North-West and the Walloon Region, started in 2017 and was based on the growing concept of circular economy, applied, in this case, on the recovery of raw materials in waste deposits. The main purpose of the project was to define a framework allowing the development of appropriate strategies when it comes to landfill mining. The geophysical methods applied in Onoz had for purpose to demonstrate their usefulness in landfill characterization (Isunza Manrique et al., 2019).

The main objectives of the geophysical methods applied in Onoz were triple. The main one was to delimitate the lateral and vertical extensions of ashes in the upper part, which was missing from the previous investigations. The second one was the characterisation and the delineation of wastes in the lower part of the site. Finally, the third objective was to study the potential environmental pollution. The idea was also to use the geophysical results to define a sampling plan targeting zones of interest and allowing *in fine* to reduce characterization cost.

The first method employed was the “Frequency Domain Electromagnetic induction” (FDEM). The FDEM technique allowed to estimate the lateral extension of the ash deposit which spreads from the upper part of the site to the bottom part (Isunza Manrique et al., 2019). The second technique was a magnetic method to study the extension of wastes and detect potential buried magnetic objects in the lower part and the upper zone. Unfortunately, due to technical issues, the measurements performed in the upper part were a bit defective. The next method was the ERT technique coupled

with IP measurements. ERT aimed to cover a major part of the waste deposit in the lower zone of the site and consisted of three profiles enabling a distinction between the waste, the bedrock, some backfill, the ashes and lime. However, it was proved that, due to the very low and quite similar conductivities, it was almost impossible to distinguish lime from ashes. Still, it remained possible to distinguish the bedrock, with a high resistivity in the northern part of the deposit. A more conductive part at the expected depth of the bedrock was observed in the southern part of the profiles. The hypothesis raised at that time to explain the results involved the presence of a more fractured zone , a change in the lithology (it is well-known that the geological formation occurring in Onoz contains dolomite) or the presence of leachate. The lowest resistivity zone in the profiles was due to the presence of lime and ashes, that demonstrated to have a very low electrical resistivity as confirmed with laboratory experiments conducted on a sample collected on the site.

An intermediate resistive and heterogeneous zone occurred closer to the surface and was attributed to variable wastes. In terms of chargeability, the highest points in the profiles were due to the presence of metallic components in the waste, while the lowest points were corresponding to lime and ashes. In fact, all results coming from geophysical methods were overlapped with the previous invasive investigations, in order to properly calibrate and interpret the model. Moreover, a proper strategy in terms of trenches and boreholes was proposed to remove the remaining uncertainties, especially in the upper part of the site (IRCO, 2018).

Subsequently, a new invasive survey based on the geophysical investigation was performed in 2018 by IRCO. This time, ten trenches (seven in the lower part, three in the upper part) were conducted, while five boreholes were drilled (three in the lower and two in the upper parts). Moreover, four samplings were performed with an auger in the upper part. IRCO (2018) estimated the volume of the different wastes as follow: 3 400 m^3 of heterogeneous (municipal and inert) wastes in the lower part, 48 840 m^3 of lime, with 3 340 m^3 in the lower part and 45 500 m^3 in the upper part, and a total of 160 012 m^3 ashes, with only 212 m^3 in the lower part and the rest in the upper zone.

Each layer discovered during the excavation undergone chemical analyses and leaching tests. ***Table 4*** displays the most important polluting substances, present at elevated concentrations and observed during the tests performed on the different layers. The norms used at this time were the ones fixed by the soil decreed of December 2008, for the Threshold Value (TV) and the Value of Intervention (VI), and by the dataset of not-standardized pollutants for the Limit Value (LV). Although the elements observed in the table could be considered as alarming, the total concentration of pollutants is acceptable and the waste deposit is not considered as dangerous under the law (IRCO, 2018).

Table 4.Contaminants found in the different wastes in Onoz, with TV, LV and VI being respectively the Threshold Value, the Limit Value and the Value of Intervention (Generated from IRCO, 2018)

ZONE	LAYER	TEST	POLLUTING ELEMENTS AND NORM EXCEEDANCE*
Lower	**Waste**	**Chemical**	▪ PAH > **TV** (T1,T2,T4,T6, F2), **VI** (T1, T4, F2) ▪ VOHC > **TV** (T1,T6, F2) ▪ Heavy metals > **TV**,**LV**, **VI** (T1 to T7 F2) ▪ Mineral oils > **TV** (T1,T2,T5,T6,T7, F2), **VI** (T1,T3,T4,T6, F2) ▪ Polychlorinated biphenyl (PCB) > **LV** (T1,T6)
		Leaching	▪ Heavy metals > **TV** (Pb), VI (Cu), **LV** (Al, Sb) ▪ Mineral Oils > **TV**, **VI** ▪ Total Organic Carbon (TOC) > Signal value ▪ …
	Lime	**Chemical**	▪ Heavy metals > **TV** (T1,T6), **VI** (T6, F2), **LV** (T6, F3) ▪ Mineral oils > **TV** (T1, T6, F2, F3) ▪ PCB > **LV** (T1) ▪ VOHC > **TV** (T1, F3), **VI** (T6, F2, F3) ▪ Hydrocarbons > **LV** (F2, F3) ▪ …
		Leaching	▪ VOHC > **TV** ▪ Heavy metals > **TV** (Pb), **LV** (Al, Ba) ▪ TOC > Signal value
Upper	**Lime**	**Chemical**	▪ Mercury > **TV** (F4, F5), **VI** (F4) ▪ Aluminium > **LV** (F4) ▪ Mineral oils > **TV** (F4, F5), **VI** (F5) ▪ VOHC > **TV** (F4), **VI** (F4, F5) ▪ Hydrocarbons > **LV** (F4, F5) ▪ …
		Leaching	▪ VOHC > **TV** ▪ Heavy metals > **TV** (Pb), **LV** (Al, Ba) ▪ TOC > Signal value
	Ashes	**Chemical**	▪ Aluminium > **LV** (T8, F4, F5) ▪ Mineral oils > **TV** (F4, F5) ▪ PAH > **TV**, **VI** (F5) ▪ VOHC > **VI** (F4, F5)
		Leaching	▪ Arsenic > **TV** ▪ Aluminium > **VL** ▪ Fluorides > **VL**

* The different boreholes and trenches where the sampling occurred, are mapped in ***annex 9.1.1*** (***Figure 79***)

Furthermore, in January 2019, a post sampling geophysical survey was performed still in the scope of the RAWFILL project joining ULiège and the British Geological Survey (BGS). The idea of the survey was to refine the characterization of the site.

Another dataset was acquired with the magnetic method to verify the lateral extension of the lime and ashes deposits. The FDEM technique was used, only in the lower part of the site, at the foot of the steep slope, to verify any evolution in the lateral extension of the waste deposit and the cover of ashes and lime. In comparison with the last FDEM survey performed in 2018, the equipment available this time enabled to take measurements at two depths of 0.5 and 2.m, while in 2018 the depth investigated was at fixed 6 m. In contrast with the previous geophysical survey, two active seismic

datasets were acquired using the MASW technique and the refraction method. However, considering the mild quality of acquired data, affected by many factors, a more intensive overthinking on data processing had to be done (Isunza Manrique et al., 2019).

Most important results of the previous investigations, invasive and non-invasive are presented in the ***annex 9.1***. The conceptual model based on the previous surveys is displayed in ***figure 19***, while the map showing the location of the cross-sections is shown in ***figure 18***.

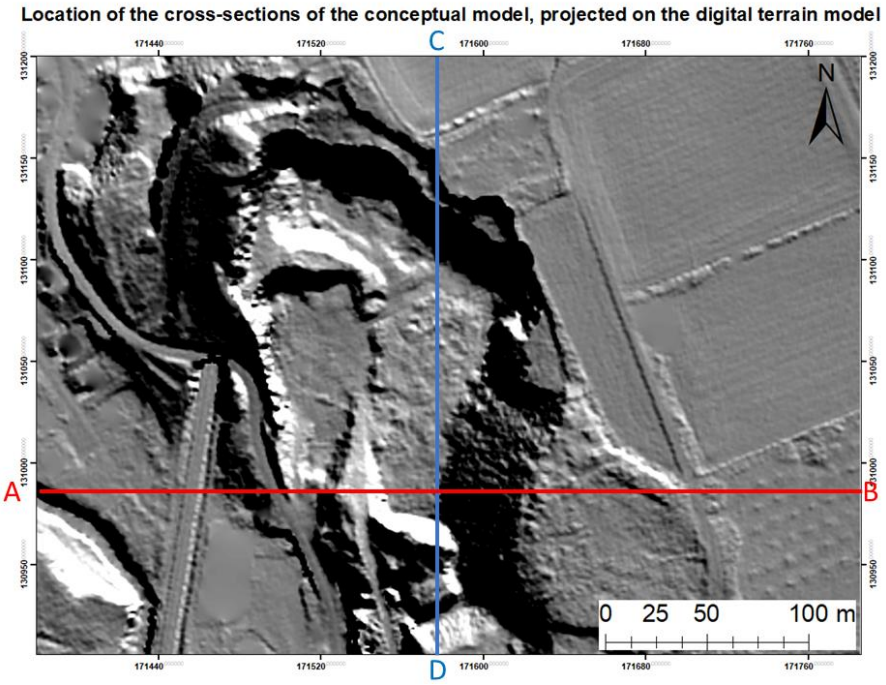

Figure 18. Location of the cross-sections of the conceptual model (Adapted from Service Public de Wallonie, 2017)

The conceptual model represented by the two cross-sections highlights the distinction between the heterogeneous waste and the lime/ashes layers. The lateral extension was expected to be well-defined thanks to the previous geophysical methods applied. Nevertheless, some knowledge enhancements could be required. Moreover, the lateral extension of the ashes and lime in the upper part was also well-described. Yet, a great doubt subsisted in the depth of this body in the upper part of the landfill.

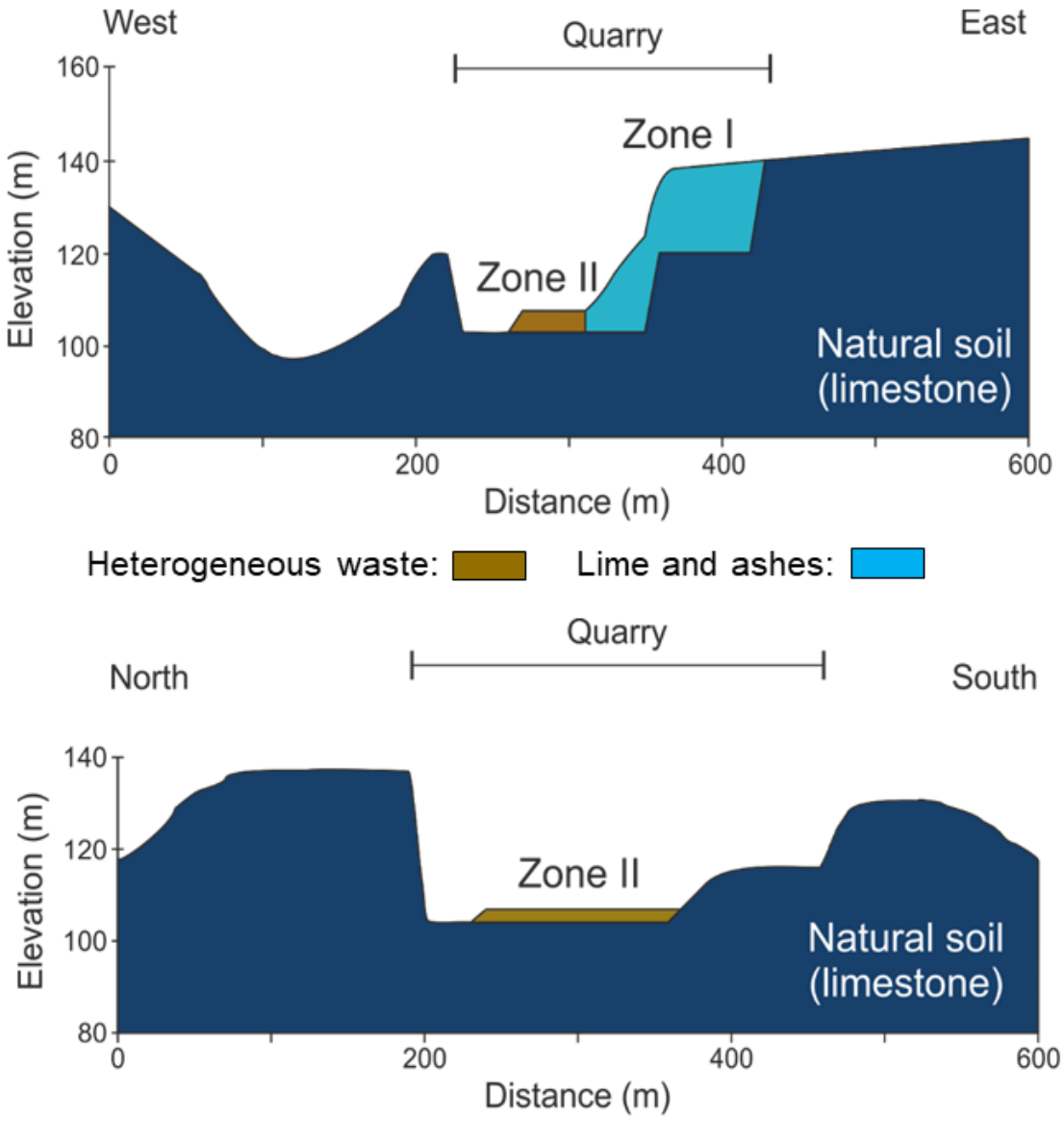

Figure 19. Cross-sections of the conceptual model (Modified from Verdi, 1995)

5 GEOPHYSICAL SURVEY DESIGN

As already mentioned, the geophysical methods selected in this master thesis consisted in a coupled 3D ERT and IP survey as well as a HVNSR survey of the entire site. The targeted zones are identified in ***figure 14***. The ERT survey was performed in zone 2 where heterogeneous waste were known. Optimally, the ERT would give an idea of the spatial, horizontal and vertical extensions, but also a distinction between wastes presenting different resistivity intervals. The HVNSR measurements were performed in both zones 1 and 2. In zone 1, the main purpose was to analyse if the technique could display any specific pattern useful in landfill characterization. In zone 2, besides the specific patterns, the objective was to give an approximate indication of the depth of the ashes and lime layers.

5.1 ERT/IP design

The ERT/IP survey consisted in four different profiles, disposed in the lower zone of the site, where the previous invasive and geophysical investigations demonstrated the presence of heterogeneous wastes. It has been shown that most of the 3D ERT designs leading to successful results, are performed using a structured and regular grid. Nevertheless, the abundant vegetation in some zones hampered the establishment of such a structured grid and this will often be the case in landfill or former industrial waste deposits. Consequently, the final configuration obtained was the unusual one displayed in ***Figure 20*** and corresponded to the locations where it was possible to place ERT cables. However, the applied design could still be considered as effective as further demonstrated through the computation of a forward model in ***section 5.1.3***. The profiles were all composed of 32 stainless steel electrodes, spaced by 3 m, leading to profiles of 93 m long each.

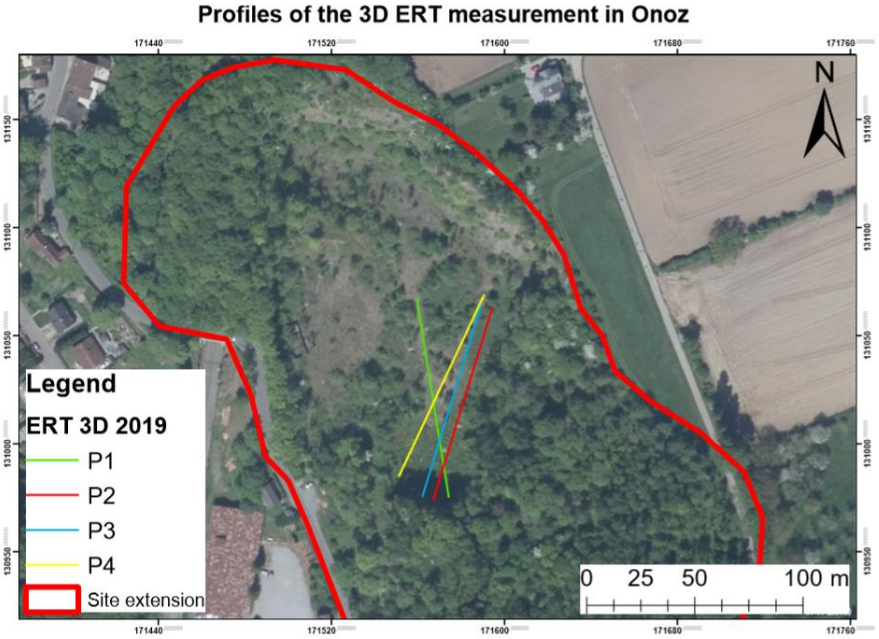

Figure 20. Aerial view of the site showing the configuration of the four ERT profiles (Adapted from Service Public de Wallonie, 2018)

It should be emphasized that the final aim of the survey was to compute a 3D model of the resistivity, hence the survey protocol had to be adapted compared to classical ones. The protocol used in Onoz was revised from to the one proposed by Van Hoorde et al., (2017) already mentioned in ***section 2.1.1***. It was chosen because its proven value in 3D surveys. In the present case, given that is was impossible to set parallel lines, they were simply considered as pseudo-parallel. The protocol involved both in-line and crossline measurements. The in-line measurements followed a standard dipole-dipole array. The maximal electrode spacing, *a*, corresponded to 30 m, while the dipole separation factor, *n*, was at maximum 6 (See ***section 2.1.1*** for explanation on *a* and *n*).

The crossline measurements also followed a dipole-dipole configuration. “Crossline” indicates that the potential dipole is in a different line than the current dipole. At first, the current was injected between two electrodes with a minimal spacing of 3 m and measured in a dipole with an offset of 3 m (i.e. the current injected between electrodes 1 and 2 of the first line will be respectively measured at the electrodes 4 and 3 of the second line). Afterwards, the potential measurement was shifted to the next neighbouring pair of electrodes. The maximum number of measurements per pair of current electrodes was equal to 6. As soon as data was acquired for one pair of current electrodes, the current was injected in the neighbouring pair. Following the first set of measurements for a certain electrode spacing, the latter was increased by 3 m. The maximum distance between two injecting electrodes was 30 m as for the in-line measurements. As the electrodes spacing increased, the shift between the injecting dipole and the potential dipole increased of the same distance. Once the potential acquisition was achieved for a line, the measurements started over at the next line. When all the pairs of electrodes of profile 1 had been used as current, the current injection shifts to the second profile that performed crossline measurements with lines 3 and 4. ***Figure 21*** displays a non-exhaustive example of the protocol used for two lines. The total number of measurements generated by the current protocol reached 5 300 measurements. Unfortunately, during the survey, a problem occurred on the 7th electrode of the first line. Thus, it was decided to remove the data acquired with this electrode, which reduces the dataset to 5051 measurements.

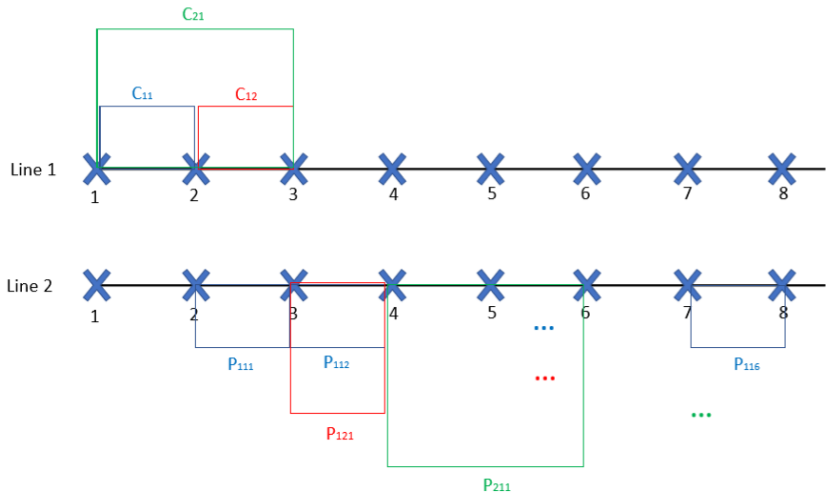

Figure 21. Example of crossline measurements between two lines of the protocol used for the ERT measurements

A dipole-dipole array was chosen for the measurements, since it is the most sensitive configuration to horizontal variations and had already proven its value in 3D acquisition (Rucker et al., 2009). Unfortunately, this was probably not the most suitable array to assess the vertical variations. Furthermore, given that the protocol involved in-line measurements, this enabled the computation of 2D profiles for the four lines, as it discussed later in ***section 6.1.2***.

The IP measurements were coupled to ERT data following the same protocol. The injection time was of 2 s. After switching off the current, the decaying voltage was measured after 0.01 s and at ten different time-lapses until 1.86 s, with the largest integration window of 0.58 s.

Data acquisition was performed with the ABEM Terrameter LS instrument and took around 5h. Moreover, a complete reciprocal dataset was acquired in order to carry out the most adapted error analysis.

5.1.1 Data processing of the 3D model

To check the data quality used for the 3D inversion, the raw dataset had to undergo a filtering depending on different parameters. The first parameter examined was the variance, directly measured by the instrument. Although no repeating measurement had been taken during the survey, the ABEM gave a relatively good approximation of the possible data variance, i.e. the quality factor given by the instrument. Regarding the histogram displayed in ***figure 22***, it was chosen to fix the threshold value at 10 % to remove the majority of the elevated values, while keeping an appropriate number of measurements. This led to the removal of 760 measurements.

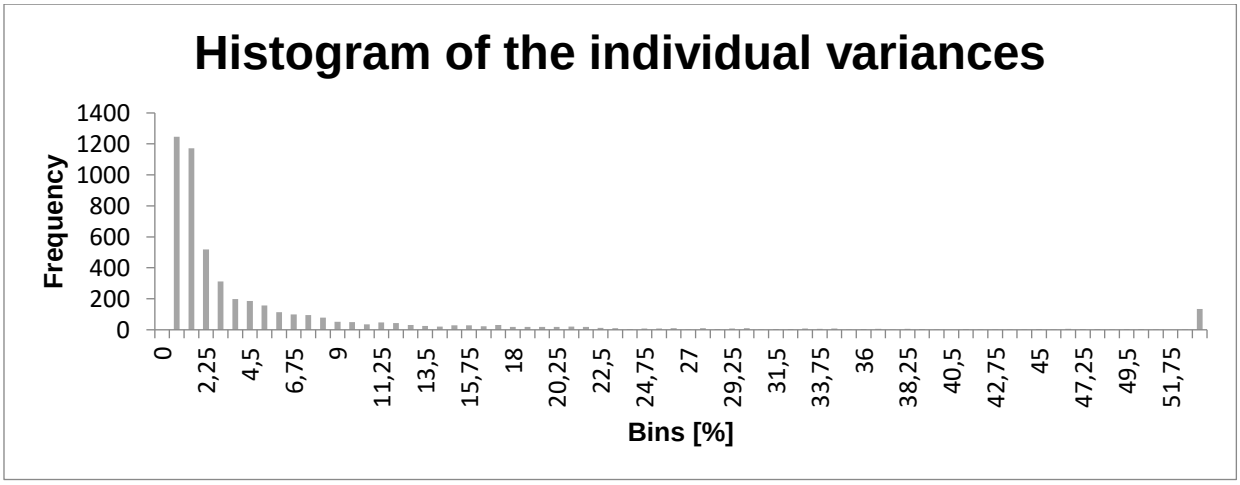

Figure 22. Histogram of the variance of each measurement given the ABEM Terrameter LS

The second criterion consisted in the relative error when the direct measurement was compared with the data acquired during the reciprocal. The histogram was plotted (***Figure 23***) and once again, after visual observation, the threshold was fixed to 10% for the same reason as for the variance. This time, 930 measurements were removed, which finally gives a dataset of 3361 measurements for the 3D inversion.

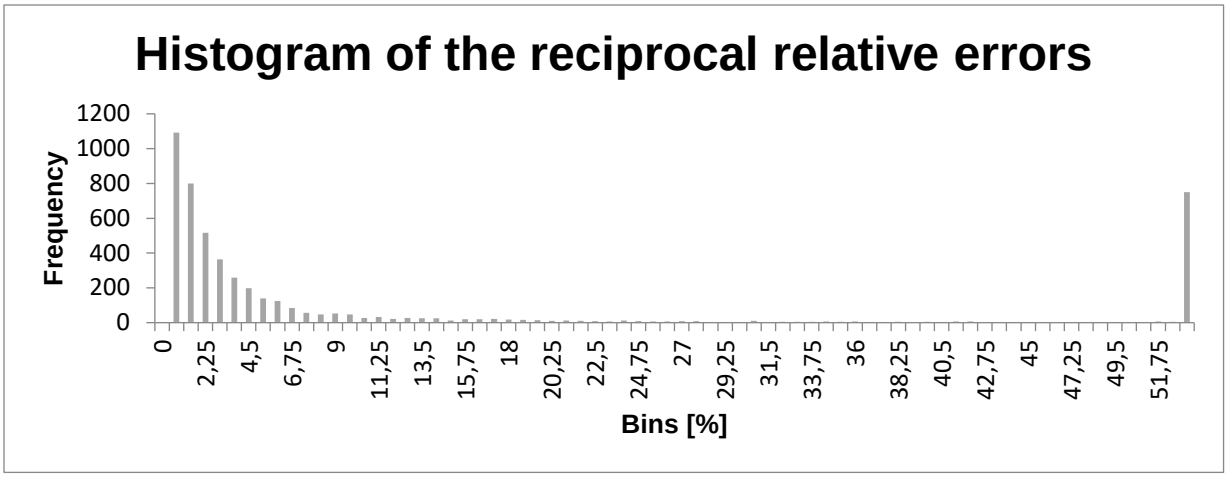

Figure 23. Histogram of the reciprocal relative errors

The next step was to incorporate the noise estimation in the dataset. This was accomplished by computing an error model, which is, in the frame of this master thesis, the Slater's model (see ***section 2.2***). The obtained error model is displayed in ***figure 24***.

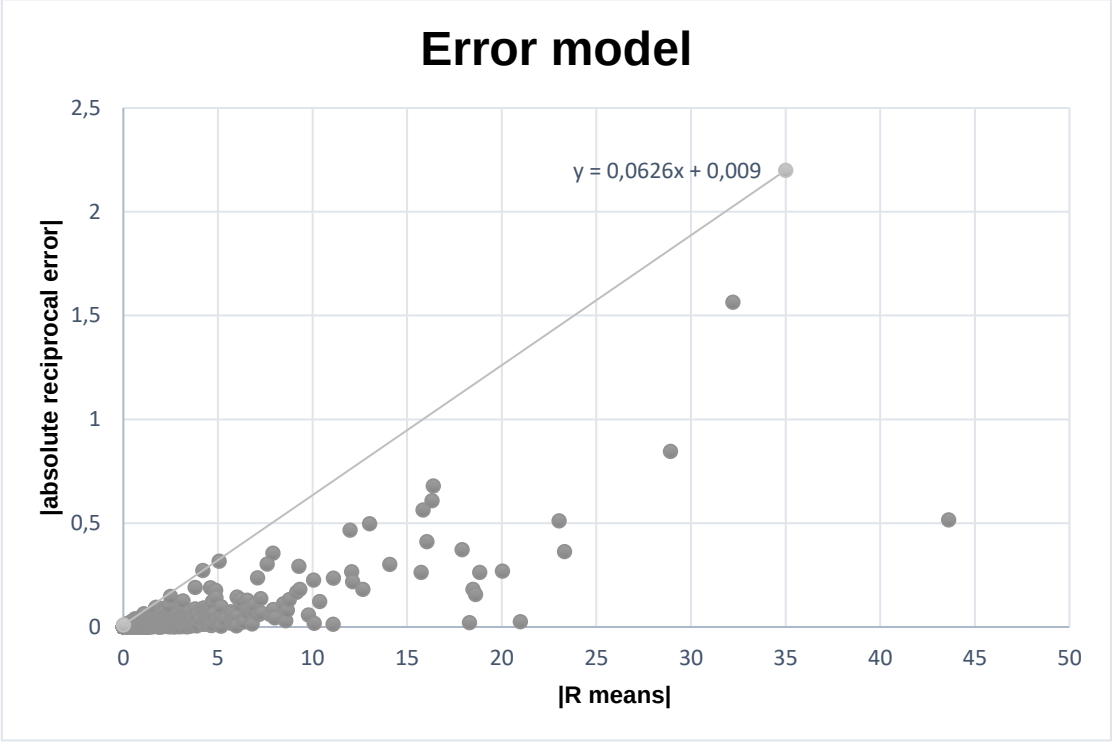

Figure 24. Error model following Slater's model

In order to have a better idea of the possible performances of the designed survey, a synthetic modelling of the Onoz site was computed. The stepwise approach followed can be described in this way:

1. Generation of different simplified resistivity models, based on the information acquired during the previous investigation. These models are the so-called "true synthetic models" Moreover, to better understand the impact of a thick and highly conductive layer on the global model, it was decided to induce a variation of certain

parameters of this layer, such as the depth, thickness and the resistivity. This was rendered possible in E4D by directly changing them in the mesh generation file.

2. Simulation of the synthetic data of each “true model” by running a forward model. The obtained data are called the “synthetic data”
3. Inversion of the “synthetic data”. Various inversion parameters were used, in order to understand their effect on the resulting model. The possibility of changing parameters was offered by E4D mainly by varying the solution constraints provided to the inversion algorithm. It was possible to provide these types of information through two main equations, i.e. the structural metric and the weighting functions. As its name implies, the structural metric is the equation used to impose a particular structure to the resistivity distribution. The weighting function determines how constraining the structural metric should be. E4D offers ten different structural metrics and four weighting functions. Additionally, it was possible to modify the relative weight applied to the constraint generated by the various combinations of structural metric and weighting function (Johnson et al., 2014). The inversion enabled the generation of various “inversed synthetic models”.
4. Comparison between the “inversed synthetic models” and their corresponding “true synthetic model”. This enabled to assess the value of the designed survey and to observe the different problems that could occur.
5. Computation of the DOI of the “inversed synthetic models” to observe how it evolves with various inversion parameters and to observe the different problems that could occur, when using this model appraisal tool.

After assessing the quality of the protocol used, the real data were inverted to obtain a model of the waste distribution, as well as to detect the bedrock in Onoz. First a so-called smoothed inversion was performed, followed by a blocky inversion in order to test different hypotheses regarding the geological structures. In E4D, an inversion is considered to have converged when a chi^2 of 1 is reached.

A 3D IP model of Onoz landfill was also displayed after inverting the results in BERT.

To get an idea of the reliability of the model obtained from the real data, the DOI was computed. As it will be shown during the forward modelling (***Section 6.1.3.3***), the DOI does not always provide an accurate information and can be impacted by various parameters. This could have been thoroughly checked by the sensitivity model, unfortunately the one provided by E4D displayed unrealistic results. In conclusion, a critical eye should be applied during the model interpretation.

5.1.2 Meshing

The following step consisted in generating an appropriate mesh reflecting the actual situation by exporting the data from the available *Digital Elevation Model* (DEM) (SPW, 2018, ***Figure 16***). Finally, a grid, composed of an elevation point every 2 m in the X and Y directions was generated in the E4D software. It was also important to set correctly the position of the different electrodes. ***Figure 25*** displays the resulting mesh.

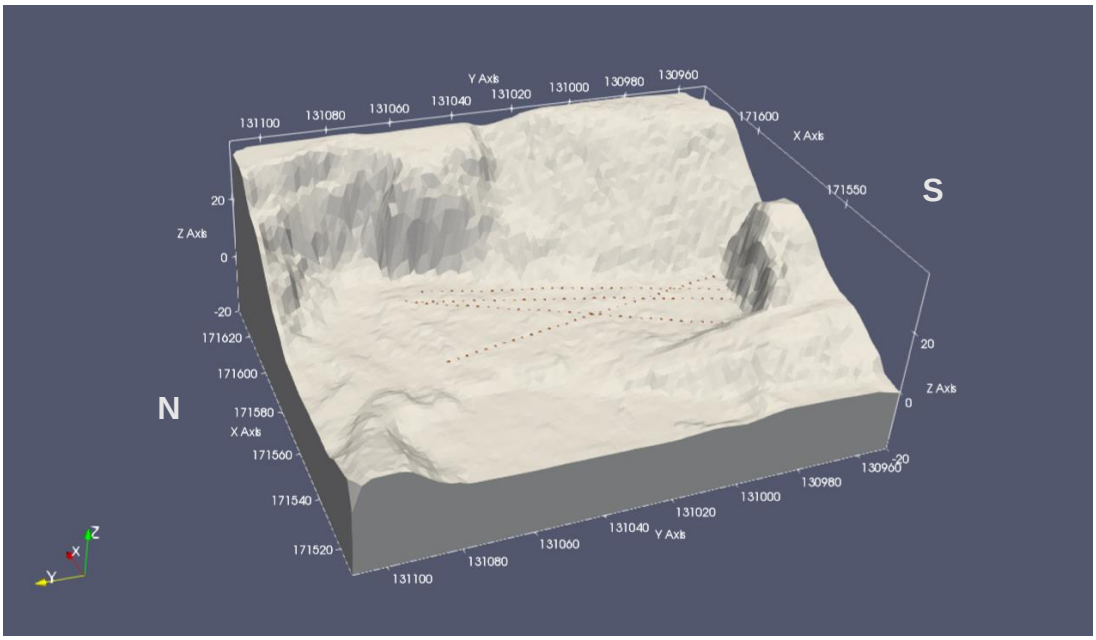

Figure 25. Generated mesh for the inversion

5.1.3 Forward model

As it is aforementioned, forward modelling is fully part of the survey design. It is noteworthy to remind that the forward model has for principal aim to generated numerical results of the survey that would have been acquired on a field such as the one modelled in the synthetic case. It is then necessary to perform an inversion with those results and to compare the “inversed synthetic model” with the known “true synthetic model”.

As already mentioned, it was therefore important to compute a synthetic resistivity model with conditions approaching those faced in Onoz. ***Figure 26*** displays the structures in the model which contains four different zones. The bedrock, which was placed at a depth of around 4 m in the entire model, was characterized by a resistivity of 3333 Ω.m, which is a high but usual value in case of non-altered limestone (Telford et al., 1990). The rest of the massif was represented with a resistivity of 200 Ω.m, characterizing an altered bedrock and unconsolidated soil (Telford et al., 1990). Then, two highly conductive zones, i.e. with a resistivity of 20 Ω.m, were placed within the model and represented the highly conductive lime and ashes. The first zone was a square of 100 m^2 situated in the middle of the survey and at the soil surface and with a thickness of 2 m. The second sector was delineated as a rectangle of 69 m to 59 m, which was placed in the south-eastern corner of the model, at the same depth as the first zone but with a thickness of 3 m. It is worth mentioning that the depth of layers indicated is compared to the lowest surficial point of the quarry. Both zones represented the presence of waste, such as lime ashes or municipal waste, which are known to be conductive. It was also important to place the electrodes, represented in red in the figure, at the exact same place as for the real survey, to validate the chosen geometry in the sake of obtaining a proper resulting model. The electrode configuration provided into E4D was the dipole-dipole used in the real survey, with in-line and crossline measurements as discussed in the ***section 5.1***.

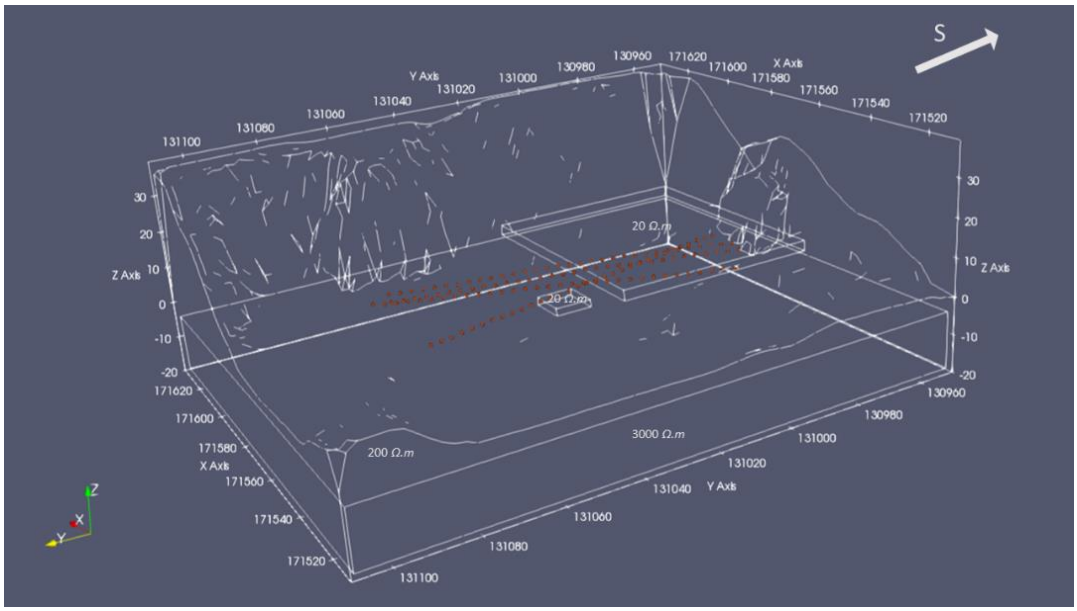

Figure 26. Numerical model used for the forward modelling

Figure 27 shows a cross-section from north to south, in the middle of the zone under investigation. It offers a better visualization of the different zones and for the next comparison with the inversion results.

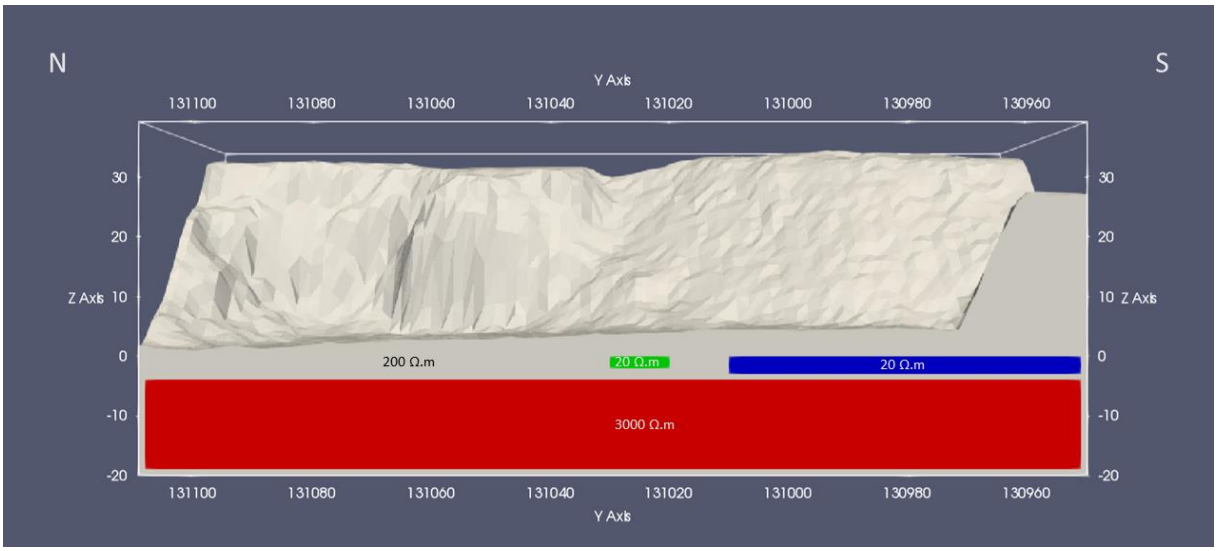

Figure 27. North to South cross-section of the forward model

5.1.3.1 Smoothness constrained model

The parameters of the inversion were chosen in *E4D*, in order to test a smoothness constrained inversion with relative weight equal to 1. The starting model was fixed at a resistivity around 3333 Ω.m. The inversion outcome is presented in ***figure 28***.

Remarkably, although the starting model was fixed at a resistivity around 3333 Ω.m, the whole model seems to have a lower resistivity at first glance. Taking a closer look at ***figure 28 A***, it is clear that the global model is affected by the highly conductive zones. Indeed, zones where the actual survey should lead to no change compared to

starting model showed resistivity lower than the starting model, i.e. 2300 Ω.m and with an enhanced effect near the conductive zones. This effect is even more visible when the cross-section (***figure 28 B***) is analysed. It is clear that the thickness of the conductive zones is overestimated compared to what it should have been in the benchmark. The generated resistivity model also indicates that the depth of the bedrock is even deeper than 20 m in the southern part of the model, which was not acknowledged in the synthetic model. Moreover, the part of the conductive layer beneath the small southern cliff is clearly undetectable since it was impossible to set electrodes there, due to the topography. It is also important to notice that the lowest resistivity is pointed at 57 Ω.m, showing that the resistivity of the two lenses increases due to the smoothing applied during the inversion. The application of a threshold value of 250 Ω.m, which corresponds to the resistivity assigned to the upper backfill/waste layer in the synthetic model with a certain increase caused by the smoothing, is applied to the model (***Figure 29)***. It exhibited, that the lateral extension of the zone with a resistivity below 250 Ω.m is restricted to a zone slightly bigger than the one covered by the electrodes (***Figure 29 A***), while it is further highlighted, that the depth of this layer, in the zone surrounding the thickest highly conductive layer, is overestimated (***Figure 29 B***).

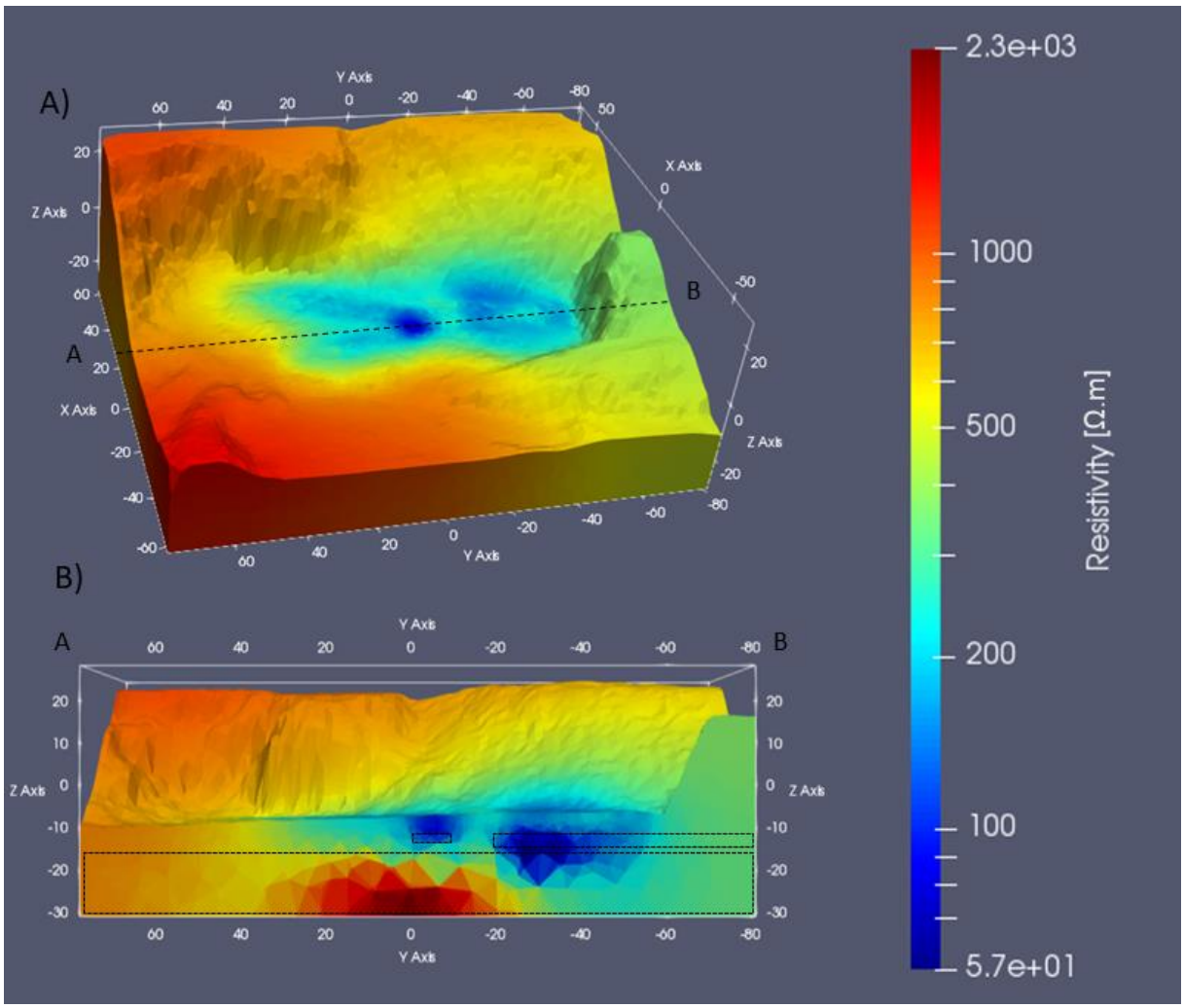

Figure 28*.* Results of the smoothness constraint inversion of the synthetic data. **(A)** Global vision of the resistivity distribution **(B)** cross-section along the dashed line of (A). The dashed line rectangles inside the cross-section indicates the position of the highly conductive lenses and the bedrock and are displayed to get a better idea of the reconstruction of the lenses.

At this stage, an important remark has to be done. The previously presented results were obtained after introducing a noise corresponding to the 5% of the simulated electrical resistance. To be in line with the reality of the field, it was decided to implement the noise computed from the error model, build with the reciprocal measurements and following the same pattern as defined by ***equation 10*** and in the present case:

$$|e| = 0.0626 * |R| + 0.009 \qquad (30)$$

Which corresponded to a relative error of 6.26% and an absolute error of 0.009. The new resulting images are shown in ***figure 30***, with ***figure 30 A*** showing the global model and ***figure 30 B***, the same cross-section as previously observed.

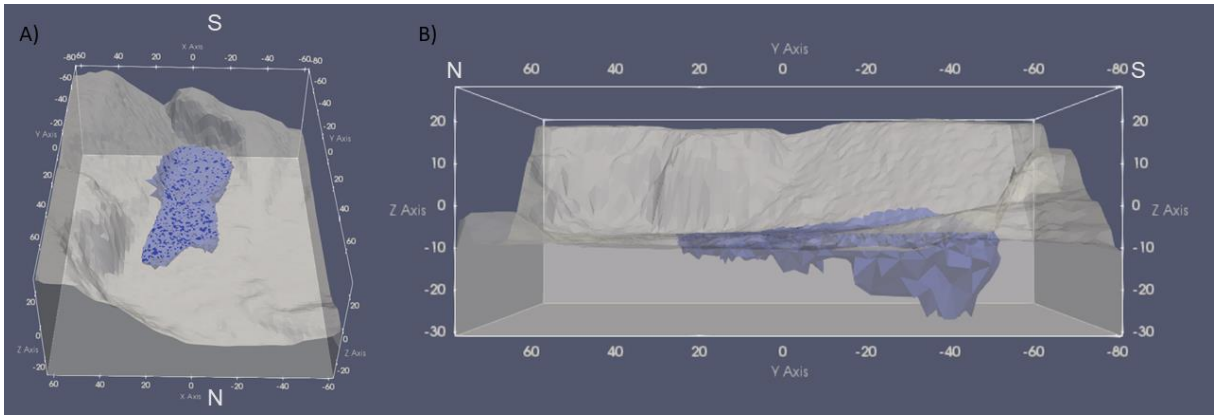

Figure 29. Application of a maximum resistivity threshold of 250 Ω.m on the model (zone in blue), **(A)** shows the horizontal extension, **(B)** the vertical extension

The differences are only moderate. The two highly conductive zones are still recognizable and the inversion software is still strunggling to model correctly the depth of the bedrock. The main difference is in the resistivity range, which is now between 60 Ω.m and 2 100 Ω.m due to the different weighting of the data. Considering these aspects and the fact that smoothing occurred during the inversion process, it is understandable that the rest of the model is being smoothed tending to 200 Ω.m, lowering the highest values and increasing the lowest one, especially where the sensitivity is probably the lowest.

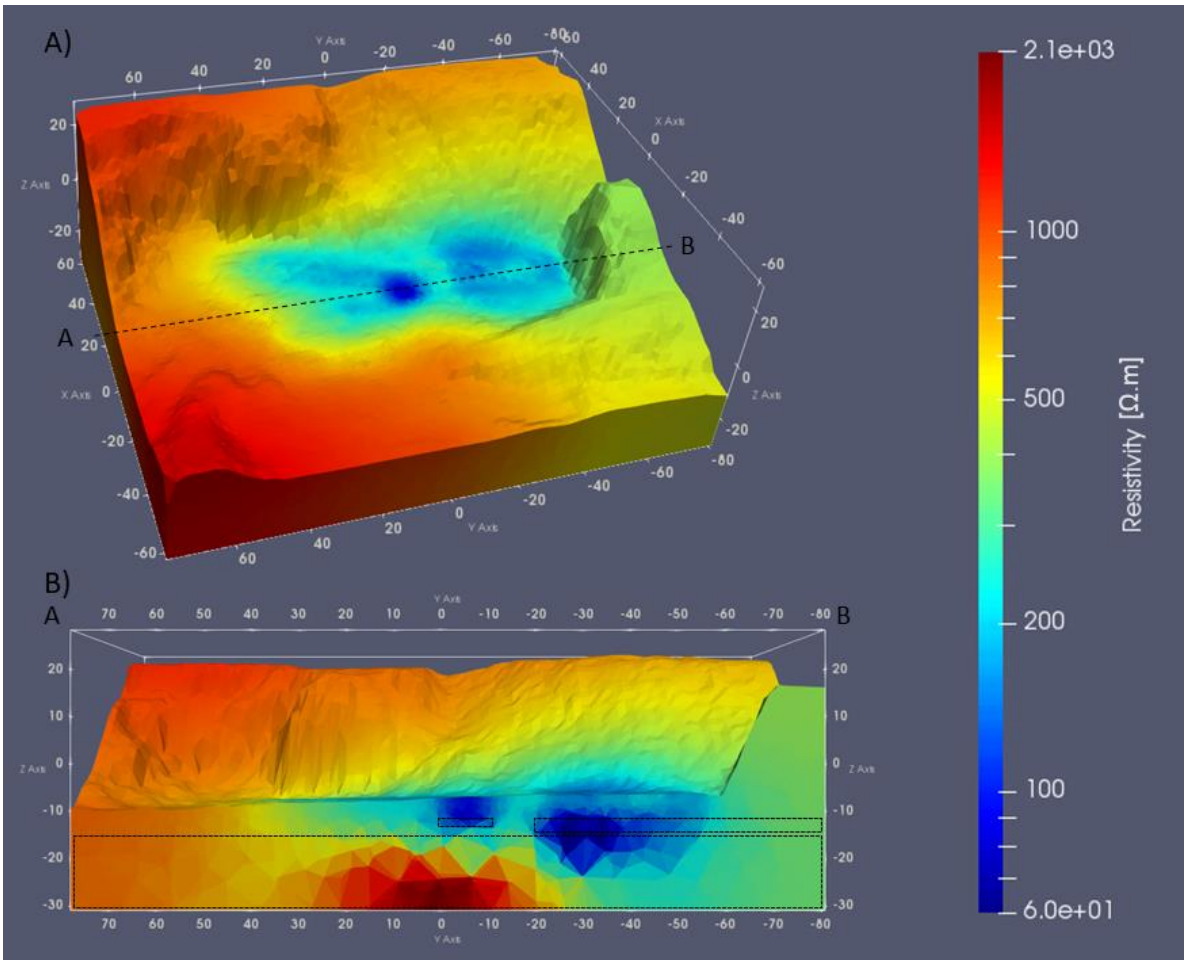

Figure 30. Results of the smoothness constraint inversion of the synthetic data with implementation of the error model. **(A)** Global vision of the resistivity distribution **(B)** cross-section of the dashed line of **(A)**. The dashed line rectangles inside the cross-section indicate the position of the highly conductive lenses and the bedrock and are displayed to get a better idea of the reconstruction of the lenses.

Another important aspect that has to be highlighted is that the line, encompassing all data, defined during the computation of the error model, is manually fitted, which introduces some subjectivity. It is therefore important to show how impacting is the choice of the error model. The error model could have followed, for the same dataset, the ***equation 31***

$$|e| = 0.048 * |R| + 0.07 \qquad (31)$$

The percentage error decreases, contrarily to the absolute error that increases. Looking at the new obtained model (***Figure 31***), it can be observed that the interval of the resistivity value is much more restricted than for the previous models. Indeed, it is visible that the lowest value stops around 130 Ω.m and the highest at 1200 Ω.m. This can be explained in the same way as earlier, i.e. by an increasing freedom for data and a smoothing tending to a resistivity of 200 Ω.m.

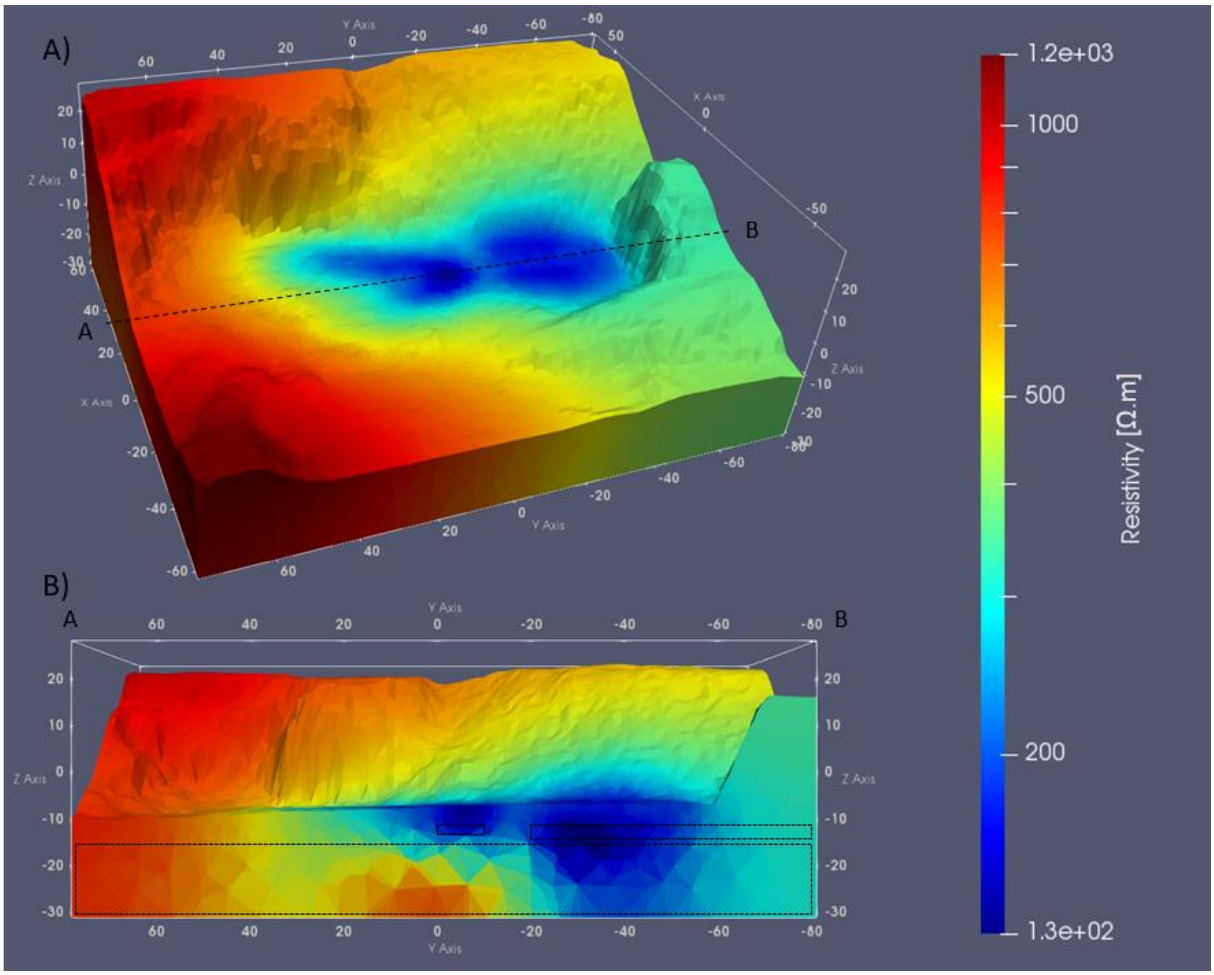

Figure 31. Results of the smoothness constraint inversion of the synthetic data with implementation of the error model. **(A)** Global vision of the resistivity distribution **(B)** cross-section of the dashed line of **(A)**. The dashed line rectangles inside the cross-section indicate the position of the highly conductive lenses and the bedrock and are displayed to get a better idea of the reconstruction of the lenses.

Here, the smoothing and the implementation of the error model lead to an increase of the thickness of the intermediate layer, further misrepresenting the real depth of the bedrock. It is also important to notice that the smoothing also impacts the resistivity of the bedrock, which is much lower than the actual bedrock value. It is therefore important to precisely set the error model.

It is now clear that the concerns emitted by Dumont et al. (2017) concerning the inability of the ERT to measure the thickness of a layer of waste with a high conductivity, are verified. Consequently, it was decided to perform a parametric study. Indeed, a layer with a conductivity of 20 Ω.m and a thickness of 3 m was representing an extreme situation compared to what is expected to be found in Onoz. Itw as thereafter decided to perform a parametric study to analyse the impact of varying physical parameters on the resulting images of the inversion process. Moreover, this exaggeration of the conductive zone could also be caused by an inappropriate choice of the inversion parameters. The type of constraints applied to the inversion and the relative weight allowed to the constraint are being also modified.

The first parameter analysed is the thickness of the conductive layer. First, both layers are assigned to a 2 m thickness and then decrease to 1 m and finally to 0.5 m. All the images resulting from this analysis are presented in ***annex 9.2 (Figure 85)***.

When the layer thickness is decreased to 2 m, the two most conductive zones are still distinguishable and are still visible in the middle of the intermediate conductive zone. However, the lowest resistivity occurring in the model is around 82 Ω.m, which is already much higher than the 20 Ω.m from the synthetic model. The fact that the lowest resistivity increases with a decreased thickness, indicates that it is clearly due to the smoothing applied during the inversion. Moreover, the highest resistivity also increases, up to 2 200 Ω.m, which pinpoints that the thickness of the conductive layer globally impacts the model. Even if the whole model is affected to a lesser extent, the exaggeration of the depth is still present, with a bedrock relatively unrecognizable under the largest conductive zone.

For the 1 m thickness model, the two conductive layers are yet barely distinguished from the intermediate conductive layer, with the lowest resistivity around 120 Ω.m, which is probably caused by the smoothness constrained inversion performed. The depth and the lateral extension of the layer is getting closer to the reality, with the bedrock more visible under the waste layer. However, the depth of the conductive layer is still overestimated, and the model is still generally affected. For the last thickness analysed, i.e. 0.5 m, the model is once again, less affected by the presence of conductive zones and the bedrock seems to get once again closer to the true one. However, below the biggest conductive layer, the bedrock does not appear clearly and a surrounding zone with a conductivity around 500-600 Ω.m still occurs instead. In the upper layer, the lowest resistivity is around 150 Ω.m, which indicated that the two highly conductive zones are almost completely absorbed by the intermediate layer of 200 Ω.m.

The analysis of the thickness of the conductive layers, shows that the conductivity of layers plays a key role in the image obtained from the inversion.

To summarize, the thickness impacts the global model, shown by an increase of the lowest resistivity and the growing development of the bedrock in the bottom part as well as a higher difficulty to distinguish the two highly conductive zones from the intermediate layer of 200 Ω.m. However, changes in the model, after modification of the thickness, are visible but relatively insignificant.

The next parameter under investigation is the resistivity of the waste layers. It has been proven by the previous geophysical investigations led by ULiège, that the three main types of materials found in Onoz, namely lime, ashes and waste, have a resistivity of respectively around 4.5 Ω.m, 45 Ω.m and between 10 to 100 Ω.m. (Caterina et al., 2019) In this way, it is decided to study the impact of an increased resistivity of the conductive layers from 20 Ω.m to 40 Ω.m, then to 60 Ω.m and finally to 80 Ω.m, which stay in the limit of the analyses previously performed by the University of Liège.

The modification of the resistivity assigned to the two layers, induces some minor changes in the model, which are, though, still perceivable. All resulting images are visible in ***annex 9.2, figure 86***. When the resistivity is doubled from 20 to 40 Ω.m, the resistivities of the global model becomes more restricted, with the highest one lowered to 2 000 Ω.m. Even though it is still too deep, the thickness of the intermediate layer is decreased, as well as its lateral extension. However, due to the chosen inversion parameters, the highly conductive layers appears to be smoothed. Indeed, due to the decreasing difference between the resistivity of the layers, the inversion enforces a higher similarity between the resistivity of neighbouring cells. Therefore, the

minimum resistivity in the cross-section of the model is around 100 Ω.m. However, it is clear that the most conductive zones are still approximately located in the inverted synthetic model. The highest resistivity decreases since the model is the most sensitive in the layer having a resistivity around 200 Ω.m.

When the resistivity passes from 40 to 60 Ω.m, the same effects are noticeable. Indeed, the depth and the extension of the intermediate layer are once again reduced. Moreover, the model is globally less affected and the highly conductive bodies are further smoothed causing a decrease of their size, even if the lowest resistivity remains around 130 Ω.m. The increase to 80 Ω.m, shows the exact same effects. ***Figure 32*** summarizes the effect of the resistivity changes in the conductive layers on the highest and lowest resistivities found in the model.

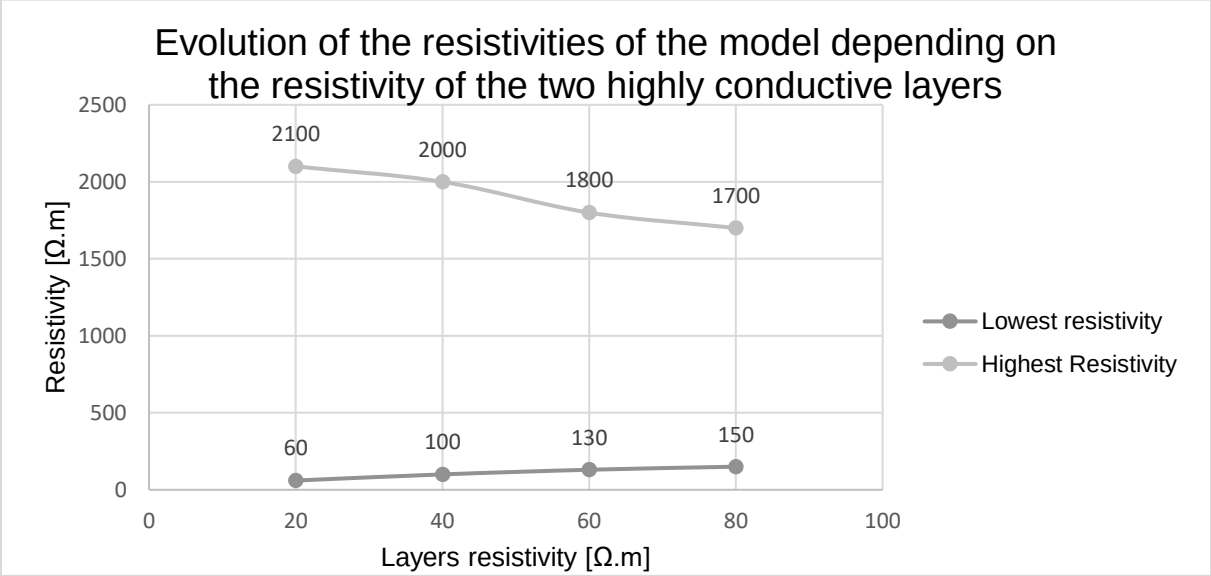

Figure 32. Evolution of the resistivities of the model depending on the resistivity of the two highly conductive layers

It is now clear that the resistivity and thickness of the highly conductive lenses, play a key role in the exaggeration of the spatial extension of the intermediate layer. However, the previous analyses also showed that the inversion parameters impact the resulting images as well. The best example is the progressive disappearing of the conductive layers. Presently, the role of these parameters is still not well understood and therefore, it is necessary to analyse their impact.

The first inversion parameter analysed is the so-called “relative weight” controlling the importance given to the specific model constraint during the inversion of the model. In other words, the more the constraints, defined by the structural metric and the weighting function, are allocated capabilities, the more the model will be impacted by the constraint. For the initial model in ***figure 30***, the relative weight was fixed at 1, which was the highest possible value. It is subsequently decrease to 0.5, 0.2 and 0.1. The obtained images are shown in ***annex 9.2 (Figures 87, 88, 89)***.

The same effects are visible at each decrease of the relative weight. The thickness of the layer of 200 Ω.m is decreased, given that the smoothing function, which is tending toward the layer of 200 Ω.m, is given less weight. However, even for the lowest value, i.e. 0.1, the correct value of the bedrock resistivity below the biggest highly conductive zone, is never reached. The interval of resistivity values is also

enhanced. As the smoothing is lessened, the parts of the model having less sensitivity are also less affected and remain closer to the starting model, which, as a reminder, was fixed at 3 333 Ω.m. When the weight is fixed at 0.2 and 0.1, resistivity values, slightly above this value, i.e. between 3500 and 4000 Ω.m, also occur in the different models. In each model, the highly conductive zones are still visible, even if the decrease in the relative weight allocated to the smoothing constraint leads to numerical artefacts with a very high conductivity.

The analysis of the relative weight demonstrates that it plays a major role in the diverse interpretations that could be done from a single dataset. However, it also shows that, even when the smoothing is decreased, the problematic influence of the thickness and conductivity of the layers cannot be overcome. The depth of the intermediate layer between the highly conductive zone and the bedrock is, in this way, still overestimated.

5.1.3.2 Blocky inversion model

The next step consists in the so-called “blocky” inversion. This type of inversion enables the creation of models that will be split into different regions with their own relatively constant resistivity and separated by sharp boundaries. This enables a sharp delimitation between elements having a relatively large resistivity difference. Generally, smoothing is the most used inversion constraint. However, considering the characteristics of the surveyed zone, the blocky inversion seems more appropriate inversion procedure. Indeed, like Loke et al., (2003) tended to prove, a blocky inversion shows better results, when the subsurface resistivity changes are sharp, as it seems to be the case in the landfill. The resulting model is displayed in ***figure 33***. Of course, the image presented is rough, due the fact that smoothing is barely occurring. The resistivity of the unsensitive zone is similar to the one of the starting model but again a more resistive zone, i.e. between 3 500 and 4 000 Ω.m, occurs in the bedrock below the smallest highly conductive zone. Contrarily, below the other conductive zone, the resistivity remains below 3 333 Ω.m and is around 1 500-2 000 Ω.m. Besides, the estimation of the intermediate layer of 200 Ω.m is more adequate and nearly corresponded to the synthetic one. Furthermore, even though their shapes are quite asymmetrical and their resistivity too high, the most conductive zones are well recognizable within the intermediate resistivity layer, even if in the case of the smaller highly conductive body, the lens seems to be located deeper in the “inversed synthetic model” than in the “true synthetic model”. Finally, small patches of higher resistivity occur at the surface. This phenomenon actually appears when a measurement is performed between two nearby electrodes. The extreme values are linked to small artefacts that developed due to the absence of smoothing.

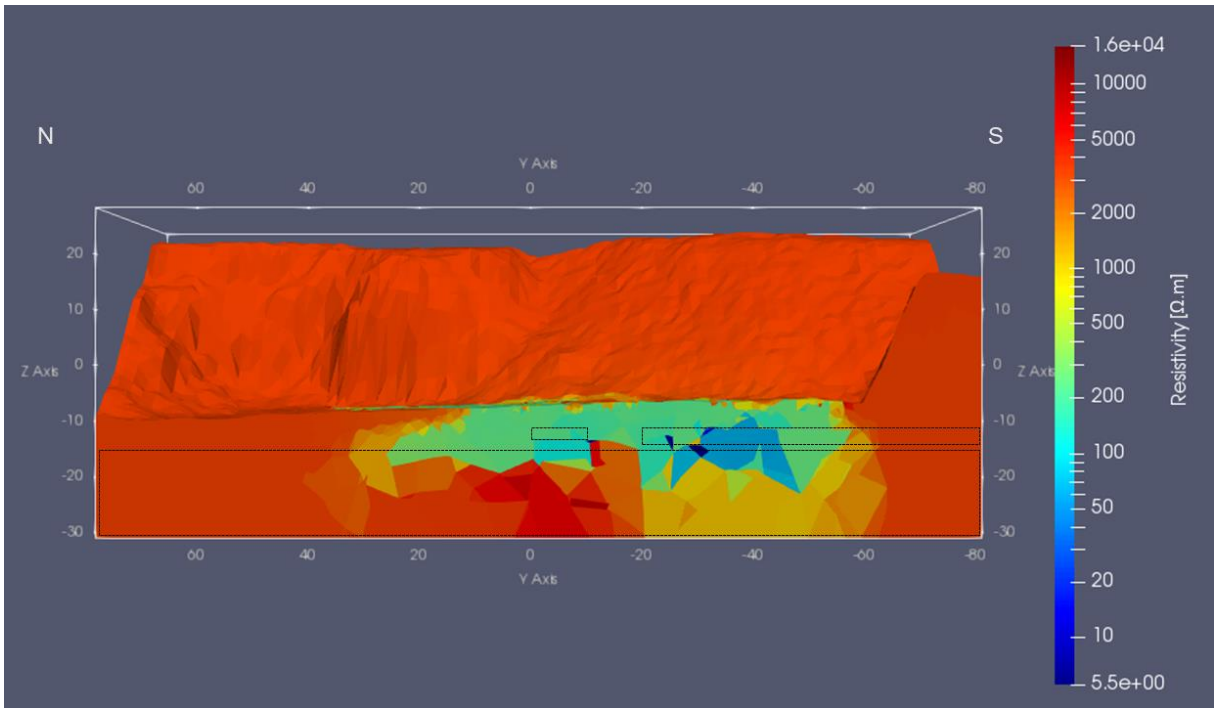

Figure 33. Cross-section of the inversed synthetic model obtained from a blocky inversion. The dashed line rectangles inside the cross-section indicate the position of the highly conductive lenses and the bedrock and are displayed to get a better idea of the reconstruction of the lenses.

The blocky inversion appears as an appropriate way to perform a delimitation of the different zones, showing the best results in terms of bedrock depth and thickness of the conductive layers. However, the roughness of the resulting image, partially due to the irregular mesh, and the apparition of artefacts can be seen as exclusion criteria in terms of quality. In conclusion, it is interesting to perform both, smooth and blocky inversions on the given data, to give a better insight of the field faced in Onoz.

5.1.3.3 DOI

As previously mentioned (***section 2.3.3***), due to unsolved problems occurring within the software and the challenging computations required, it remained impossible to obtain a consistent sensitivity model. Therefore, to appraise the quality of the models, one needs to resort to DOI. As previously stated (***section 2.3.3***), the DOI is computed regarding two different reference models, ideally surrounding the average value of apparent resistivities. This average was estimated at around 250 Ω.m, it was therefore decided to use values surrounding this average value, i.e. 25 and 5 000 Ω.m for the reference models. During both inversions, the starting model was fixed at the same value as the reference model. The DOI was performed with three different inversion settings. The first one was the smoothed constrained inversion, the second one still using a smoothness constraint but with a lower relative weight of 0.2 and finally, the third one was a blocky inversion. All the results obtained are presented in ***annexe 9.3***. The threshold value under which the zone is considered to be sensitive, was fixed to 0.1 (Oldenburg & Li, 1999). In the first case, DOI is clearly overestimated. Indeed, it is indicated as sensitive in zones, where it was demonstrated that the inversion results were distorted and impacted by the highly conductive zone situated above. The DOI is also overestimated in the zone where the resistivity indicated a higher value than 3 000 Ω.m. The DOI performed with the lowered relative weight also displays an overestimation of the zone of sensitivity. However, it shows a more realistic

zonation in the part of the model where the bedrock is showing higher value than it should. Indeed, a smaller part of this zone is now considered as sensitive. Unfortunately, the DOI is still overestimated in the zone below the biggest highly conductive layer. The DOI from the blocky inversion, also displays an overestimated sensitive zone, which is additionally quite rough and scattered.

To conclude this section, the results shows that a highly conductive zone, with a certain thickness is distorting the zone below, by creating a false higher conductive zone than the real occurring bedrock. Furthermore, no perfect inversion parameters were found to bypass this problem. It is therefore interesting to perform different kinds of inversions with modulated parameters to gather information. Finally, the DOI is also clearly impacted by the highly conductive zone and remains qualitative. It remains therefore crucial to have a critical eye on the resulting images, to avoid misinterpretation.

5.1.4 Data processing of the 2D models

The computation of 2D ERT models is not the principal aim of this thesis. However, it remains interesting to compute these models and to compare them to the 3D model and see if a good matching can be observed. As already mentioned, four profiles were implemented during the 3D survey. Therefore, it was possible to compute four 2D profiles, by extracting the in-line measurements of each profile from the global survey and by inverting them in RES2DINV.

For the data quality, the filtering applied was different than the methodology applied for the 3D model and concerned mainly the IP measurements. Series of criteria were applied, using a *Matlab* script, in order to obtain the most appropriate dataset. The first criterion was to verify that the chargeability measured during the first window was not above 1000 mV/V or below -1000 mV/V. The second point was to assure that all the chargeabilities measured during one measurement were all of the same sign. The last criteria concerned the fitting to an exponential function. The curve generated by the different chargeability at each window had to fit a decreasing exponential function and the limit of the coefficient of determination R^2, expressing the fitting to the exponential curve, was fixed at 0.8. At this point, the integral of the chargeability curve was computed using the *trapz* function, supplied by *Matlab.* Afterwards the results were introduced into *RES2DINV*. Within the software, a last filtering was applied, by exterminating manually data points that exhibit inconsistent values compared to the neighbouring points. Besides this possibility, after the inversion, *RES2DINV* offered to trim the dataset depending on apparent resistivity percentage error, if an appropriate *Root Mean Square Error* (RMSE) was not achieved. The RMSE was considered as a reasonable below 10%. ***Table 5*** summarized the final number of measurements used to perform the inversion. ***Figure 34*** summarized the methodology for obtaining the most appropriate dataset for the 2D profiles, using P1 as example.

Table 5. Number of measurements used for each 2D profiles

NUMBER OF MEASUREMENTS USED FOR EACH 2D PROFILES				
Profile	1	2	3	4
Initial number	458*		530	
Final number	339	322	341	396

* The initial number of measurement is smaller for P1 than for the other because of the defective electrode n° 7

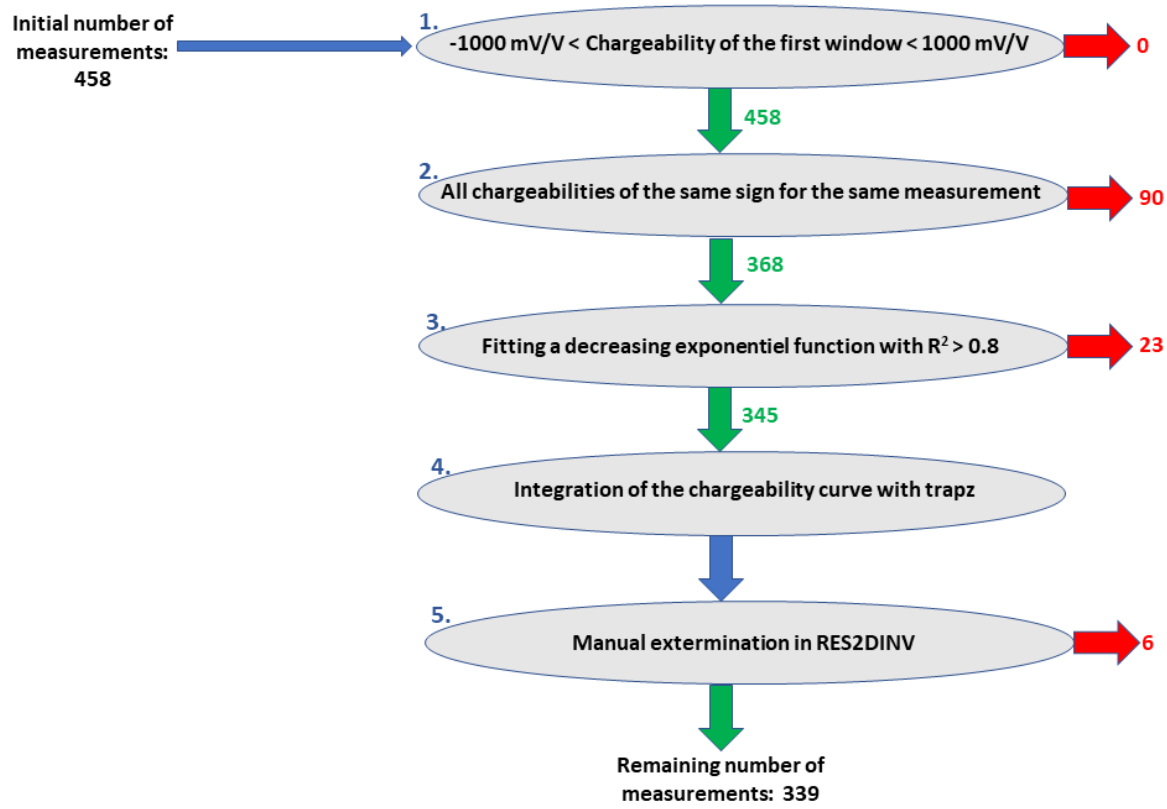

Figure 34. Methodology applied for the obtention of the best dataset for the 2D inversion, using P1 as example

Before performing inversion, it was decided to refine the model mesh. Indeed, given the high resistivity variation occurring in the studied area and due to the heterogeneity in materials in the ground, it was important to refine the model in order to stick as close as possible to the reality. The width of the cells used for the inversion were therefore half the width of the spacing between two neighbouring electrodes, i.e. 1.5 m.

Concerning the inversion, the choice of a robust inversion appeared to be the most logical. Indeed, as already mentioned for the 3D model, the values of the resistivity in a landfill can be highly variable. Moreover, the different zones in a landfill are often delineated by sharp boundaries. In this way, it was decided to select a robust inversion for both model and data constraints.

Finally, after performing the inversion procedure, the results were extracted in a "*.vtk*" format to be visualized in Paraview. This enabled to replace the X and Y coordinates, by the actual coordinates, rendering possible a crossing of the four profiles and an optimal comparison.

Furthermore, the IP measurements were also inverted and modelized into four 2D profiles. As mentioned in ***section 2.3.2***, RES2DINV offers different possibilities for the IP inversion method. In the present case, a separated inversion, meaning that the IP is kept fixed during the resistivity inversion, was chosen. This could be helpful in the determination of the different wastes constituting part of the surficial layer in the landfill of Onoz. The type of inversion is the same as for the resistivity, meaning a robust inversion.

5.2 HVNSR design

For a complete coverage of the site, it was necessary to gather a maximum of survey points, especially in areas of interest. For an optimal comprehension and interpretation of the results, the site was divided into two parts separated by the steep slope on site (***Figure 35***). In the lower part, previous HVNSR measurements were performed by the ULiège team and myself. In both zones, a random sampling was applied. The devices used for the survey were a “CityShark microseismic” station and a “Lennartz Electronic LE-3Dlite sensor”, having a sampling frequency of 200 Hz. The sensor was directly set on the ground and was levelled at each point. The recommendations of the SESAME (2004) were thoroughly considered. However, given various constraints on the site, some adaptations were done. Indeed, measurements near trees were unavoidable and the weather conditions were not always optimal, considering that most of the data were acquired in April 2019. Furthermore, the presence of several airports in the surrounding area also created some disturbances. Moreover, in order to ensure data quality and get a maximum amount of stable windows, each measurement lasted 25 min. In total, 33 measurements were added to the previous 17 measured points in the lower zone, while 18 were taken in the upper zone, yielding a total number of 68 points surveyed.

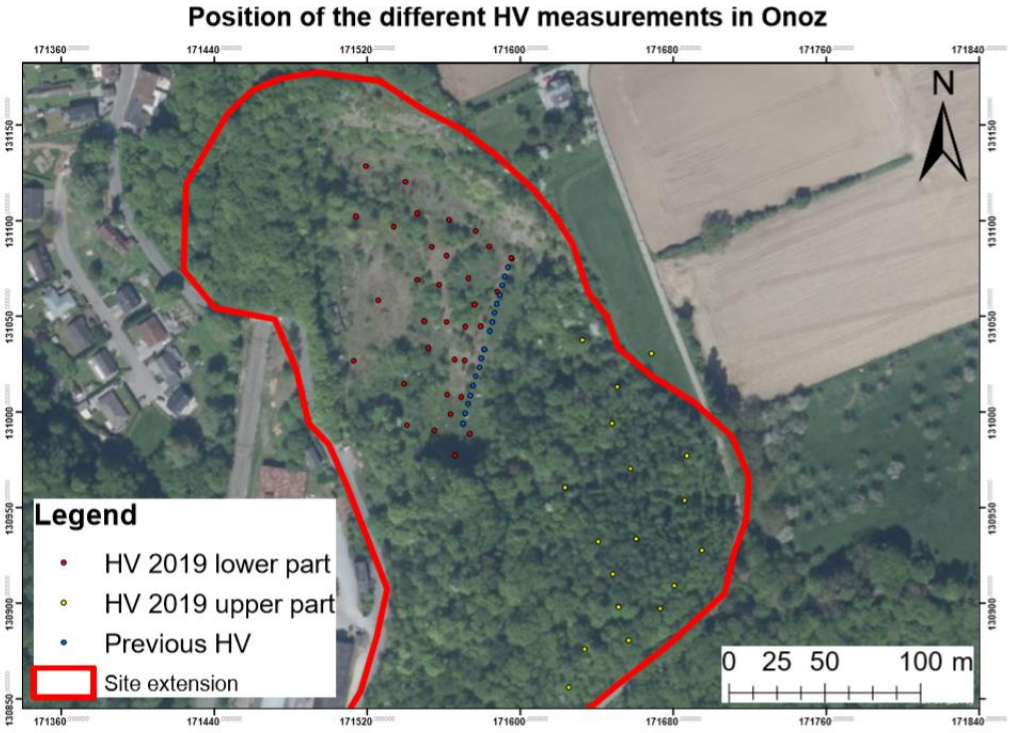

Figure 35. Position of the different HV measurements in Onoz (adapted from Service Public de Wallonie, 2018)

The next step was to process the acquired data. This was achieved by using the "*Geopsy"* software. The output frequency was focused on an interval from 0.5 to 50 Hz. Indeed, it has been proved, that above 25 Hz, most of the frequencies do not have any interest for subsurface characterization (SESAME,2004). The length of the selected stationary windows varied between 15 and 25 s, in order to obtain a sufficient amount of windows. The auto-selection of the windows was enabled by the algorithm used, which detected the transient periods and discarded them. The detection such periods is possible by comparing the short term average (STA) and the long term average (LTA). As its name implies, the STA represents "*the average level of signal amplitude over a short period*", i.e. in the present case 1 s (SESAME, 2004), while the LTA represents the same effect for a longer time frame, which was fixed to 30 s. To get rid of the transient periods, the ratio STA/LTA had to be limited by a certain threshold, which was fixed at 2.5. Very low amplitudes also needed to be eluded. Consequently, a minimum threshold of the ratio was fixed to 0.2. Moreover, no overlap between the stationary windows was allowed. For other parameters, the recommendations of SESAME (2004) were followed, meaning that the smoothing of the Fourier transformation was made by the "Konno & Ohmachi" smoothing, which enabled a better correlation between the S-waves and the H/V ratio (Konno & Ohmachi, 1998). Also, the merging of the two horizontal components was performed with the squared average. Finally, the number of samples taken on the H/V ratio graph was fixed at 100.

The next step for both modelled zones was to build a 3D block of the resonance frequency. The points were placed on a grid depending on their X and Y coordinates, while the Z axis represented the frequency. The colour map therefore depended on the amplitude of the different frequencies. To provide information between the different measured points, an interpolation was performed with *Matlab*. This enabled the delineation of different zones depending on the resonance frequency.

Then, depending on the location on the site, the protocol was adapted. Indeed, for the lower part, the heterogeneity of the waste rendered the approximate calculation complex. It was therefore decided to test the applicability of the method in such environment by comparing the obtained H/V graphs to the logs of the many trenches and boreholes previously drilled. In this way, it was possible to check if a clear relation existed between the results of the HVNSR and the composition of the wastes in the ground. Once the relation was established, it was possible to define the zonation of different waste "patterns" regarding the results given by the HVNSR.

Concerning the upper part, it was subdivided into two distinct zones. Indeed, as seen in ***figure 15***, each zone was used for different spilling activity. The first, which concerned the twelve northern measurement points in the upper zone, was used for the storage of lime and ashes, while the second defined by the 6 southern points had an undefined use. Indeed, the photography of 1963 (***Figure 14***) showed that the zone had undergone some activities, but the photography of 1976 (***Figure 15***) indicated that it was already backfilled and that the vegetation had already reclaimed its rights.

In the northern part, two HVSNR points were collected specifically in the immediate vicinity of two boreholes drilled by IRCO in 2018. Results were compared with the logs of these boreholes, enabling the calibration of the S-wave velocity for both materials. It is now important to notice that ***equation 29*** can only be used for the first surficial layer, i.e. in the present case, ashes. For a trimodal model, the formula applied to the second layer is the following (Pina-Flores et al., 2017):

$$f_1 = \frac{1}{4\left(\frac{H_0}{V_{s0}} + \frac{H_1}{V_{s1}}\right)} \qquad (32)$$

Where f_1, H_1 and V_{s1} are respectively the resonance frequency, the thickness and the S-wave velocity of the second layer. In this way, using the formulas and the logs of the two boreholes, it was possible to compute an approximation of the V_S for both materials and to subsequently apply it for the ten other points to compute an approximate depth for each layer.

The final work in this part was to compute an appropriate estimation of the waste volume. The lateral limits of the waste in the upper part were defined following the FDEM measurements performed in 2018 by the ULiège and the BGS (***Figure 36***). The line representing the limit of the zone was then split equally in multiple points and these points were assigned a depth of 0 m.

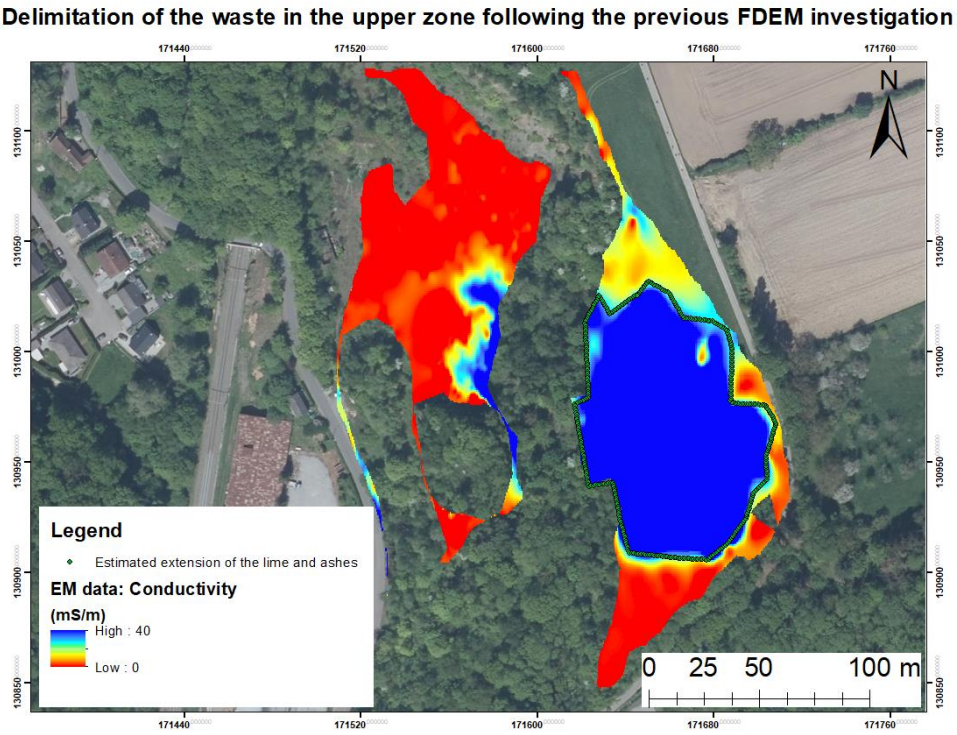

Figure 36. Map of the delineation of the waste in the upper part of Onoz landfill based on the FDEM results (Adapted from Caterina et al., 2019)

Considering the small amount of measurements performed inside the defined zone, a classical interpolation between each point, using for example kriging or the distance inverse was impossible and showed unrealistic results. The only possibility that could be applied was to use Voronoi polygons and more precisely the *Polytope-bounded-Voronoi-diagram* function in *Matlab* (Park, 2015). In the present case, the Voronoi diagram was used to assigned the same depth to a specific region surrounding a certain point. The polygons were defined such that all the points inside them were the closest to the central point. Then all the points constituting the polygon were assigned the same depth.

In the southern upper part, no boreholes and no information on the composition of the ground was provided. Consequently, major assumptions had to be done relying only on the FDEM cover performed during the previous geophysical investigations and based on visual observations done during the fieldworks for the master thesis.

6 RESULTS AND DISCUSSION

The purpose of this section is to show and interpret all the results obtained during the different fieldworks in Onoz. The actual data coming from the field investigations are analysed and, in addition to the different 3D models, four 2D ERT and IP profiles are presented for comparison. Finally, the results of the HVNSR method are displayed and analysed.

6.1 Inversion of the real ERT/IP data

6.1.1 3D Interpretation

6.1.1.1 3D ERT

After discussing theoretical models and the issues that could have occurred, the results of the inversion of the data measured during the fieldworks in Onoz are hereby considered. The first inversion is performed with a smoothness constraint in the E4D software. A second inversion, which is qualified as blocky, is also performed. The starting model is fixed at 3 333 Ω.m. and for an adequate quantification of the noise, the error model proposed in the ***section 5.1.1*** is used. It could have been interesting to perform an inversion with the individual reciprocal errors instead of the error model. This would have been a less conservative approach but could have avoid oversmoothing (Hermans, 2014). Unfortunately, the inversion was never able to converge.

In the first place, the global model resulting from the smoothness constrained inversion (***Figure 37 A***) is considered. It displays a separation of the model into two main parts. This separation is further highlighted by the histogram displayed in ***figure 38***, showing a bimodal distribution of the resistivity occurring in the model. The lowest resistivity peak represents the northern zone with a resistivity around 250 Ω.m, while the highest peak representing the other area, is reaching around 1 160 Ω.m. This can be explained as the first peak is mainly generated by the intermediate layer of 200-300 Ω.m that occurs in that part of the model (***Figure 37 B***). Furthermore, in this region, two highly conductive zones occur and as showed by the analysis of the synthetic model, they probably strongly impact the rest of the model. The higher global resistivity of the other part is due to the fact that it was the most distant zone of the conductive occurrences and above all, the depth of the bedrock is detected in this part. Therefore, the algorithm implemented into the software computes the zone where no information is available on the resistivity, taking these parameters into account, leading to a higher global resistivity for that zone, nevertheless, smaller than the one of the starting model.

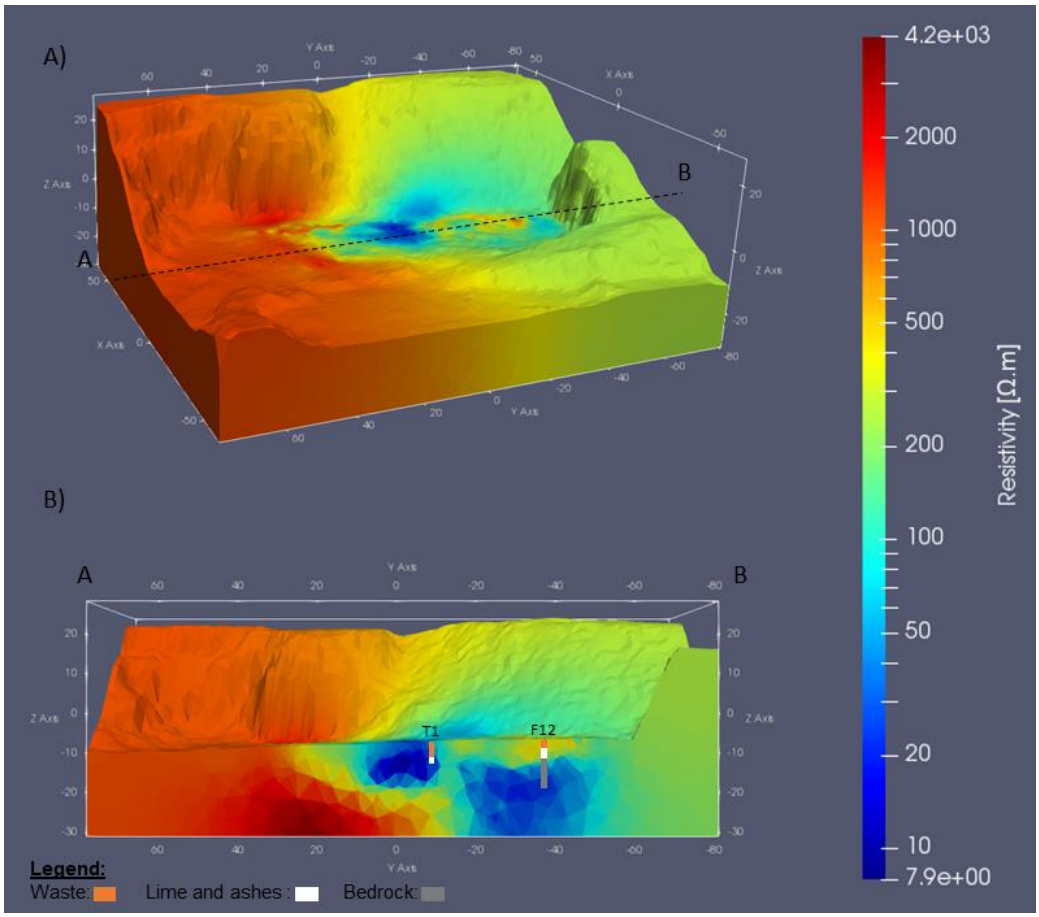

Figure 37. Resulting resistivity images of the inversion of the real dataset. **(A)** Global vision of the resistivity distribution **(B)** cross-section of the dashed line of **(A)**. Borehole F12 was made in 2012 and trench T1 in 2018

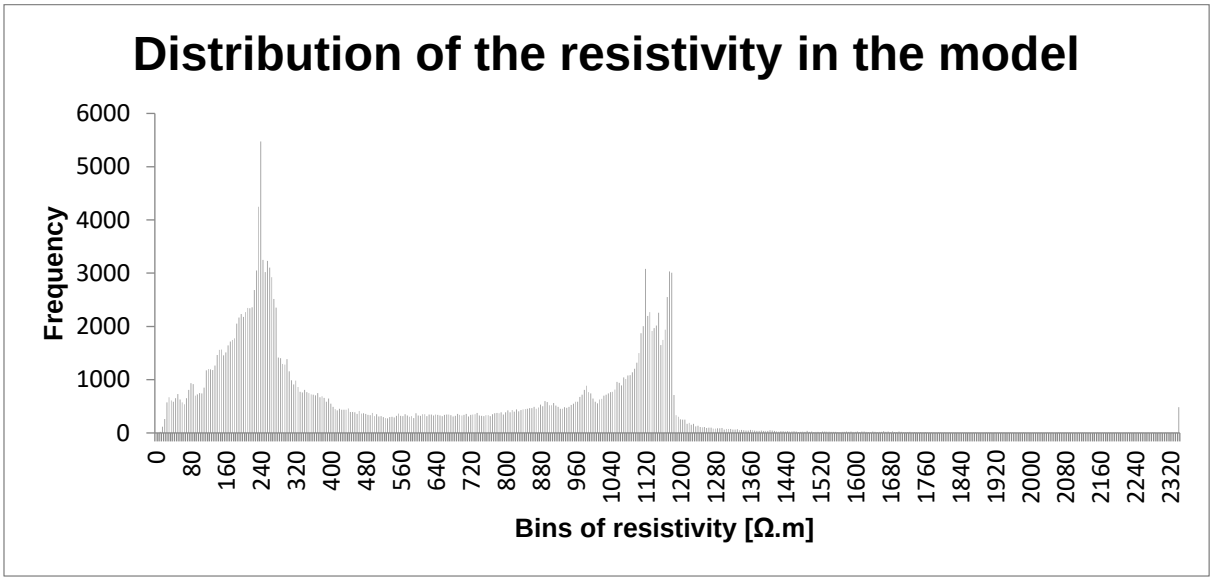

Figure 38. Histogram of the resistivities occurring in the model of Onoz

The cross-section (***Figure 37 B***), is also worth mentioning as it shows two zones of high conductivity. Given the previous investigations, especially the trenches and boreholes drilled during the previous invasive surveys (***Annex 9.1***), it is possible to link these zones to the presence of lime. These occurrences of lime are in fact fragments from the bigger heap forming the upper level in Onoz. Moreover, the base of the heap,

known to be composed of lime and ashes shows also very low resistivity values, supporting the assumption that the higher conductive zones can be related to lime. For a better comprehension of the occurrence of low resistivity values within the lime, the reader is invited to get acquainted with ***table 4*** in ***section 4.4***. Lime samples collected during site characterization revealed a contamination in hydrocarbons and other polluting elements. Furthermore, it has been demonstrated that hydrocarbons decrease the bulk electrical resistivity due to complex mechanisms notably related to bacterial activity. Considering that hydrocarbons are often electron donors, they are therefore bacterial activity incubator. As a consequence of this enhanced bacterial activity, organic and carbonic acids may be generated and subsequently accelerate the weathering of minerals, causing an increase of conductivity (Caterina et al., 2017). Besides the bacterial activity, the high conductivity can be explained by the nature of the ashes and lime. Indeed, both materials are unconsolidated and have potentially a higher surface area available. It can, therefore, potentially favour an increase of the interfacial conductivity (Abdel et al., 2004). Furthermore, the model shows that one of the highly conductive zones reaches the surface in the central part of the survey. Therefore, it is visually possible to verify the assumption that the most conductive parts are actually related to lime (***Figure 39***).

Figure 39. Photography of the surficial lime occurring in the central part of the survey in Onoz

The thickness of the greatest and highly conductive layer also seems to be relatively important given the expected geology. This distribution of the conductivity could be explained by the presence of leachate in the limestone. However, given the benchmark study performed in ***section 5.1.3***, the most probable explanation is an exaggeration of the actual thickness of lime and ashes during the inversion. Indeed, the purpose of ***section 5.1.3***, was principally to highlight that such an overestimated thickness, could develop in presence of a thick highly conductive layer. It is consequently impossible to determine the depth of the bedrock in this zone throughout the current survey.

In the northern part of the survey, the bedrock is, in contrast, detectable. Its depth is decreasing northward and became finally surficial, which corresponds quite accurately with the borehole/trench information.

Another zone worthy of interest is the one with a resistivity between 200-350 Ω.m occurring above the highly conductive zone. Considering the trenches and boreholes in that zone, it is postulated as backfill. The values are matching with the ones of backfill, even if they are affected by many parameters such as the compaction (Snapp et al., 2017). It is of course recognized that, in some zones, highly heterogeneous waste deposits are present. However, considering that it is mixed with backfill in certain places, and that it can have a resistivity around 100 Ω.m (Caterina et al., 2019), it is almost impossible to clearly differentiate it from the backfill. However, lower values occur at the surface and are probably related to the presence of this waste.

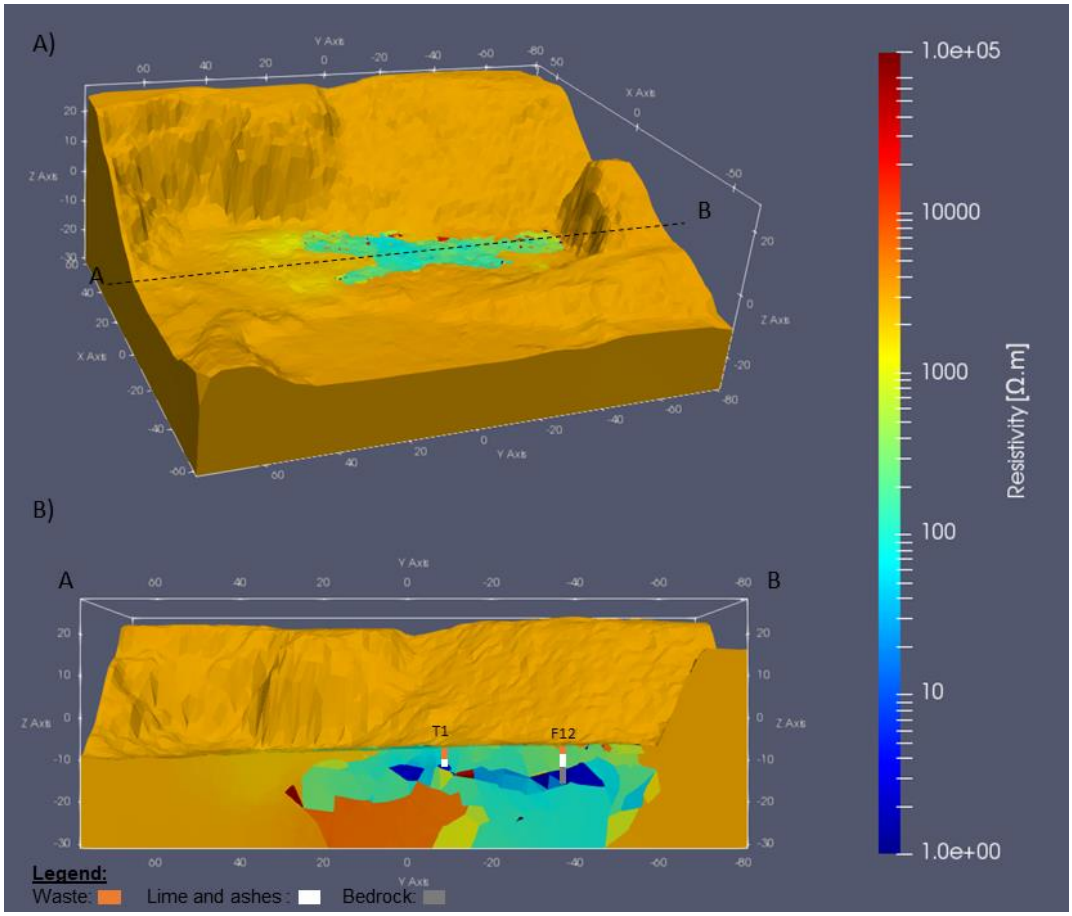

Figure 40. Resulting resistivity images of the "blocky" inversion of the real dataset. **(A)** Global vision of the resistivity distribution **(B)** cross-section of the dashed line of **(A)**. Borehole F12 was made in 2012 and trench T1 in 2018

A possible way to better define the limits between the different elements constituting the landfill in Onoz, is to perform a blocky inversion, even if the relatively voluminous size of the tetrahedrons building the mesh, renders the model rough. In addition to the different figures outlining the resulting model (***Figure 40***), the histogram of the resistivity (***Figure 41***) is plotted in order to enhance our interpretation. When both figures are considered, the first point that has to be discuss is the peak around 2 880 Ω.m, which covers most of the model. This is in fact the zones where the actual survey was missing information and that remain near the starting model that was previously fixed at 3 333 Ω.m. The distribution around the peak is much narrower than for the previous histogram, due to the fact that almost no smoothing was applied during the inversion.

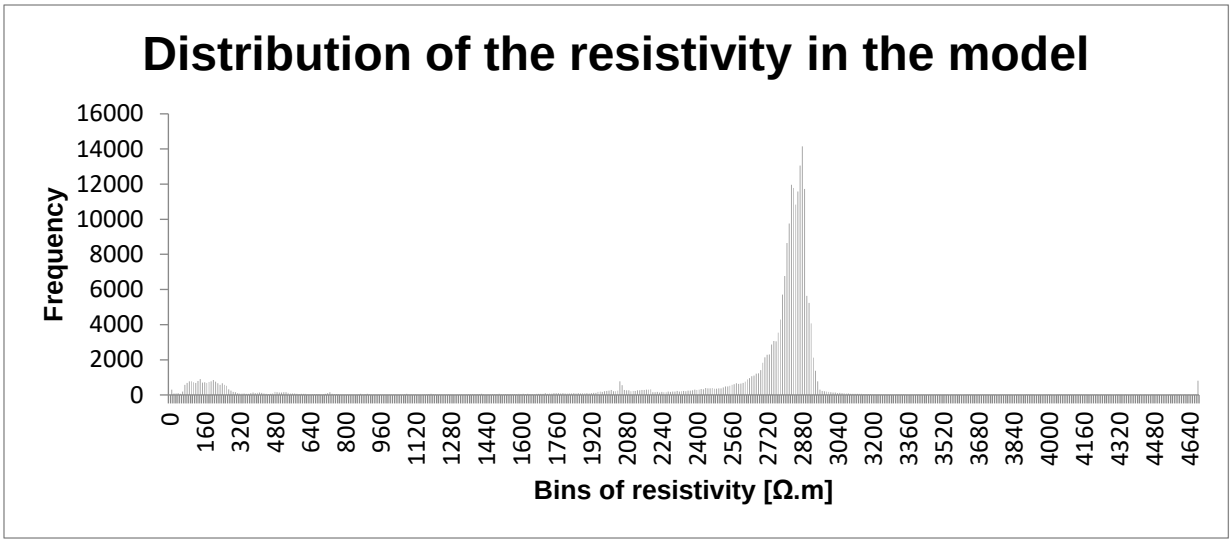

Figure 41.Histogram of the resistivities occurring in the blocky model of Onoz

The next category of resistivity that is pinpointed from the model and the histogram, is the one around 2 080 Ω.m. It is not a major part of the model, but remains visible. It specifically occurs in the northern part of the survey and probably is the proper resistivity value of the bedrock in Onoz, which is made up of limestone.

The next interval of values visible is ranging from 60 to 300 Ω.m. As already mentioned, this interval corresponds to the part of the landfill where waste and backfill deposits occur. In comparison to the smoothed inversion, the differentiation between the waste and the backfill remains difficult, although once again, the lower resistivity values occurring in this zone can be related to waste.

Another peak present at the end of the histogram, also indicates that much higher resistivities occur in the model. A major part of it is the part of the bedrock, where the resistivity is overestimated, as it was already explained. The very high values occurring in the model are inversion artefacts that have no natural existence.

The last interval of resistivity values visible in the histogram and the model, especially in the cross-section, is defined around 10 Ω.m. As already mentioned, this type of high conductivity can be related to lime, impacted by the presence of polluting elements, hydrocarbons in general. Indeed, as the study carried out by Caterina et al., (2017) tended to prove, the impact of the concentration of hydrocarbons on the resistivity seems consequent. Zones composed of asphalt and backfill are showing a resistivity around above 40 Ω.m, while other zones with the same composition but with a higher concentration are showing a lower resistivity around 10 Ω.m. This is, therefore, compliant with the resistivity obtained for the lime and ashes during this master thesis. The greatest conductive zone delimitation is more precise than for the smoothed inversion and the thickness seems closer to reality. However, the effect on the underlying ground is still significant, as it is expected from the synthetic model.

It is also interesting to define the limits of lime within the site and to compare the size for both inversions. For this purpose, a maximum threshold value of 40 Ω.m was applied on both resulting models (***Figures 42 and 43***).

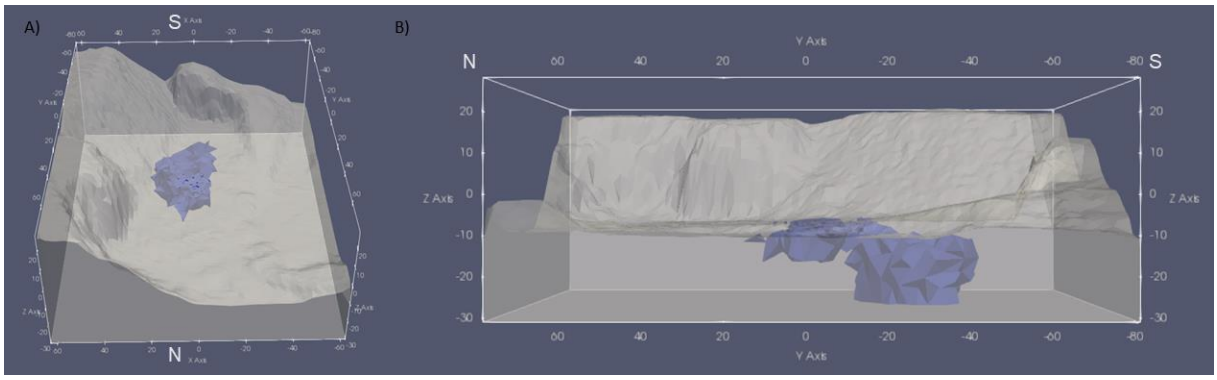

***Figure 42*.** Application of a maximum resistivity threshold of 40 Ω.m on the mode from the smoothed inversion (zone in blue), **(A)** shows the horizontal extension, **(B)** the vertical extension

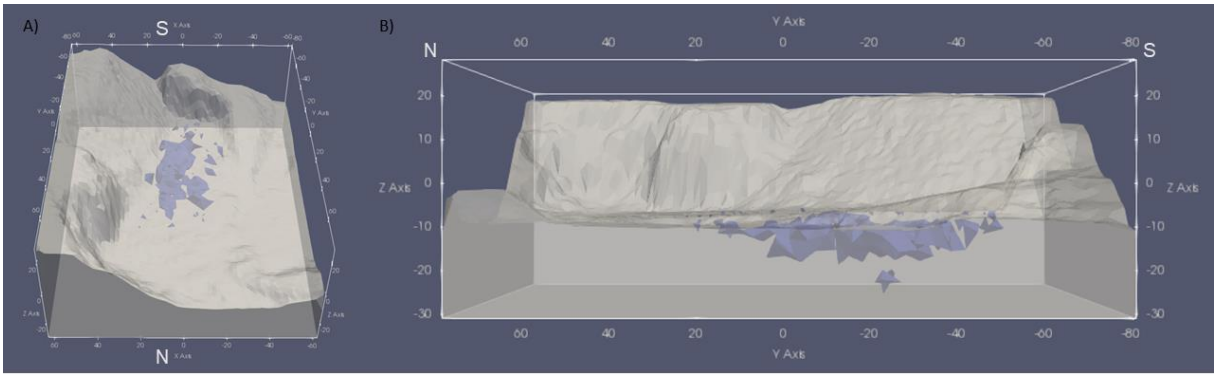

***Figure 43*.** Application of a maximum resistivity threshold of 40 Ω.m on the model from the blocky inversion (zone in blue), **(A)** shows the horizontal extension, **(B)** the vertical extension

What comes out of this comparison is a clear difference, especially in terms of vertical extension, between the volume defined by the 40 Ω.m threshold for both resulting models. In both cases, the highly conductive zone is located near the massif of lime and ashes, supporting the hypothesis that the conductive zone is mainly composed of these types of waste. The volume is generally more continuous for the smoothed inversion, enhancing the lateral extension of the body in the western direction, where the blocky inversion only displays small sparse zones of lime. Furthermore, the biggest drawback is the overestimated thickness of the layer in the southern part of the model, which has already been previously discussed. The comparison with the other model, which is known to be much closer to the reality, thanks to the boreholes, enables to realize how important the exaggeration is. To conclude on the resulting model, it is possible to summarize that the main drawback for the smoothness constrained inversion is an important exaggeration of the thickness of the conductive layer, while the one of the sharp inversion is the roughness rendering the resulting images relatively raw although closer to the reality.

Finally, an interesting point would be the comparison of the lateral extension of the ashes and lime lens given by two different methods. Indeed, it seems appropriate to compare the lateral extension given by the ERT to the one given by the previous FDEM survey. For this purpose, it was decided to compare both methods at depths that were previously investigated with the FDEM, i.e. 0.5 (***Figure 44***) and 2.5 m (***Figure 45***). Following Caterina et al., (2019), the ashes and lime were represented by an electrical conductivity larger than 40 mS/m during the FDEM survey. For a proper comparison, the resistivity was converted into conductivity and the conductivities interval was rescaled to match the one used for the FDEM, i.e. from 0 to 40 mS/m.

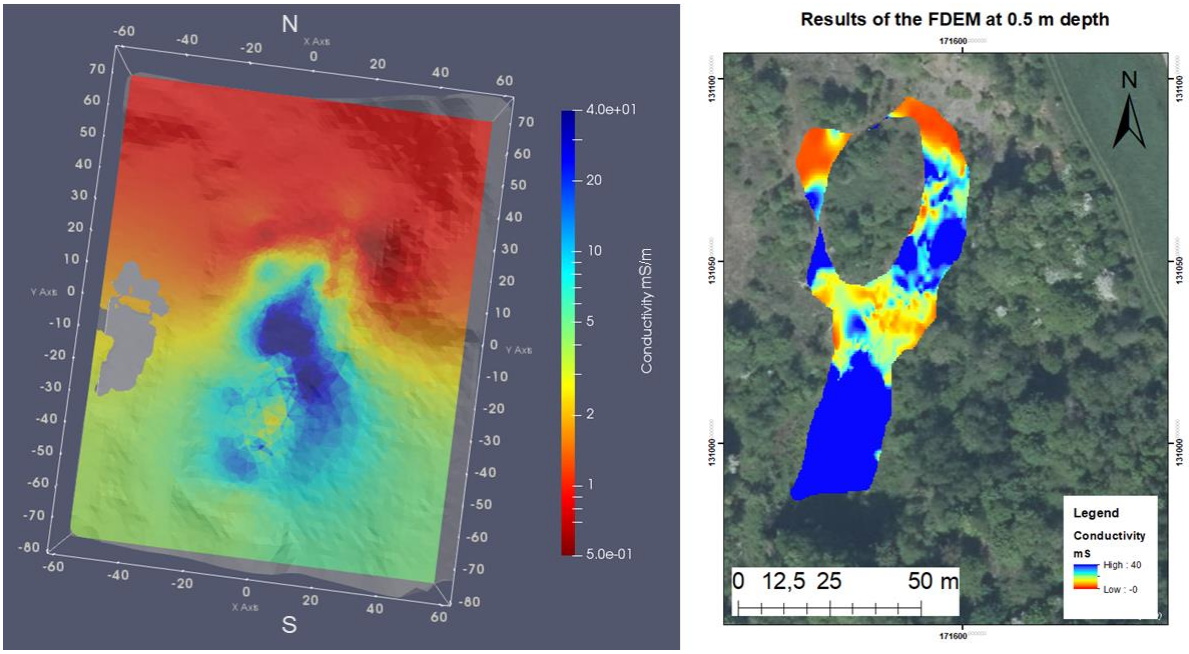

Figure 44. Comparison of the lateral extension given by the ERT and the FDEM surveys at a depth of 0.5 m (Adapted from Caterina et al., 2019).

The first thing to be pinpointed is that the ashes and lime body is detected in the same zone, with both methods, at both depths. For the 0.5 m depth, the ashes and lime lens seem to be slightly overestimated in the northern direction. However, it matches quite well in the case of the 2.5 m depth. At both depth, for the ERT results, the conductivity seems to decrease in the south-east part of the surveyed zone, where the FDEM still displayed high conductivity values. This difference may be explained by several factors such as a loss of sensitivity in this zone due to the special ERT configuration. It could also be attributed to the smoothing applied during the inversion. Unfortunately, the roughness of the model obtained from the blocky inversion, due to the great size of the tetrahedrons composing the mesh, renders the comparison challenging.

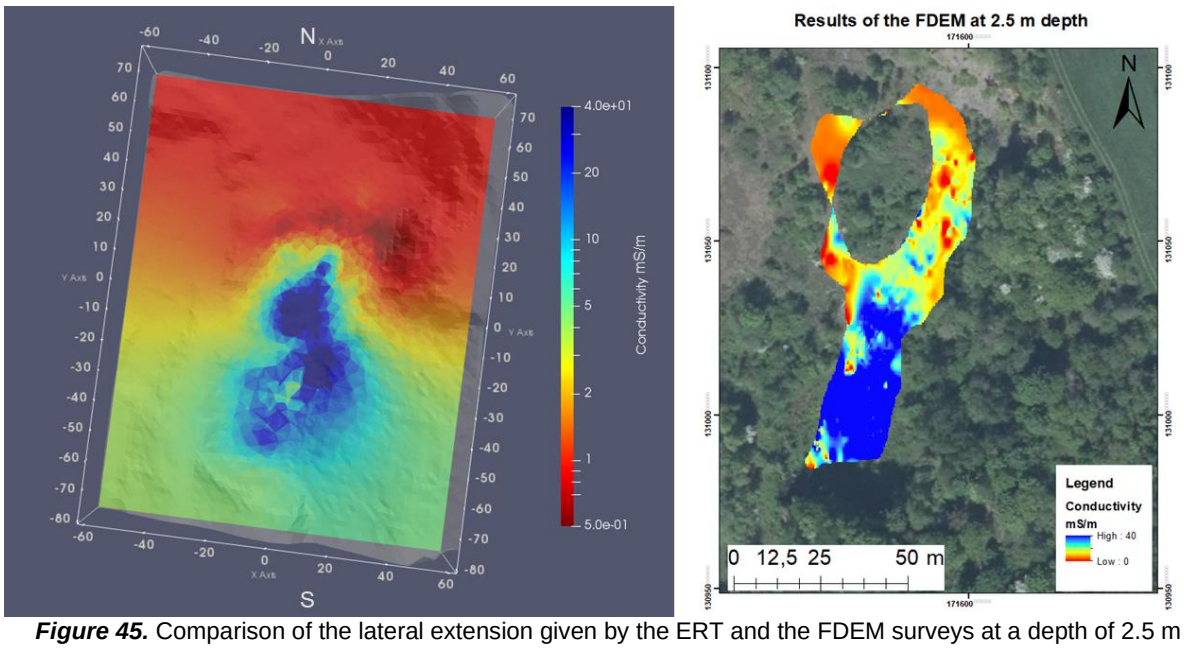

Figure 45. Comparison of the lateral extension given by the ERT and the FDEM surveys at a depth of 2.5 m (Adapted from Caterina et al., 2019).

A final explanation can be provided by the FDEM survey. Indeed, if a closer look is taken at the coverage of the FDEM (***Figure 46***), it is visible that this part of the site was inaccessible. The conductivity of the zone is therefore only known by interpolation of the surrounding results. Consequently, if the presence of lime and ashes was reduced in this part, the change would not have been detectable by the FDEM, but well by the ERT thanks to the crossline measurements implemented in the protocol.

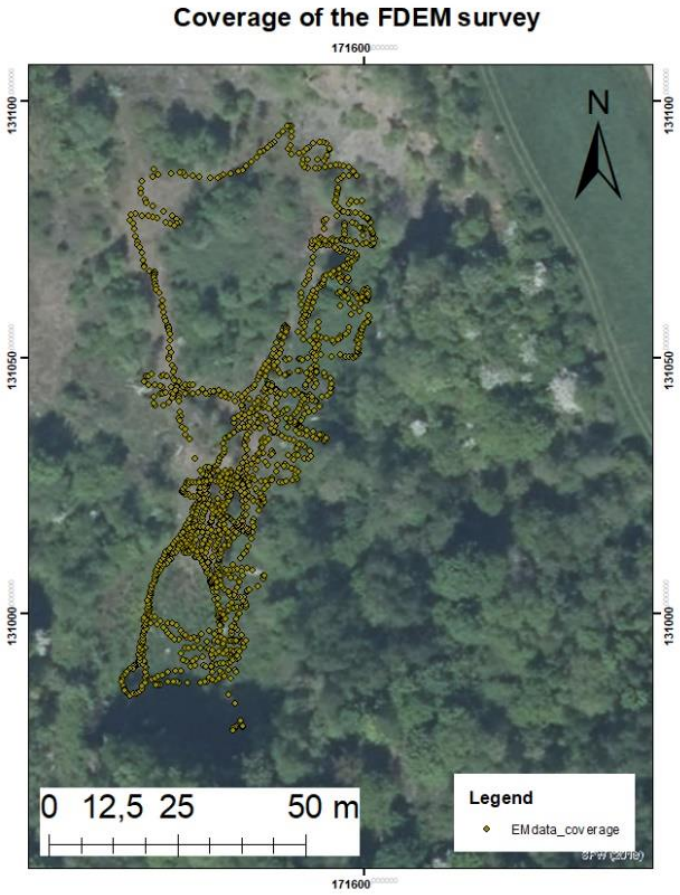

Figure 46. Coverage of the FDEM survey (Adapted from Service Public de Wallonie, 2018)

6.1.1.2 3D IP

As E4D requires a commercial license to perform the inversion of IP data, data collected in Onoz were inverted with BERT (***Figure 47***).

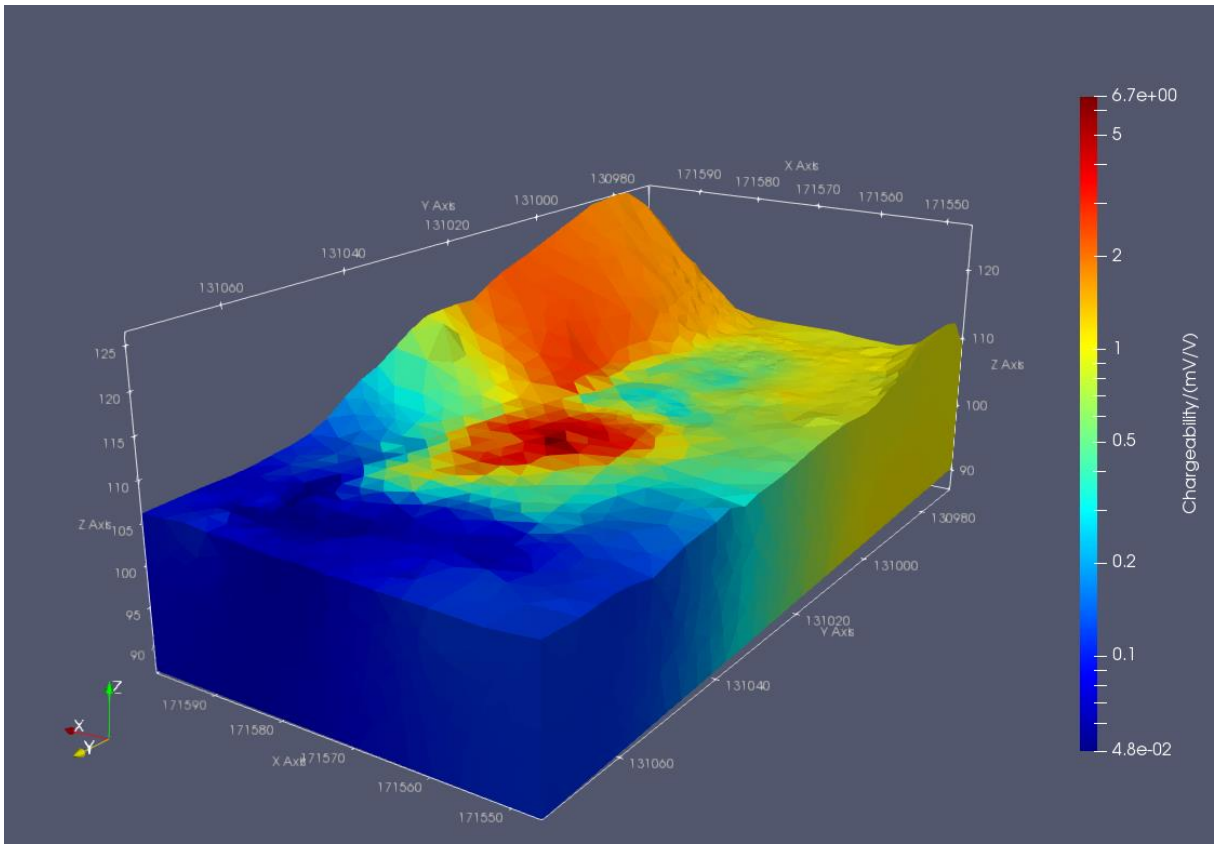

Figure 47. 3D IP model performed using BERT

The ashes and lime layer seemed to be defined by the higher chargeability occurring in the landfill. This is clearly identifiable, knowing the composition of the massif in the south-east corner of the model. The rest of the waste is characterized by a low chargeability, especially inert, or by intermediate values. The bedrock seems to have a low chargeability in certain places and intermediate in other places. This could be explained by natural factors such as the fracturation or the porosity. Algorithmic explanations are also possible, considering that the high chargeabilities measured for the lime and ashes are impacting the rest of the model such as for the ERT. The different assumptions on this model, will be further investigated during the analysis of the 2D profiles.

6.1.1.3 3D DOI

As for the synthetic model, the next step is to assess the zones where the actual survey is sensitive. As already mentioned, the selected image appraised tool was the DOI. Unfortunately, the highly conductive zones also have an impact on the quality of the information given by the DOI. It is interesting to display the resistivity distribution model, regarding a very high resistivity reference model, to further observe the evolution of the resistivity below the highly conductive layer. The inversion performed, was a blocky one, since it already demonstrated to be the most suitable in terms of layer delineation and the reference model was fixed at 5 000 Ω.m (***Figure 48***).

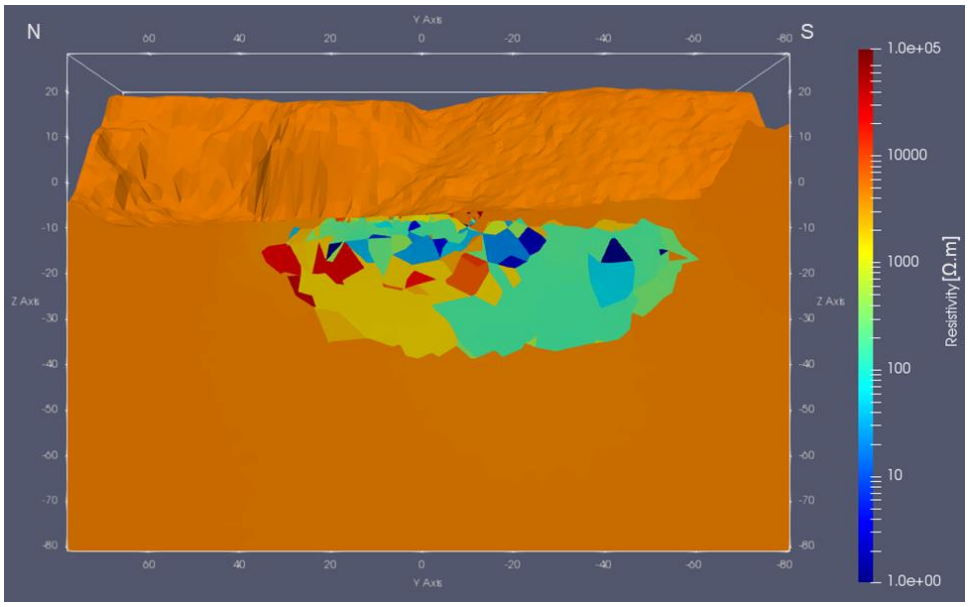

Figure 48. Resistivity model from an blocky inversion enforced by a reference model of 5 000 Ω.m

It is clear that the zone, below the highly conductive layer still tends to a higher conductivity than expected and therefore, the quality of the DOI is going to be affected in this specific zone. The same effect is also observed in the part below the ashes and lime hill, where high conductivity values could be detected during the survey.

The reference models used for the computation of DOI were fixed at 25 and 5 000 Ω.m. Firstly, the localisation of the parameters with a DOI below 0.1, obtained from the smoothed constrained inversion is displayed (***Figure 49***). It is evident that the DOI is clearly overestimated. The DOI indicates zones as sensitive, where it has already been demonstrated that the results are distorted by the conductive layer. This is even more visible in the part below the ashes and lime massif, where the DOI indicates a sensitive zone below 50 m, which is obviously impossible considering the length of the different profiles of the survey. The approximate 15 m of depth in the zone, where the bedrock occurred, are also considered as slightly overestimated.

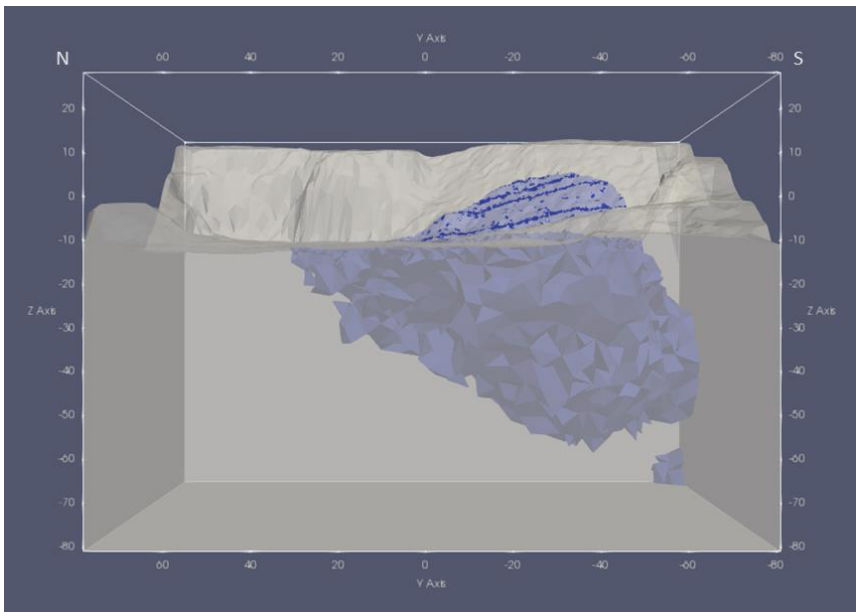

Figure 49. DOI from the smoothness constrained inversion

Secondly, the DOI from the blocky constrained inversion was computed (***Figure 50***). The size of the volume having parameters with a DOI below 0.1, still seems to be affected by an exaggeration due to the presence of the conductive layer. However, compared to the smoothed model, the exaggeration is mitigated around 35 m, below the conductive layer and within the massif. Unfortunately, the problem subsists, and the probable real sensitivity is never reached, depending on the impact of the conductive layer on the overall model. Furthermore, in the part where the bedrock is visible, the volume considered as sensitive is clearly diminished to reach approximatively 5 m of depth, which approximately fits the reality, even if some sparse elements of the mesh were falsely considered as sensitive. This supports the assumption previously done, demonstrating that the resistivity value of the bedrock was overestimated by the algorithm, because the survey was not sensitive in this zone.

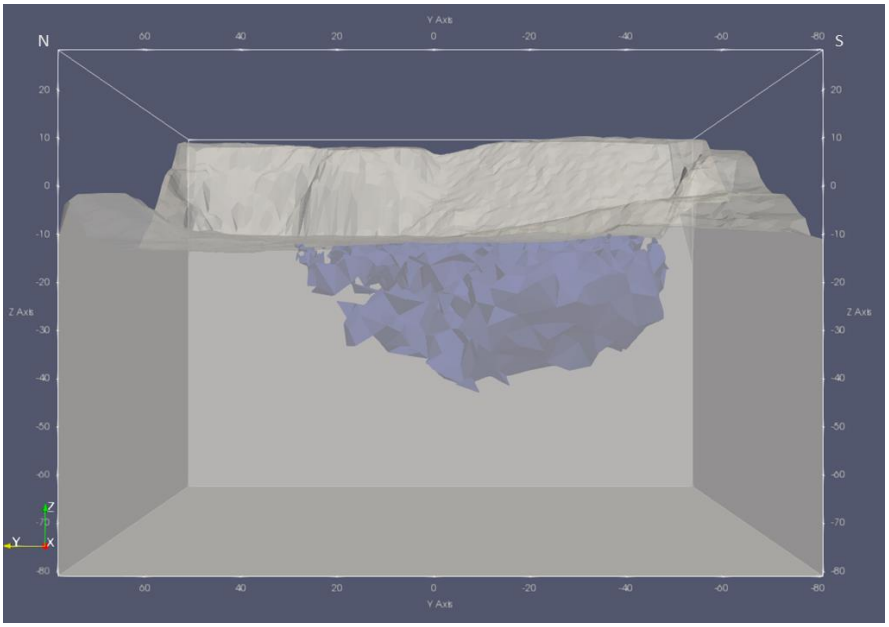

Figure 50. DOI from the blocky constrained inversion

To conclude this section, we should bear in mind that the 3D ERT/IP survey had for purpose to give an idea of the material distribution in the quarry of Onoz. The presence of the highly conductive layer of lime distorted the resulting model, rendering difficult to define the precise interface between the waste, lime, backfill and the bedrock in the lower zone. However, it was possible to delineate approximatively each type of material in the upper part of the subsurface. The sharp inversion showed rougher resulting images but remained closer to the reality of the field. The main problem that could be highlighted in this section is the fact that the DOI was affected by the presence of the highly conductive layer, enforcing partially the model to converge to lower resistivity values even in case of a highly resistive reference model.

6.1.2 2D interpretation

6.1.2.1 2D ERT

The 2D interpretation, although not being the main concern of this survey, is still interesting in order to display the results of the in-line measurements of the four profiles and to compare them to the 3D results. For a rapid reminder of the location of each profile, the readers are invited to look again at ***figure 20***.

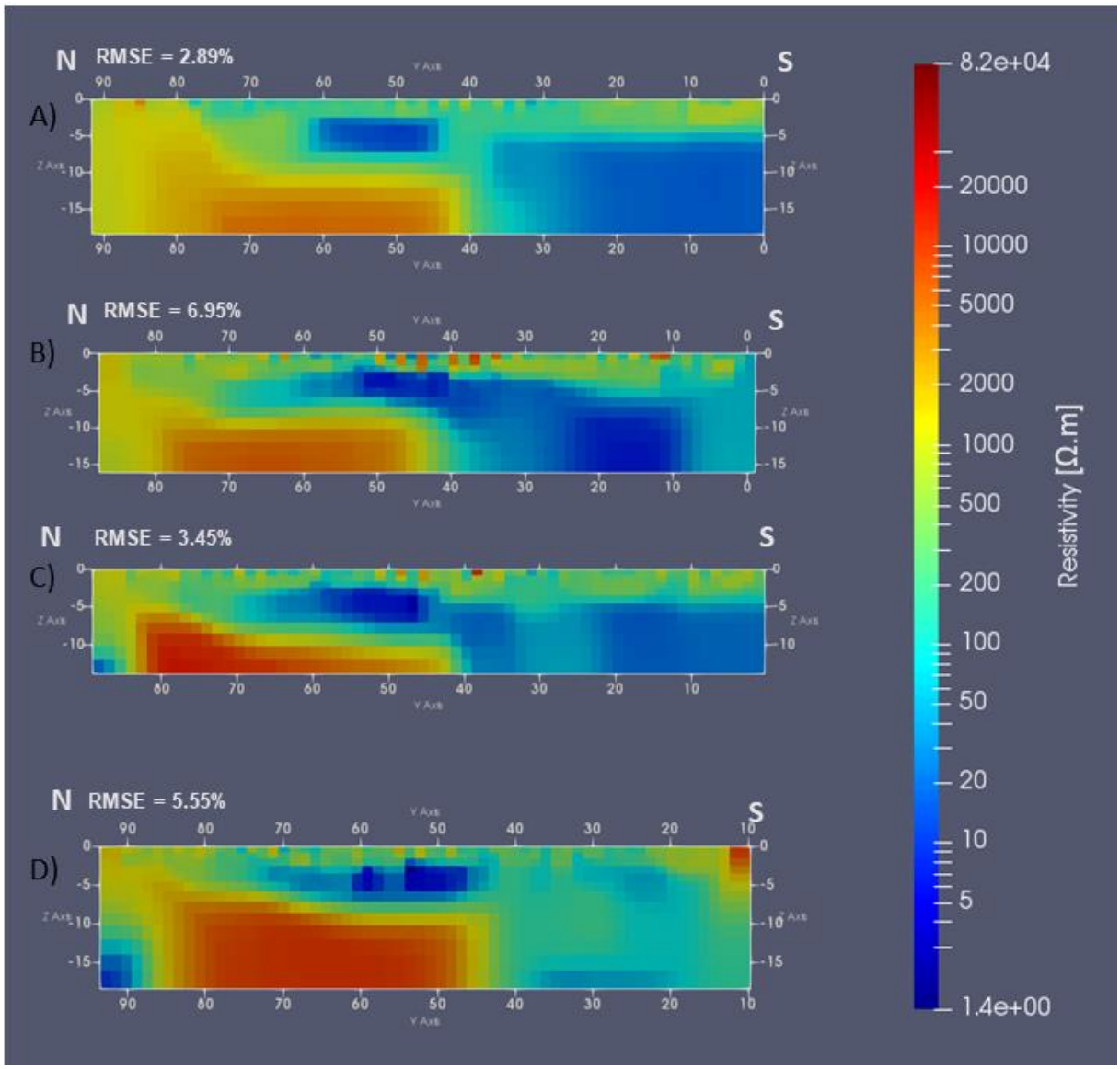

Figure 51. Resistivity models obtained after inversion of in-line measurement for **(A)** P1 **(B)** P2 (C) P3 (D) P4

Figure 51 displays the resulting resistivity model for each profile and they all seem consistent with the results of the 3D inversion. Furthermore, the RMSE of each profile, is smaller than the reasonable threshold value previously fixed at 10 %. For each profile, the bedrock occurs in the northern part, with an overestimated resistivity around 5 000 Ω.m. Furthermore, a lens of highly conductive material is present and can be once again related to lime charged in hydrocarbons and other pollutants (Caterina et al., 2017). In the southern part, the conductive layer, already seen in the 3D inversion, occurs again and its thickness is also overestimated, considering that it

is impossible to detect the bedrock, which is known to sit there thanks to the previous boreholes and trenches. The effect of this conductive layer seems to decrease, when the profile is moved away from the ashes and lime massif. However, it remains impossible to detect the bedrock in this zone. Near the soil surface, the resistivity values are more heterogeneous, which remains consistent with the presence of backfill and heterogeneous waste.

Figure 52 shows the same profiles as those presented in ***figure 51***, with the difference that they are cross-sections taken from the 3D model previously displayed. This enables an appropriate comparison between the results of the 3D and 2D inversions. The results seem relatively comparable. Profile P1 shows a separation between the two highly conductive lenses, while P2 shows that it is one main highly conductive body. Moreover, P3 and P4 displays the same kind of internal structures. Both also overestimate the conductive bodies. The difference between the resistivities interval is caused by the smoothing applied during the 3D inversion, inhibiting the creation of small artefacts as those occurring in the 2D profiles.

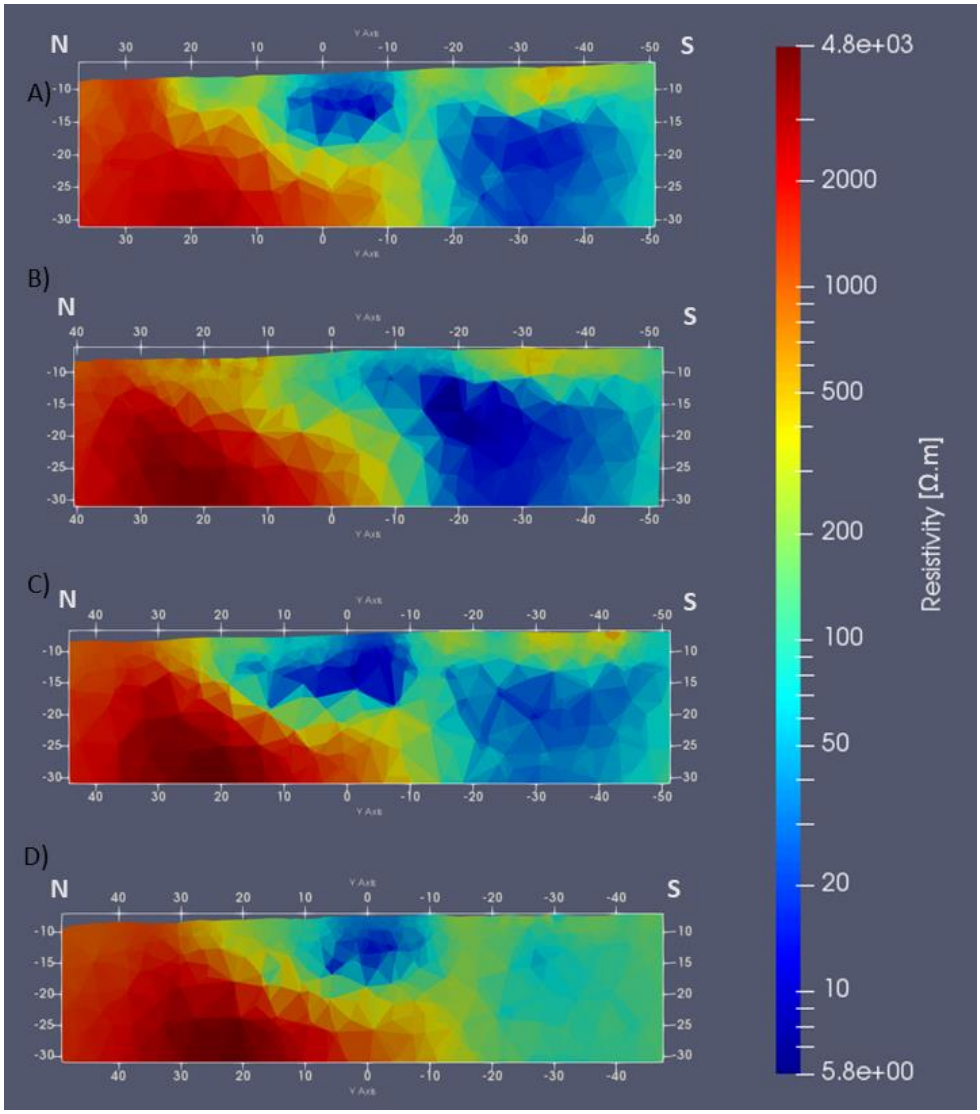

Figure 52. Resistivity profiles obtained from cross-sections of the 3D model corresponding to the 2D profiles for **(A)** P1 **(B)** P2 (C) P3 (D) P4

6.1.2.2 2D IP

Figure 53 displays the resulting images of the IP. measurements. The results enable a differentiation between the different materials found in Onoz. Indeed, knowing approximately the disposition of the material in the site, it is possible to link the faced chargeability to the right soil component. The bedrock, in the deepest part of the profiles, is defined by a low or intermediate chargeability. The interval of chargeability for the bedrock is due to many parameters, such as the fracturation or the porosity for example. The lime, ashes and waste with high metallic content, backfill and waste and inert waste are showing respectively high, intermediate and low chargeability values in the surficial part of the profiles. The higher chargeabilities displayed deeper are linked to the lime and ashes layer. Indeed, considering that it occurs in the southern part of the profiles and especially in profiles 1, 2 and 3 (***Figure 53 A, B, C***), i.e. those closer to the ashes and lime hill, the link can be clearly established. However, it is also clear, that the thickness of the layer is overestimated, as for the ERT.

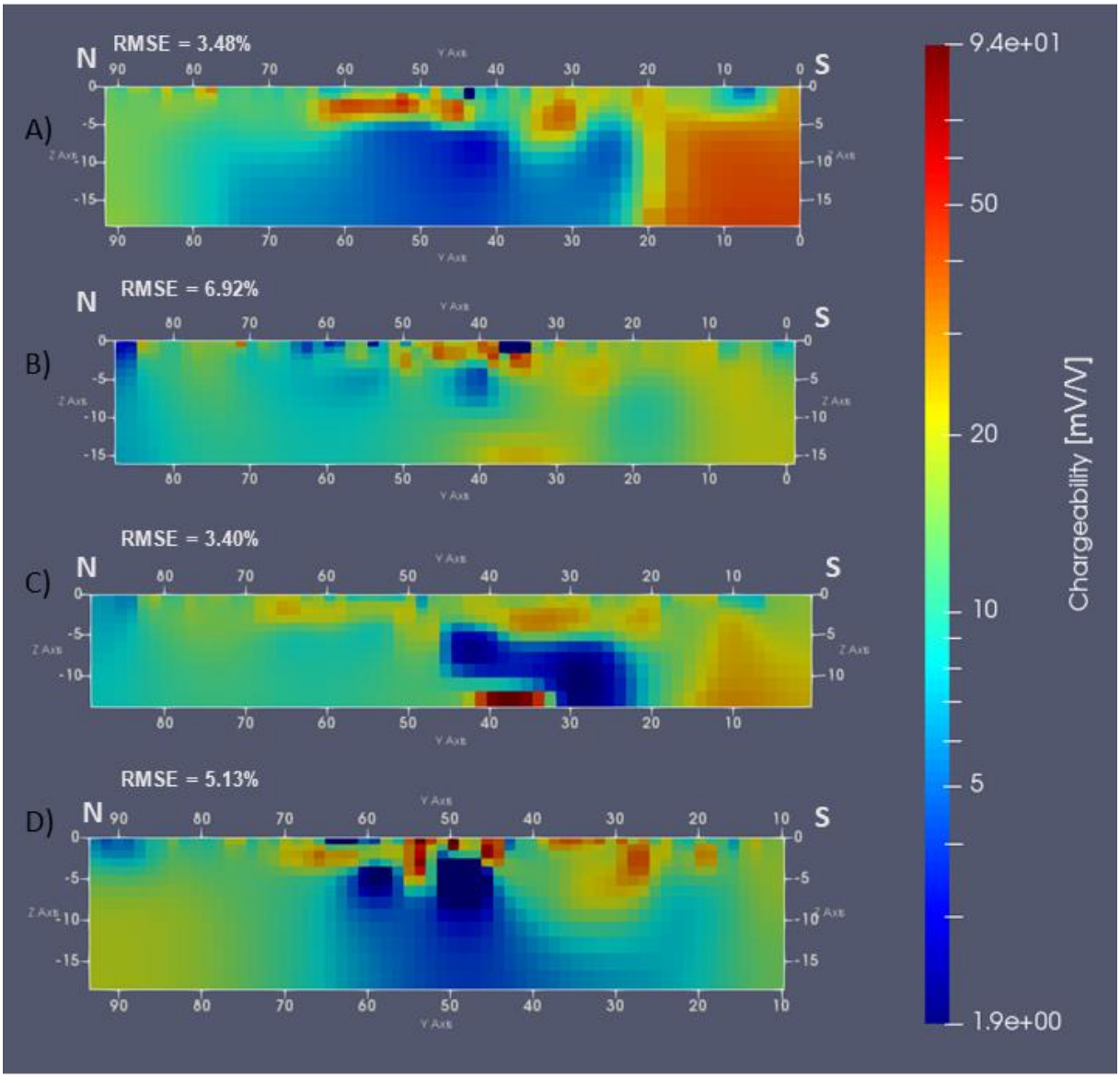

Figure 53. Chargeability models obtained after inversion of in-line measurement for **(A)** P1 **(B)** P2 (C) P3 (D) P4

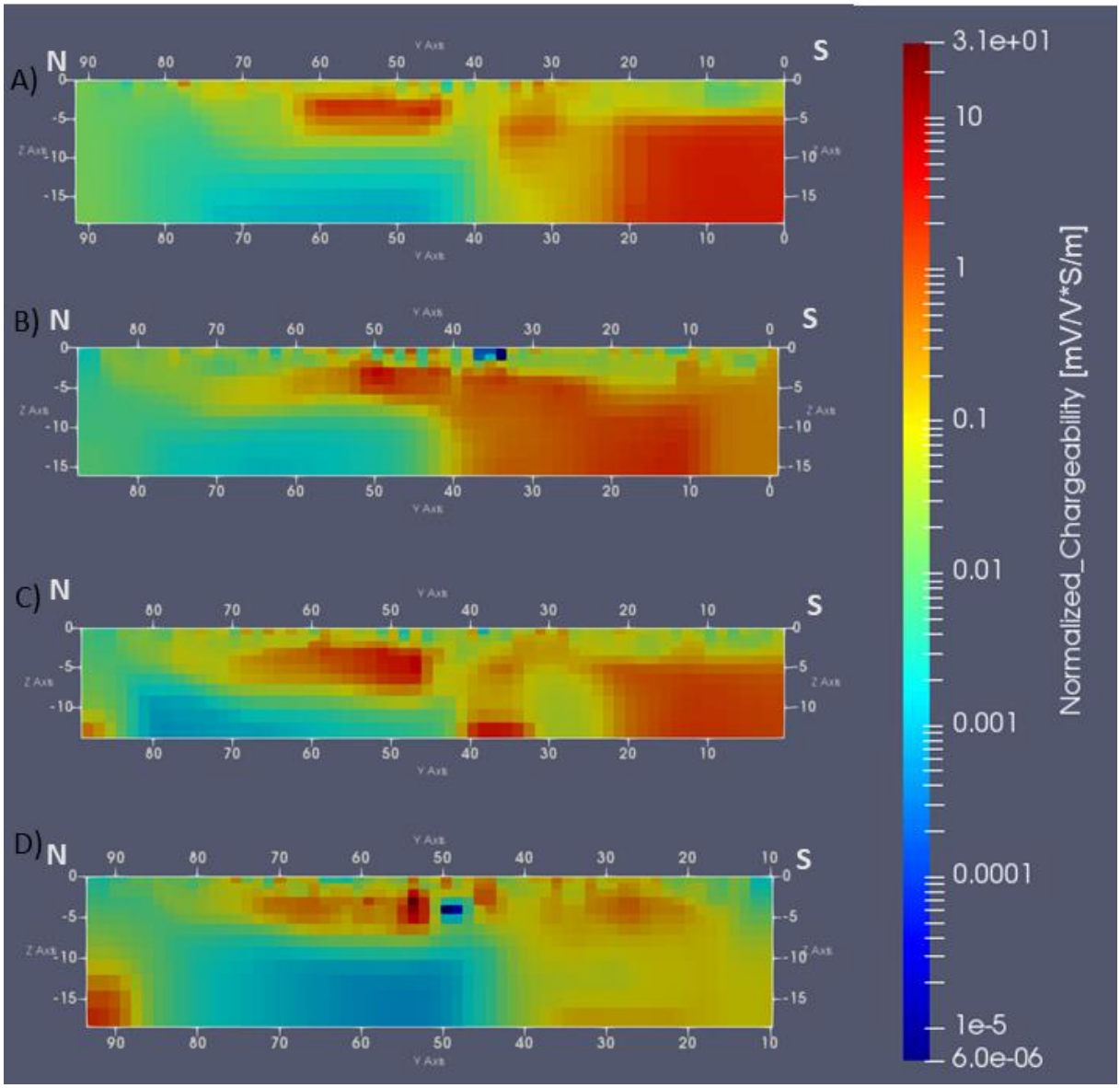

Figure 54. Normalized Chargeability models obtained after inversion of in-line measurement for **(A)** P1 **(B)** P2 (C) P3 (D) P4

As already mentioned (***Chapter 3***), a good way to further distinguish the different materials in the subsurface is to compute the normalized chargeability (Dahlin et al., 2010; Ellis et al., 2016). ***Figure 54*** shows the obtained profiles. The central lens of lime and ashes is yet well defined in the central part of each profiles. Profiles 2 and 4 (***Figure 54 B, C***) show distinct lenses of inert. The rest remains quite similar, even if unfortunately, the body of ashes and lime in the eastern part is still highly overestimated.

6.1.2.3 2D DOI

As for the 3D model, it is important to display the DOI of the 2D profiles (***Figure 55***). In some regions the DOI reached 20 m deep, which is considered as flaw considering the array and the length of the survey. The biggest difference with the 3D DOI is the fact that in the southern part of 5-m to 10-m depth of profiles 1,2 and 3 (***Figure 55 A, B, C***), a less sensitive zone appears. This is the first time, that the thickness of the high conductivity layer occurring in this zone is queried. Another zone

showing a lack of sensitivity is situated in the central part of each profile, where the resistivity measurements showed an interface between a low resistivity and high resistivity zone. A loss of sensitivity in the northern part, i.e. where the bedrock occurs, is also visible and is consistent with the apparition of a higher resistivity layer, allowing less current to pass by.

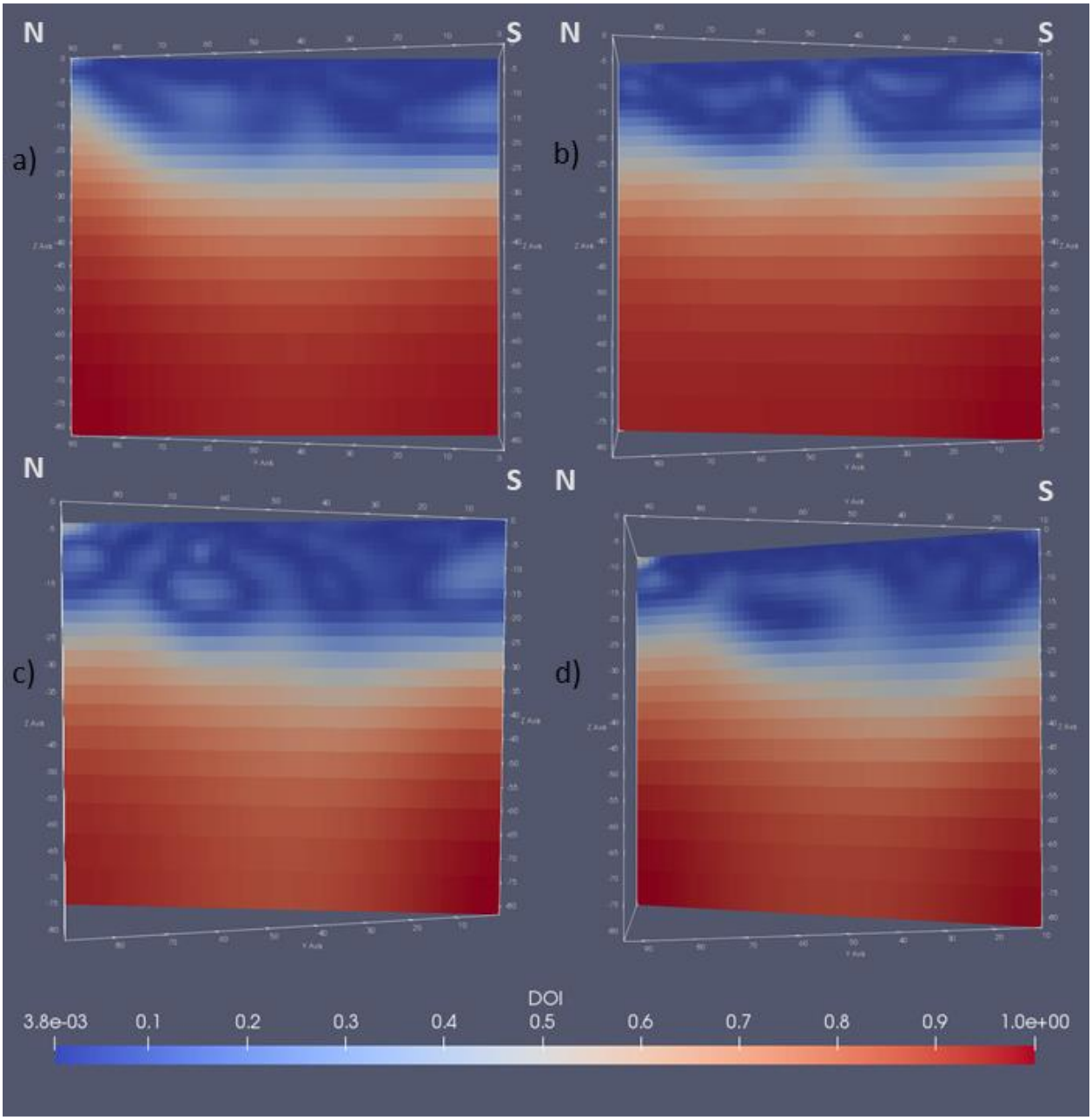

Figure 55. DOI of profile **(A)** 1 **(B)** 2 (C) 3 (D) 4

To conclude, the DOIs of the 2D profiles remains incorrect, but tends in the right direction by showing a lack of sensitivity in zones, where it is known that the high conductivity layer is overestimated. However, it is too deep compared to the expectations.

6.2 HVNSR

6.2.1 Lower part

As already mentioned (***section 5.2***), the heterogeneity of the subsurface in this part of the site rendered the achievement of HVNSR measurements interpretation more challenging than in “classic” alluvial sediments. Moreover, the lack of information, especially on the seismic velocity of the different materials composing the soil and considering that calibrating the HVNSR graphs obtained was challenging, made impossible the approximation of the depth of the different layers. The main purpose of performing HVNSR measurements, in this part, was to demonstrate its value in specific environments such as landfill and to show that it could be helpful in the delineation of different zones, in terms of waste distribution.

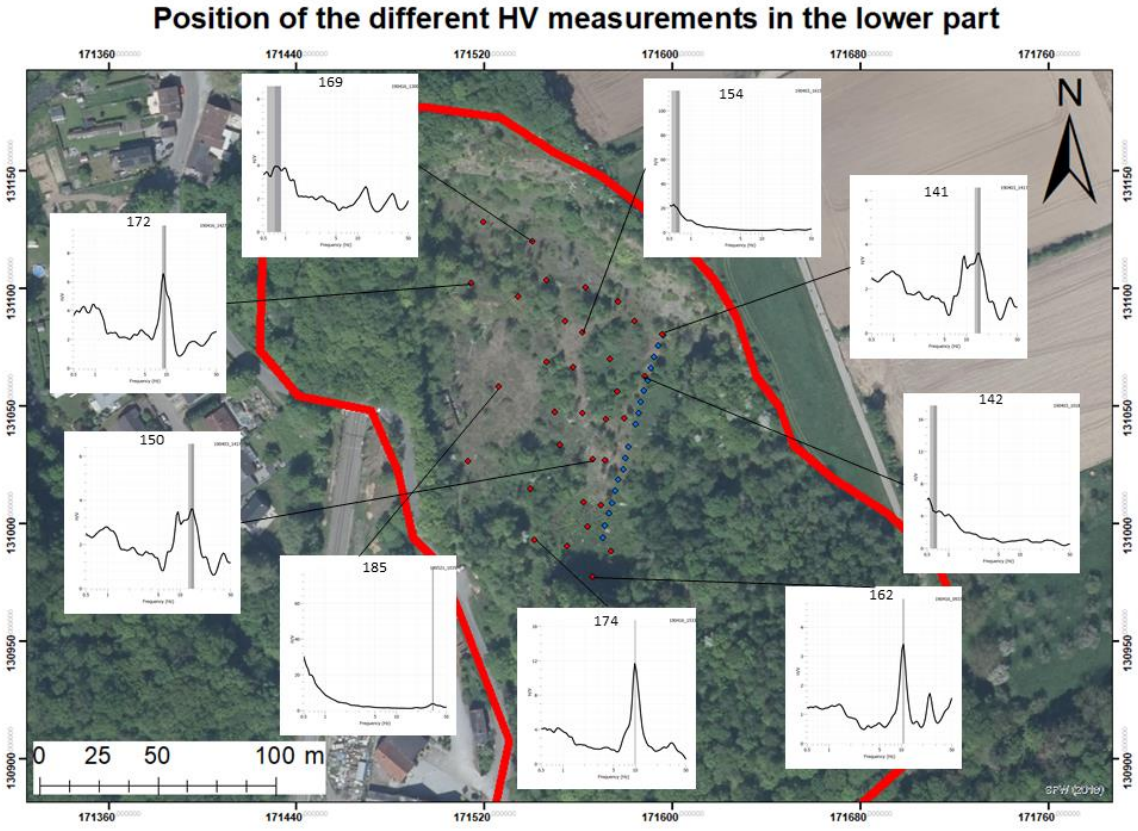

Figure 56. HVNSR measurements map of the lower part and representative graphs of the different zones (Adapted from Service Public de Wallonie, 2018)

Figure 56 displays the map of the HVNSR measurements in the lower part and the representative graphs arising from these measurements in specific areas of the landfill. It is interesting to analyse some of those HVNSR graphs and to relate them to previous information gathered from the invasive investigations. All the HVNSR graphs are presented in ***annex 9.5***. The first one analysed is the measurements n°185, which was taken at the lowest point of the quarry and seems relatively flat. However, a small peak occurs around a frequency of 33 Hz. This frequency is plausible given the frequency band of the instrument, i.e. 200 Hz. Indeed, following Nyquist (1928) the maximal sampling frequency can be of 100 Hz. This graph is compared with the trench number 10 made in 2012 by RECOsol SPRL (***Figure 57***). It should be noticed that the

mean H/V curve is the black line, while the coloured lines represent all the H/V curves of the stability windows and the dotted lines, the standard deviation. The small peak frequency is in fact significant and could be related to the 50 cm of silt present directly above the bedrock. At this point, it is necessary to outline that the high amplitude at very low frequency, i.e. below and around 1 Hz, are probably caused by perturbations coming from weather conditions, which are not always optimal.

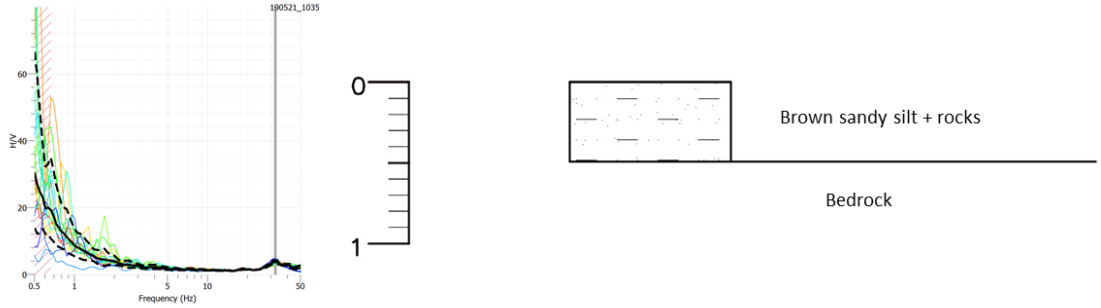

Figure 57. Comparison of the HVNSR curve of measurement 185 and the closest trench (Modified from RECOsol, 2012)

The next points analysed are the measurements n°172 and n°174. They are both situated at elevated points of the quarry. They were chosen to have approximately the same elevation. In the aerial photography of 1976 (***Figure 15***), it was clear that some structures were developed in these locations but probably not related to the discharge of lime and ashes. Some invasive investigations are still missing in this part of the site, nevertheless, the main scenario is that the structures are embankments made of tailings of the quarry exploitation, explaining the highest peak occurring between 9 and 10 Hz. However, the fact that the amplitudes of the peak are different could be explained in several ways. For example, the embankments could have been made of different materials or differently compacted, or the limestone composing the bedrock was more fractured or of slightly different compositions at each location. The upper layer was then recovered with soil, explaining the smaller second peak occurring at higher frequency in the graphs (***Figure 58***) and the dense vegetation in these parts of the site. The graph of the measurement n°171 (***Annex 9.5***), shows that the material in this structure dos not vary and the higher frequency of the peak corresponds to the diminution of the layer overlaying the bedrock.

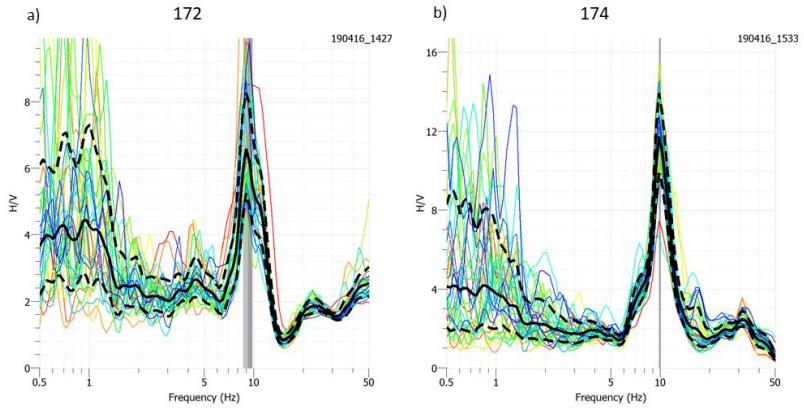

Figure 58. HVNSR curve for measurements 172 and 174

The next representative measurement analysed is n°162, located in the southern part of the landfill, close to the cliff and the hill of lime and ashes. The closest boreholes in this case is the n°2 achieved by IRCO SPRL in 2018, which is situated around 6 m far from the measurement point, but remains a proper representation of the subsurface. The visualisation of the H/V curve and the corresponding boreholes is displayed in ***figure 59***.

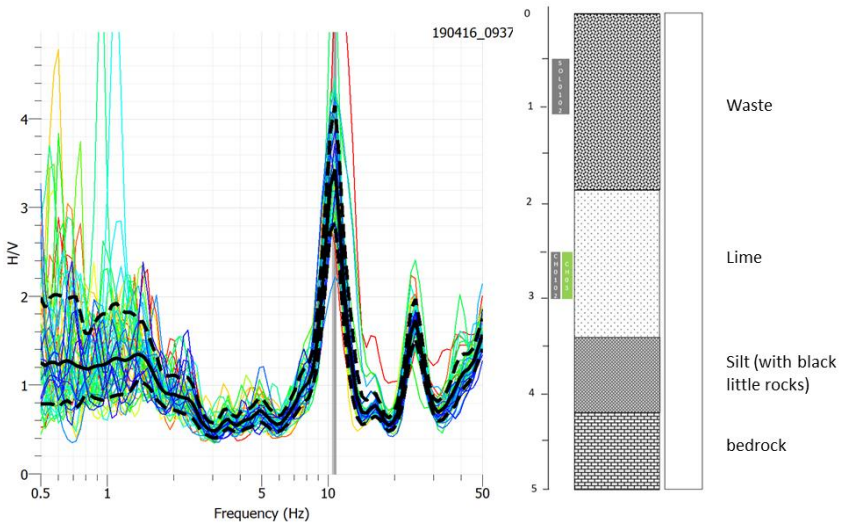

Figure 59. Comparison of the HVNSR curve of measurement 162 and the closest boreholes (Modified from IRCO, 2018)

The highest amplitude peak at a frequency around 11 Hz, can be clearly linked to the lime. Considering that the measurement point is closer to the hill of ashes and lime, it makes sense to estimate that the thickness of the lime layer is greater than the one displayed in the borehole 2. The second peak, with an amplitude of 2 at a frequency around 25 Hz is linked to the presence of the overlaying layer of waste. The silty layer, which has probably largely decrease in this zone, is probably too small and the contrast to the bedrock insignificant, to be clearly identified in the H/V curve at this point.

The same scheme is visible in the HVNSR curve of measurement n°152 (***Annex 9.5***), which was performed in a zone where it was already well known that a smaller layer of heterogeneous waste was overlaying a layer of lime and ashes.

The next zone analysed is much more complex. The representative measurement is the n°150. The peaks appearing in the H/V curve are less recognizable (***Figure 60***), which complicates the interpretation. After giving further interest at the closest trench (n°19 performed in 2012 by RECOsol), it is observable that the bedrock is overlaid by three different other layers, i.e. backfill, bricks foundation and lime. Multiple peaks with a certain amplitude appear in the HVNSR curve, showing that the instrument could sense the contrast between each layer. However, due to the lack of information on the seismic velocity of the different materials, it is unrealistic to link correctly each peak to its proper material. Measurements n°149 and 164 (***Annex 9.5***), also show the complex curve in the H/V graph and the trench nearby (n°4 by IRCO) and is also demonstrated to be composed of many different layers.

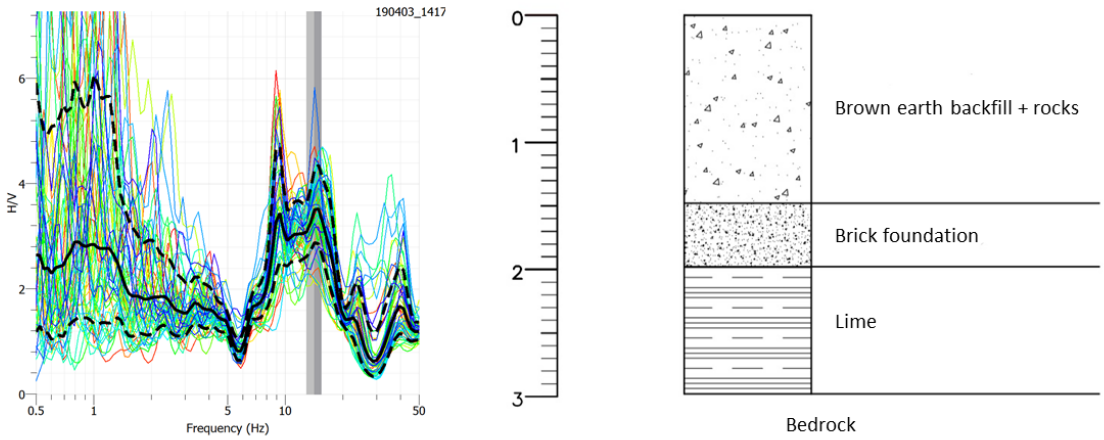

Figure 60. Comparison of the HVNSR graph of measurement 150 and the closest trench (Modified from RECOsol, 2012)

Of course, as for each geophysical method, the HVNSR is not an absolute method and can display some inconsistent results. Measurement n°142 (***Figure 61***) remains problematic. The H/V curve looked flat, implying that the bedrock was outcropping at this location. However, the trenches situated 3 m south-west far from it, shows that a significant layer of backfill, mixed with rocks and waste, is present and should be detected. It could be argued, that the very small peaks around 12 or 25 Hz could be the representative frequency of this layer. However, their amplitude is too small to be interpreted, since the seismic velocity contrast between the surficial layer and the bedrock should be bigger, given the nature of the component of each layer. It could also be possible, considering the heterogeneity of the soil in the landfill, that the surficial layer disappears. Nevertheless, the trenches n°3 made by IRCO in 2018 and situated further north in the nearby of n°142, shows that this backfill layer is still present.

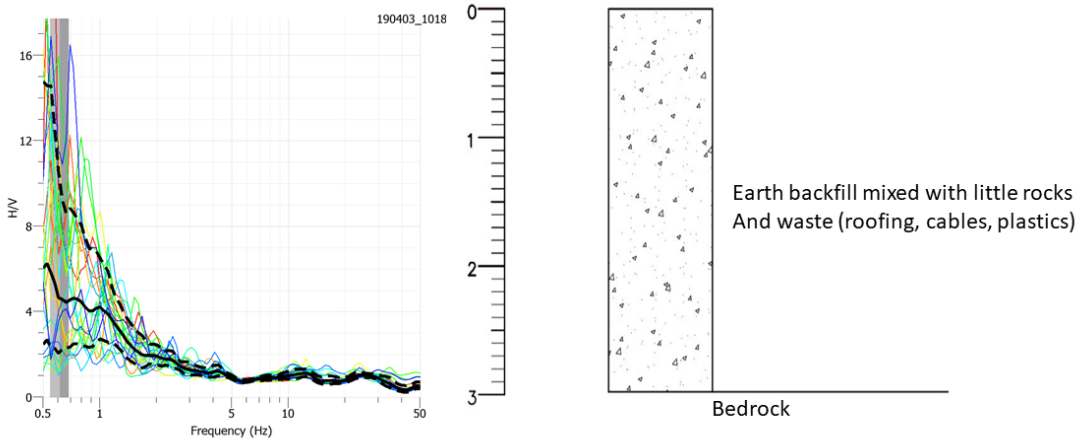

Figure 61. Comparison of the HVNSR graph of measurement 142 and the closest trench (Modified from RECOsol, 2012)

Other issues are also encountered. One of them is being defined in this report as the “structure effect”. It is important to remind, that SESAME (2004) recommended to take HVNSR measurements far from any structure, e.g. wall and trees. Indeed, in certain cases, this can cause the apparition of undesired peaks. One of the main examples is the measurement n°169 (***Figure 62***), located near the northern limit of the old quarry. Indeed, two clear peak frequencies are being identified. However, when the closest trench, i.e. n°11 (RECOsol, 2012), is analysed, it displays only a surficial layer of silt overlaying directly the bedrock. Regarding the amplitude of the second peak and its frequency, it is possible to relate it to this surficial layer, given the previous results of measurement n°185 (***Figure 57***). The first peak frequency does not match the borehole log and is probably not cause by a layer in the subsurface. The most probable explanation is that the source of this peak was located either in the northern cliff of the old quarry or in the embankment located near the measurement point. It remains difficult to precisely decide which one is causing the apparition of the peak. Regarding the results of n°170 (***Annex 9.5***) located closer to the cliff and further to the embankment, it is assumed that the source is within the embankment although a doubt subsists because the amplitude of the peak is not as important as for measurement n°172 (***Figure 58***).

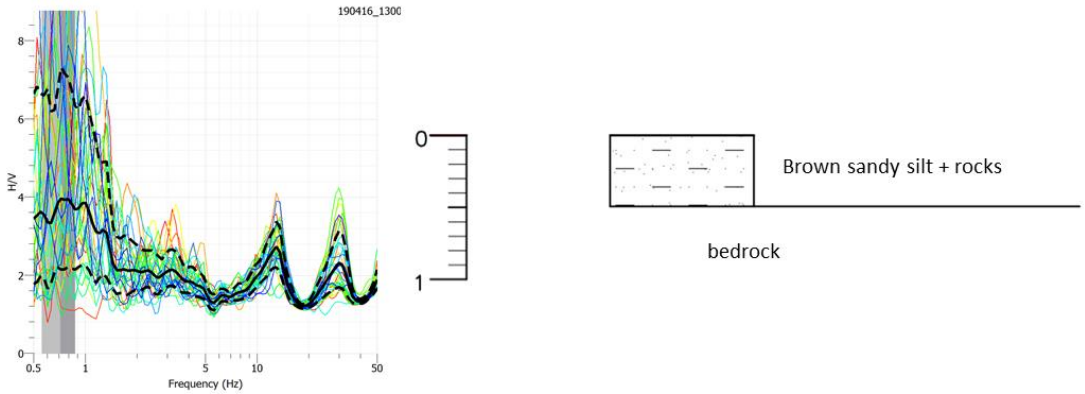

Figure 62. Comparison of the HVNSR graph of measurement 169 and the closest trench (Modified from RECOsol, 2012)

Now that it has been proven that the HVNSR could be used to define different zones within the lower part of the site, it is important to focus on the main purpose of this report, which is a 3D modelling of the landfill. As already mentioned (***Section 5.2***), the 3D modelling is performed by interpolating the frequency between each point inducing some uncertainty. Due to the nature of the measurements, it is impossible to display the 3D block in one piece. It is therefore decided to display three of the most interesting profiles computed from the HVSNR (***Figure 63***). Note that the scale representing the H/V amplitude is limited to 5 for a better visualization.

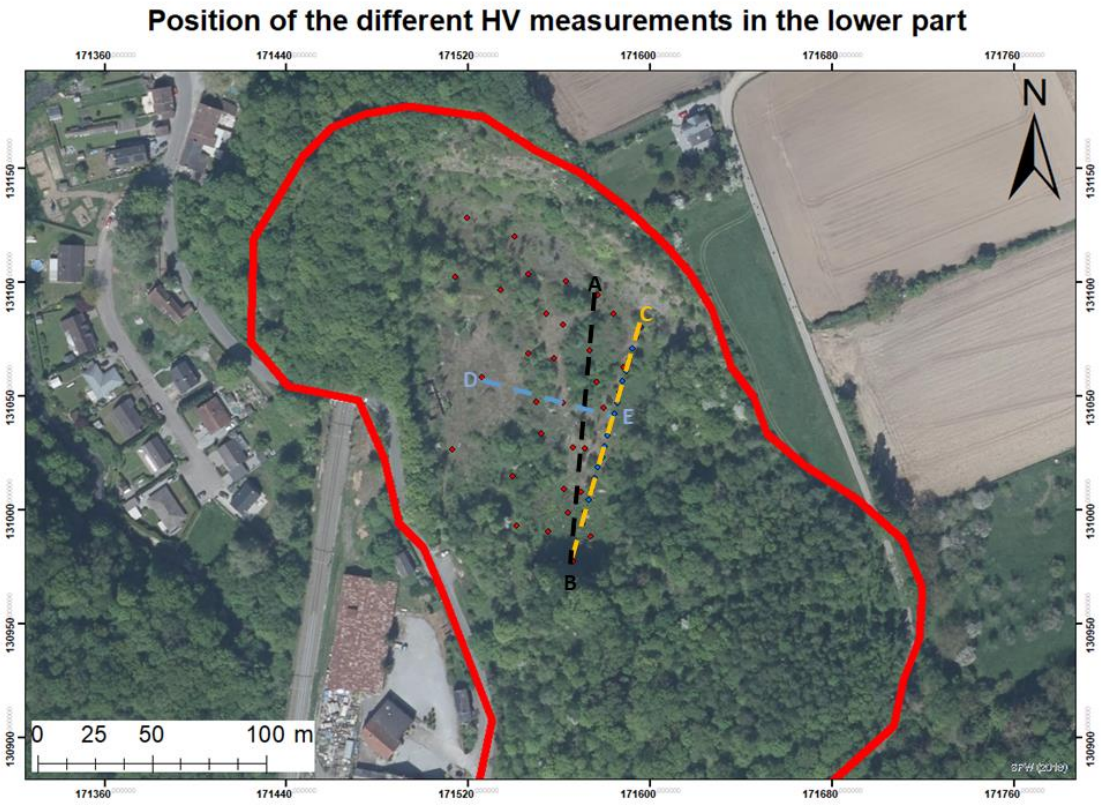

Figure 63. Map of the 3D HVNSR profiles displayed for the lower part (Adapted from Service Public de Wallonie, 2018)

The first profile (A-B) displayed is the same cross-section as the one selected for the interpretation of the 3D ERT (showed in black in ***figure 63***). It was obviously chosen to find concordances between the methods, validating their purpose in the frame of the characterisation of a landfill. Starting from the southern part, i.e. from B, a peak at a frequency around 10 Hz is clearly standing out during the first 30 m (***Figure 64***). Regarding the previous HVNSR and ERT analyses, it is possible to identify this peak as the mark of a certain thickness of a layer of lime and ashes. This frequency is still visible on the next 20 m but is accompanied by multiple peaks, caused by the presence of waste and backfill. The lime and ashes peak finally disappears, while the multiple peaks of waste and backfill still continue for 15 m. Then, no peak frequency occurs, signifying that the bedrock is reached. The amplitude around 2.5 Hz, occurring in the northern part, is probably caused by the previously defined “structure effect”.

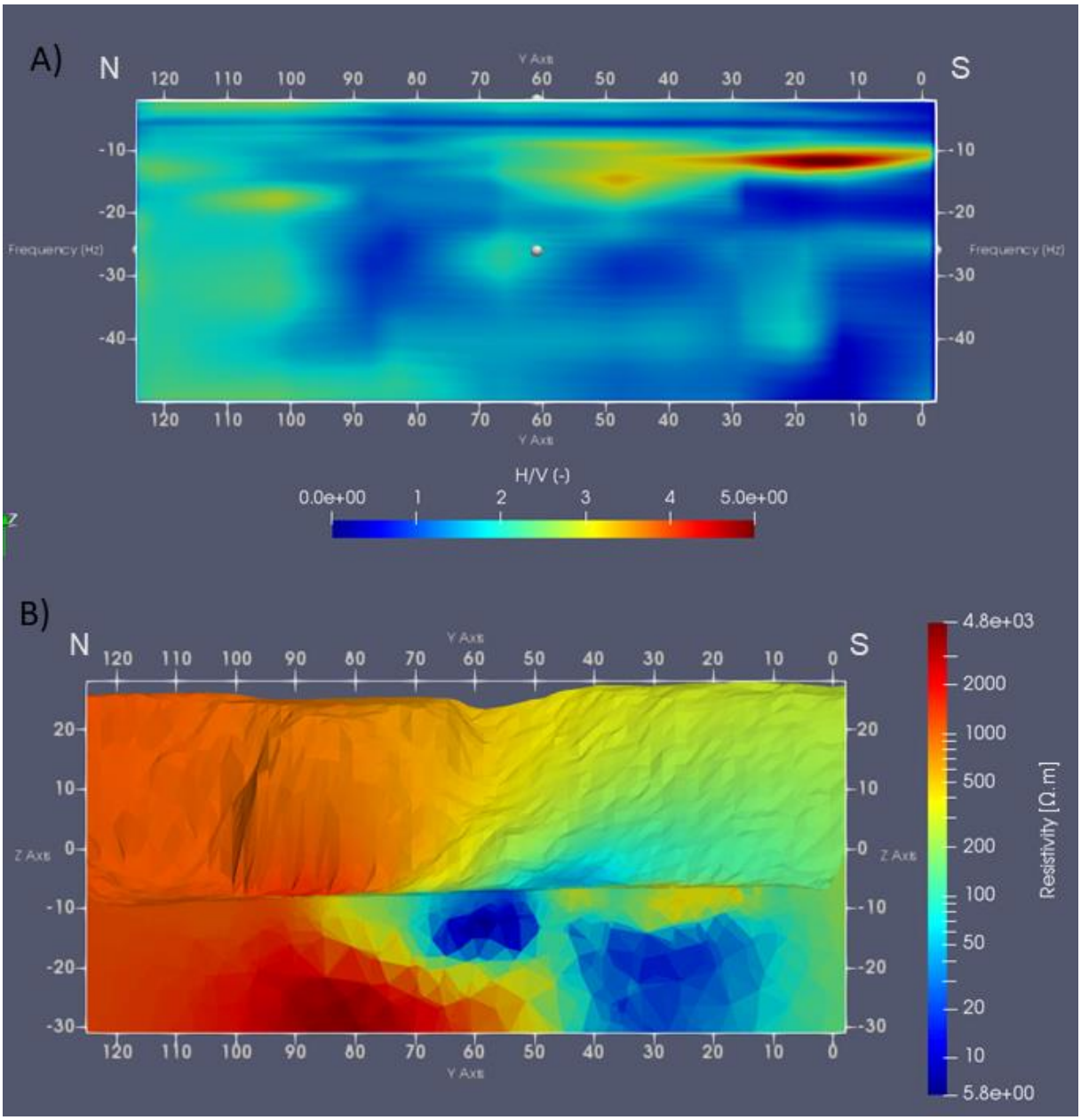

Figure 64. HVNSR cross-section **(A)** corresponding to the cross-section displayed during the ERT interpretation **(B)**

The next interesting profile (B-C) displayed, is the H/V measurements previously performed by the team of the geophysical team of the ULiège and myself in the frame of this master thesis. The profile is of interest as the different points were only 5 m distant, which renders the profile much more precise, and it was performed not far from the first profile, which enables a verification. ***Figure 65*** shows the same peak around 10 Hz in the southern part. This peak is once again clearly related to the lime and ashes. However, this time, the peak is visible on approximately 60 m, which is longer than for the first profile. This can be explained by the fact that the measurements are taken much closer to the ashes and lime massif. Besides the lime peak, after 30 m, another peak around 18 Hz lasts around 45 m. This large frequency peak is representative of the waste and backfill, known to occur in this region of the landfill. The higher H/V amplitude than 2 in the northern part was probably caused once again by the “structure effect”.

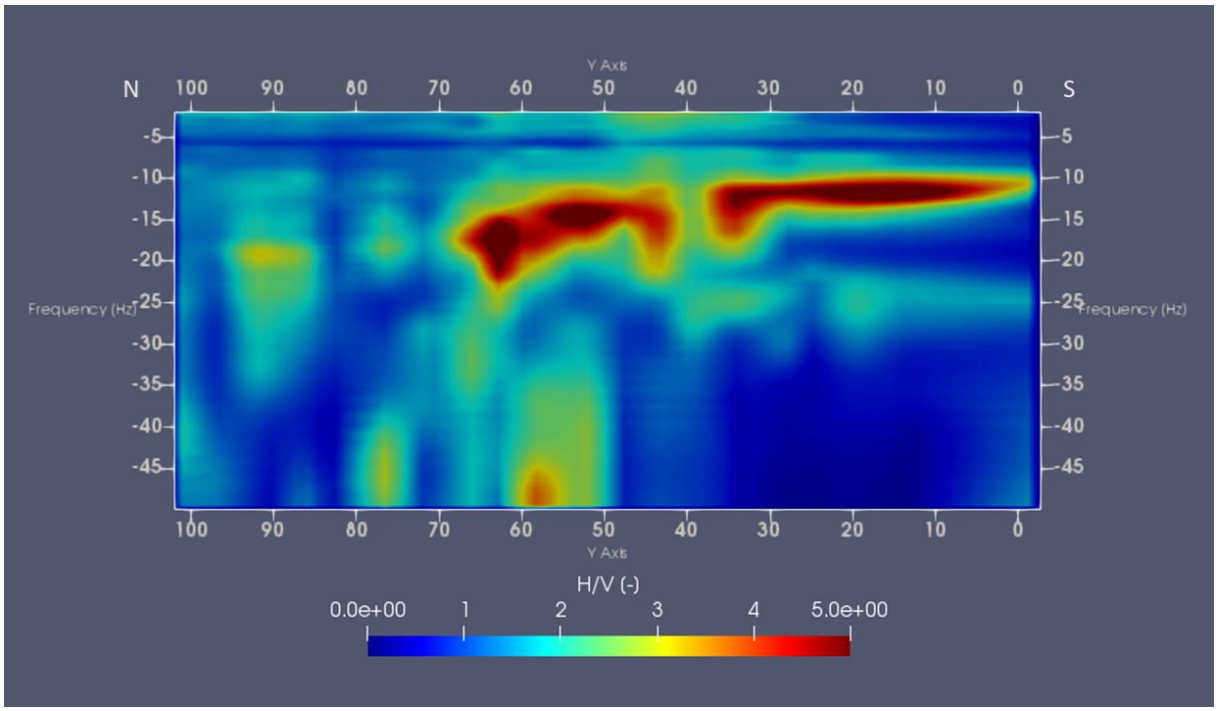

Figure 65. HVNSR profile of the measurements performed previously by the geophysical team of ULiège and myself

The last profile is taken perpendicularly to the two previous ones (D-E), in order to get an idea of the extension of the waste in this direction (***Figure 66***). Firstly, it should be noted that the high amplitude around 10 Hz in the western part is clearly an interpolation artefact. As it is already well known, in this zone, the bedrock is only overlaid by a thin layer of silt. This peak is caused by the interpolation of the frequency between the measurement points. Indeed, in this zone of the landfill, the amount of measurements was drastically reduced compared to the rest of the site, because of the lack of interest. The measurements performed in the two embankments surrounding this zone, consequently influences it and generates a fake peak at the same frequency as the one strongly occurring in the embankments. In fact, the real frequency of interest on this region is around 30 Hz, representing the layer of silt above the bedrock. The high amplitude shows that the fake peak also has as impact to reduce the effect of the other peaks occurring in the rest of the profile. It is therefore important to properly consider the peak of lower amplitude. At the east of the false peak, higher amplitudes occur for frequencies around 12 and 25 Hz and are linked to the waste present in this zone. The rest of the higher amplitude frequencies in the eastern part are also linked to the heterogeneous waste. However, at the eastern end of the profile, a peak around 10 Hz seems to develop, announcing the beginning of the layer of lime and ashes.

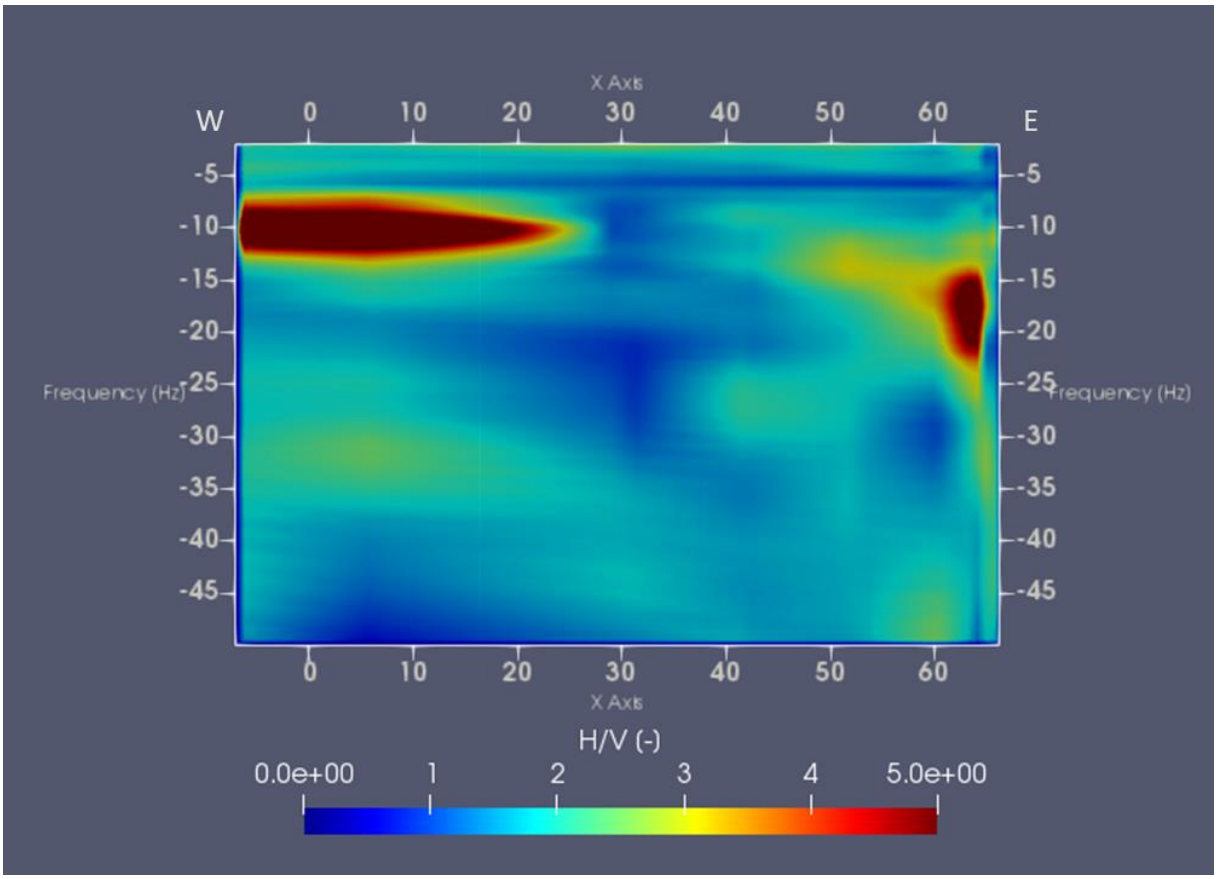

Figure 66. HVNSR perpendicular profile

The HVNSR technique proves to be useful for characterizing a landfill. It shows that it is possible to determine the layers occurring in the different zones of the landfill, by using their resonance frequencies. Computing profiles also shows that the changes occurring could be helpful in the frame of delimiting the different zones, once the peaks are clearly identified. However, HVNSR also shows limitations as every geophysical method. Without the information gathered by the previous invasive investigation, it would have been impossible to link the peak to the proper material. Furthermore, it remains sometimes difficult to connect all the peaks to the observed material given the high heterogeneity of the subsoil, which also renders difficult the calculation of the layer thickness.

6.2.2 Upper part

In this part of the landfill, two major waste layers were reported by previous investigations. As observed in the historical view of the site (***section 4.1***), a massive amount of lime was firstly discarded and was thereafter topped with a thick layer of ashes. The subsurface at this location is consequently considered as relatively homogenous with well-separated layers. Therefore, contrarily to the lower part of the site, it is possible to determine the seismic velocity of both layers by using the two previously drilled boreholes and subsequently to define their thickness, by assuming certain hypotheses***. Figure 67*** displays the map of all the measurements in the upper part, combined with some H/V graphs representative of their zone.

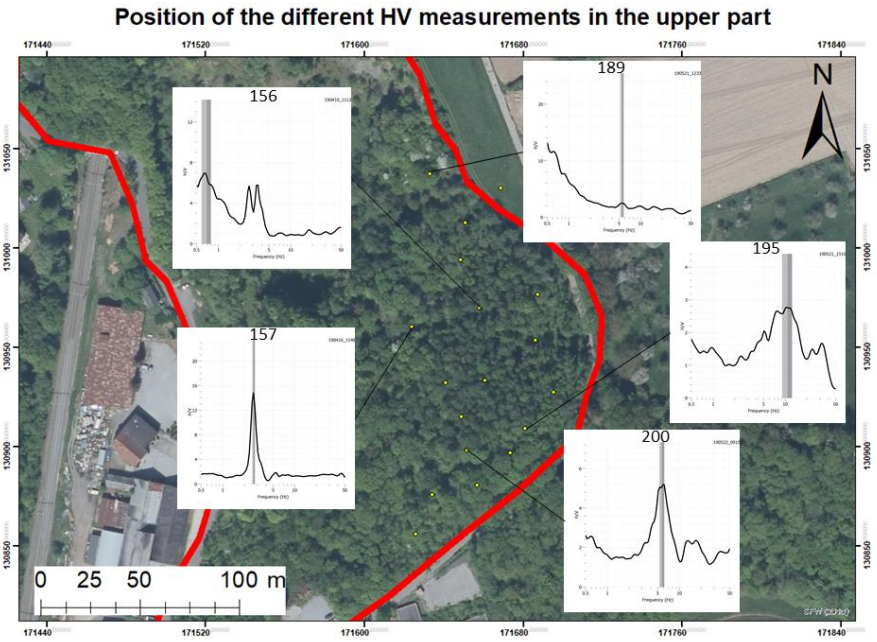

Figure 67. HVNSR measurements map of the upper part and representative graphs of the different zones (Adapted from Service Public de Wallonie, 2018)

The first H/V graph analysed is the measurement n°156 (***Figure 68***). Two well-distinct peaks are visible at frequencies of 2.68 and 3.43 Hz. Fortunately, this measurement location is closely situated to the borehole n°4, drilled in 2018 by IRCO (***Annex 9.1***). The latter indicates a first layer of ashes of around 14 m, overlaying a layer of 12 m of lime, naturally explaining the occurrence of two peak frequencies. The lowest frequency can be linked with the layer of lime while the second peak can be related to the ashes.

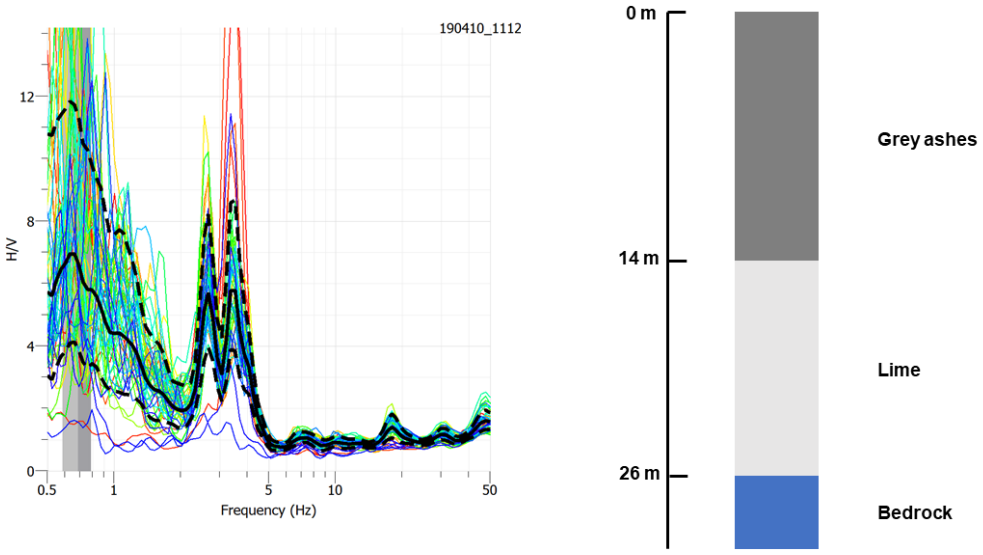

Figure 68. HVNSR graph of measurement 156 compared to the scheme of the corresponding boreholes

The next measurement was taken next to the other borehole performed by IRCO, i.e. n°5 (***Annex 9.1***). Measurement n°157 shows a single well-marked peak (***Figure 69***), whereas the borehole still indicates two different layers. However, the thickness of the lime layer is yet only of 3.5 m, while the ashes layer has a thickness around 21.5 m. The fact that the layer of lime is not detected by the HVNSR method is assumed to be due to the fact that both layers have a close seismic velocity and that the lime peak is part of the ashes peak and therefore cannot be discriminated.

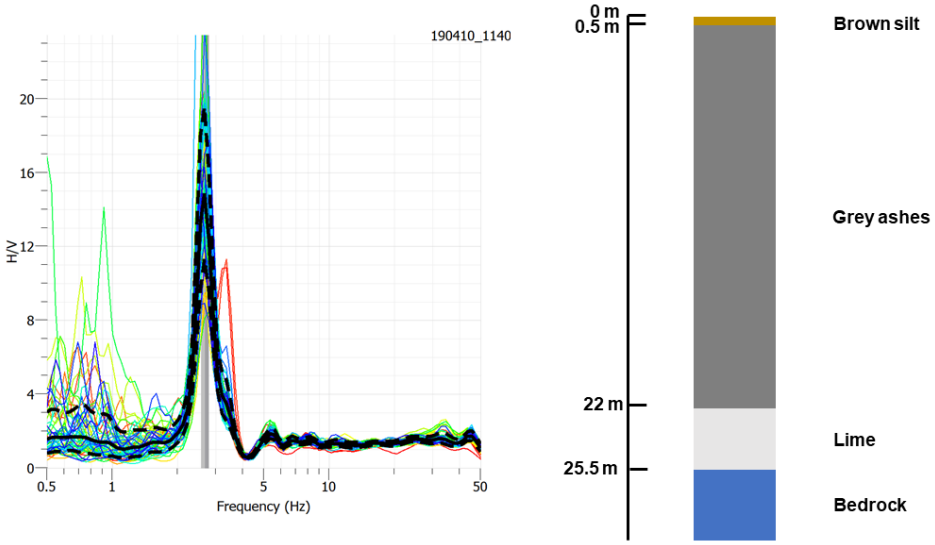

Figure 69. HVNSR graph of measurement 157 compared to the scheme of the corresponding boreholes

Measurement n°189 was taken in the northern part, near the cliff of the quarry. The H/V curve is relatively flat even though two small peaks occur at relatively high frequency (***Figure 70***). These peaks are probably not caused by the lime and ashes but by some thin layers of soil above the bedrock. Therefore, this measurement shows, the northern limit of the ashes and lime hill. This hypothesis is supported by measurement n°190, showing the same kind of H/V relation (***Annex 9.5***).

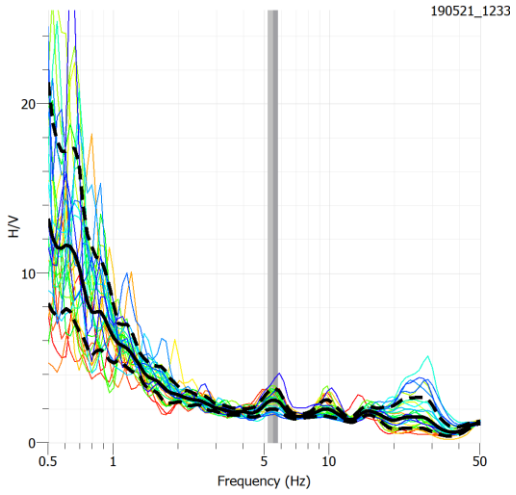

Figure 70. HVNSR graph of measurement 189

Measurement n°195 is considered as representative of the situation in the southern part of the upper zone (***Figure 71***). The HVNSR graph is less clear than for measurement n°156 although the two peaks are still present but at higher frequencies, implying a decrease of the total thickness of both layers. The two new peaks appearing at 25 and 35 Hz are considered as insignificant in this case, considering their low amplitude.

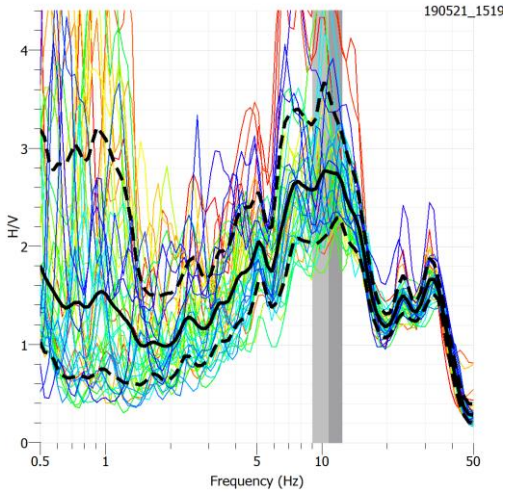

Figure 71. HVNSR graph of measurement 195

Measurement n°195 marks the southern limit of the ashes and lime massif. Indeed, measurements from n°197 to n°202 follow a different H/V pattern (***Annex 9.5***). In the field, the difference between each zone of the upper part was marked by the topography, with the southern part 3 m lower. Furthermore, walking through this part of the site, it was clear that the surficial material was completely different of the central part, which agrees with the results of the previous EM performed in this part. Moreover, the photography of 1963 indicates that some activity was going on in this part of the site, but due to the poor quality of the photography it is hard to determine precisely what type of activity (***Figure 14***). However, from the next aerial photography of 1976, it is clear that this part was already recovered by nature and was therefore not used for the landfilling of lime and ashes.

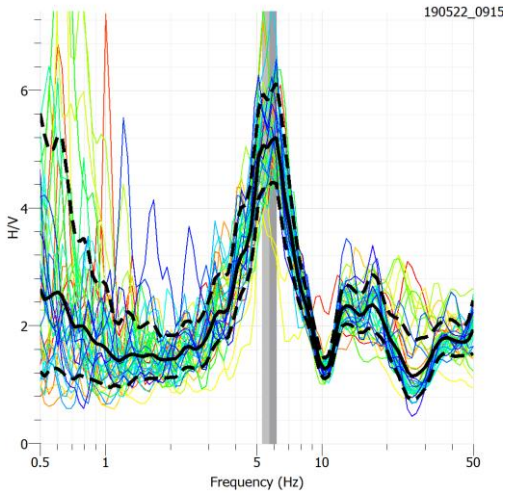

Figure 72. HVNSR graph of measurement 200

Measurement n°200 is chosen to represent this part of the site (***Figure 72***). Two peaks really close to each other, i.e. at frequencies around 5.5 and 6.5 Hz, and multiple other peaks at higher frequency can be seen. Unfortunately, no boreholes or trenches were performed in this part of the site, rendering the verification of different hypotheses difficult. However, the most probable one, considering the heterogeneity showed by the H/V graph and the observations during the fieldworks, is that the bedrock is overlaid by some backfills and a layer of soil. Furthermore, due to the topography, some measurements were performed near small walls in the northern and western direction. Consequently, it remains plausible that some of the measurements are impacted by the already discussed “structure effect”.

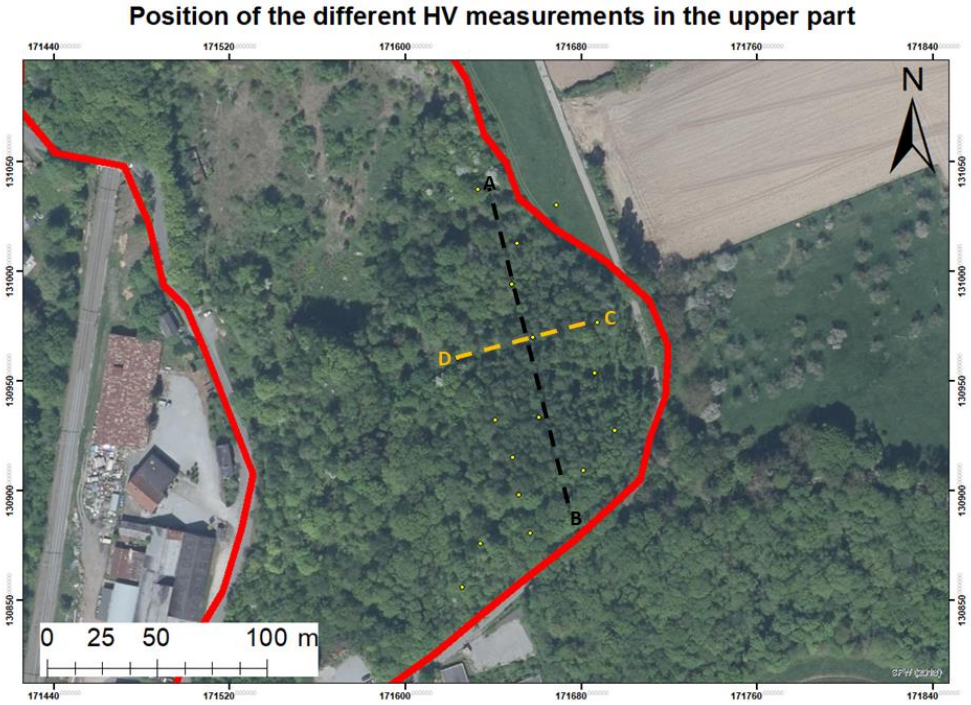

Figure 73. Map of the 3D HVNSR profiles displayed for the upper part (Adapted from Service Public de Wallonie, 2018)

A suitable option to observe changes between each zone, is to perform once again the 3D H/V block and to display some of the profiles generated from the interpolation between each point. ***Figure 73*** maps the location of the two profiles chosen to analyse the evolution of the subsurface in both directions.

The first profile displayed is the one in the north-south direction (***Figure 74***). In the north, no clear frequency stands out during the first 20 m, indicating that no lime or ashes is overlaying the bedrock. Then, the frequencies of the lime and the ashes are observed during approximately 95 m. Finally, in the southern part, some scattered frequencies occur, indicating the changeover from the lime and ashes to the backfilled ground.

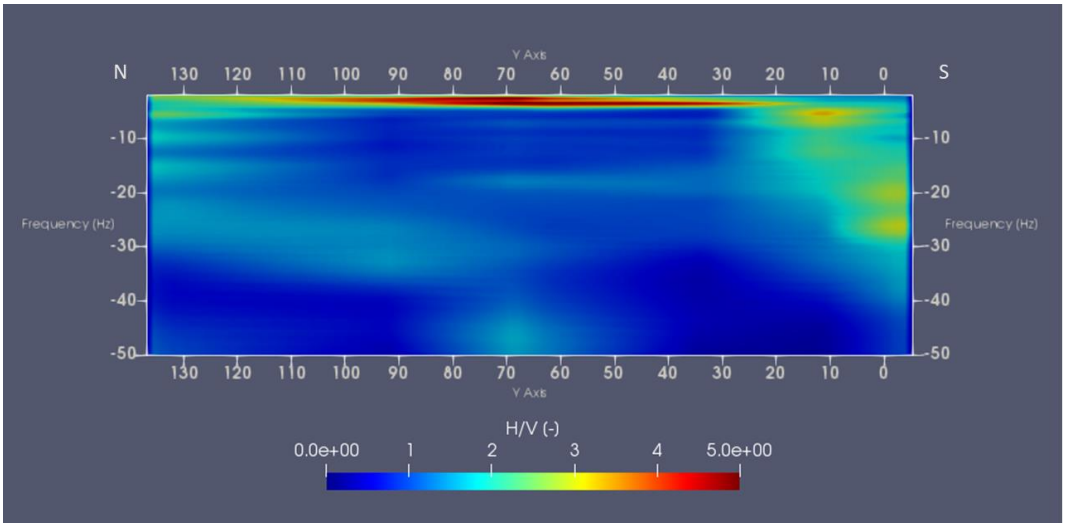

Figure 74. HVNSR profile in the north-south direction in the upper part of the site

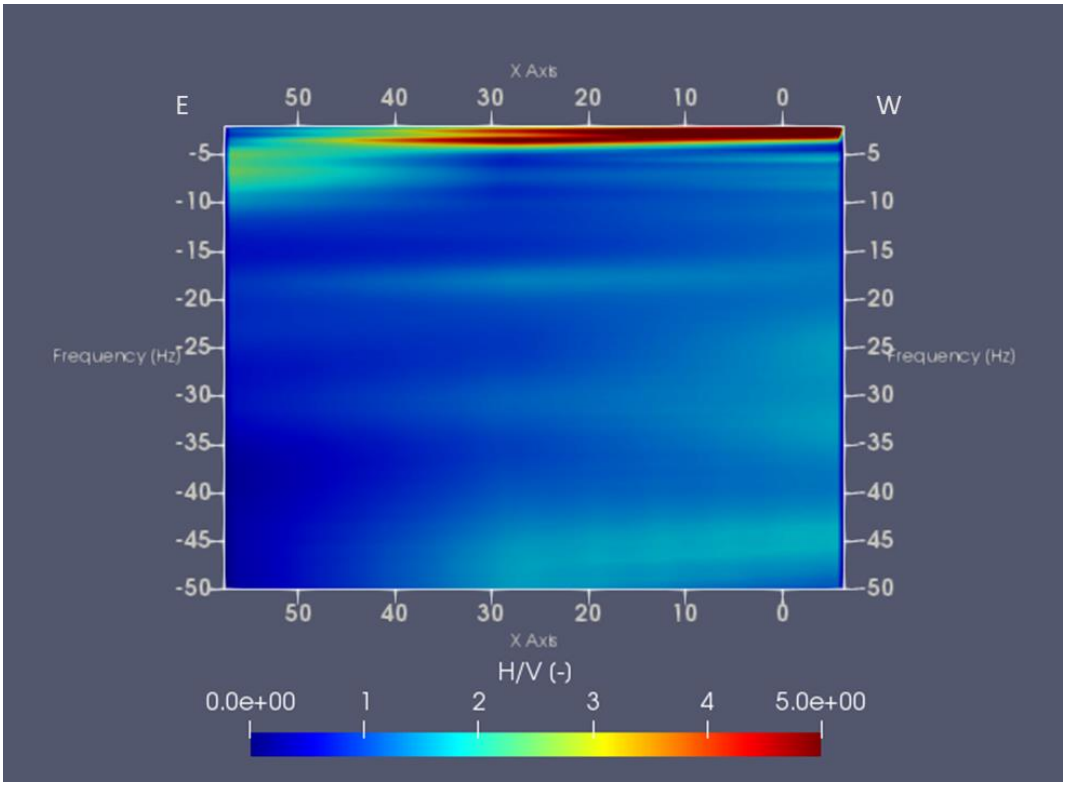

Figure 75. HVNSR profile in the east-west direction in the upper part of the site

The next profile considers three points in the central part and in the east-west direction (***Figure 75***). Starting from the western part, one major frequency is highlighted and indicates that the layer of ashes is much thicker than the one of lime. Then, after approximately 8 m in the eastern direction, two frequencies show a high amplitude. At the eastern end, two higher frequencies also have a higher H/V ratio. They are still linked to the ashes and lime but the layers are thinner than formerly observed. The transition in depth is not well marked in the H/V representation because of the low amount of measurements performed. However, it remains sufficient to understand that the thickness of the complete layer of ashes and lime is decreasing in the eastern direction. The spatial distribution of lime and ashes is settled. The next step is, therefore, to compute the thickness of each layer and subsequently the total thickness of the waste. The first calculation that has to be done is the seismic velocity of both materials. This is achieved for the ashes layer by combining the information given by the boreholes close to measurement n°157 and the formula of ***equation 29***. As previously assumed, the layer of lime is too thin to detect the change at the interface with the ashes, causing the apparition of a single peak in the H/V graph. It is decided to account the lime layer as part of the ashes layer, which reaches consequently a thickness of 25.3 m. Given this assumption and the peak frequency of measurement n°157, the V_s obtained for the ashes layer is 271 m/s. Then, measurement n°156 and borehole n°4 are used to compute the V_s of the lime layer. Using the ***equation 32*** and the calculated V_s, the estimated thickness of the ashes layer is computed. It is estimated around 19.7 m, which is bigger than what the boreholes indicates. The main explanation provided is that the V_s of each layer are close to each other as early discussed and, in this way, it is difficult to clearly identify the change of material in depth. Consequently, to balance and to respect the correct total height of the combined layer, the layer of lime is fixed at 6.5 m instead of 12 m. This has for effect to underestimate the lime layer, while the ashes one is overestimated. Nevertheless, it is possibly the best assumption to properly estimate the total thickness of the waste. ***Equation 32*** and the frequency of the first peak in the H/V graph enables the calculation of the lime V_s, which is estimated at 318 m/s, which complies with the assumption that both V_s are relatively close. The rest of the thicknesses at each HVNSR measurement are computed following these two estimated V_s. The frequencies attributed and the results obtained are displayed in ***table 6***. The map of the measurements the H/V graphs is presented in ***annex 9.4***. All the total depths finally obtained, complies relatively well with each other and the total depth observed in the two boreholes. Furthermore, the depth obtained confirms that it decreases when the measurement was performed along the road in the eastern part.

Table 6. Thickness calculated from the HVNSR measurements

N° of measurement	f_0 [Hz]	f_1 [Hz]	$H_{ashes\ m}$[]	H_{lime} [m]	Total H [m]
187	2.92	2.78	23.2	1.4	24.6
188	4.1	2.81	16.5	8.9	25.4
189	**BEDROCK**				
190					
191	6.89	4.95	9.8	4.5	14.3
192	4.05	3.59	16.7	2.5	19.2
193	3.47	2.84	19.5	5.1	24.6
194	3.47	2.66	19.5	7	26.5
195	10.91	7.62	6.2	3.1	9.3
196	6.89	4.53	9.8	6	15.8

Given that the lateral extension is approximately delineated and that the depth is known at certain locations, it is possible to compute the total amount of the combined waste, i.e. lime and ashes. The use of this method leads to an estimation of the total waste in the upper part of 172 900 m^3, with the lime and the ashes accounting respectively for 35 750 m^3 and 137 150 m^3. Both materials are underestimated compared to the previous estimation made by IRCO (2018). Besides the choice of the approximation method, part of the explanation is also the HVNSR measurements that could only be performed on flat surface. Therefore, the waste lying in the slope between the upper and lower parts is not taken into account.

Based on these computed depths and the previous information, it is possible to design a new conceptual model with North-South and West-East cross-sections, through the ashes and lime massif (***Figure 76***).

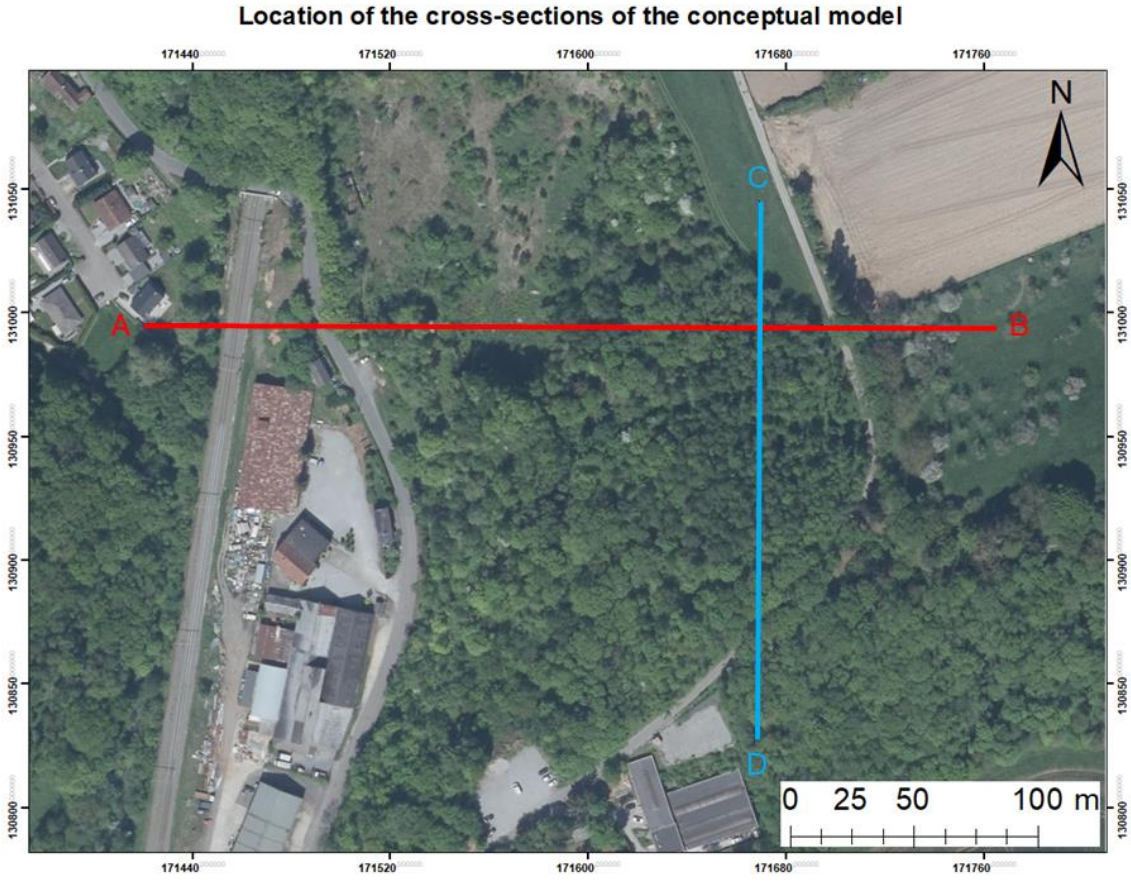

Figure 76. Location of the two cross-sections used as conceptual model.

Figure 77 displays the W-E cross-section. In the eastern part, the abrupt transition inside the ashes and lime body is due to the use of the Voronoi diagram and the depth is probably greater in this zone. Indeed, the polygons surrounding the lower depth points are probably too large compared to reality. Moreover, the depth of the ashes and lime body in the sloped part of the site is a complete extrapolation, given that HVNSR measurements and boreholes could not be performed in this part of the site. Furthermore, the part indicated that heterogeneous waste also partially contains lime or ashes and was fixed following the information given by the former invasive surveys.

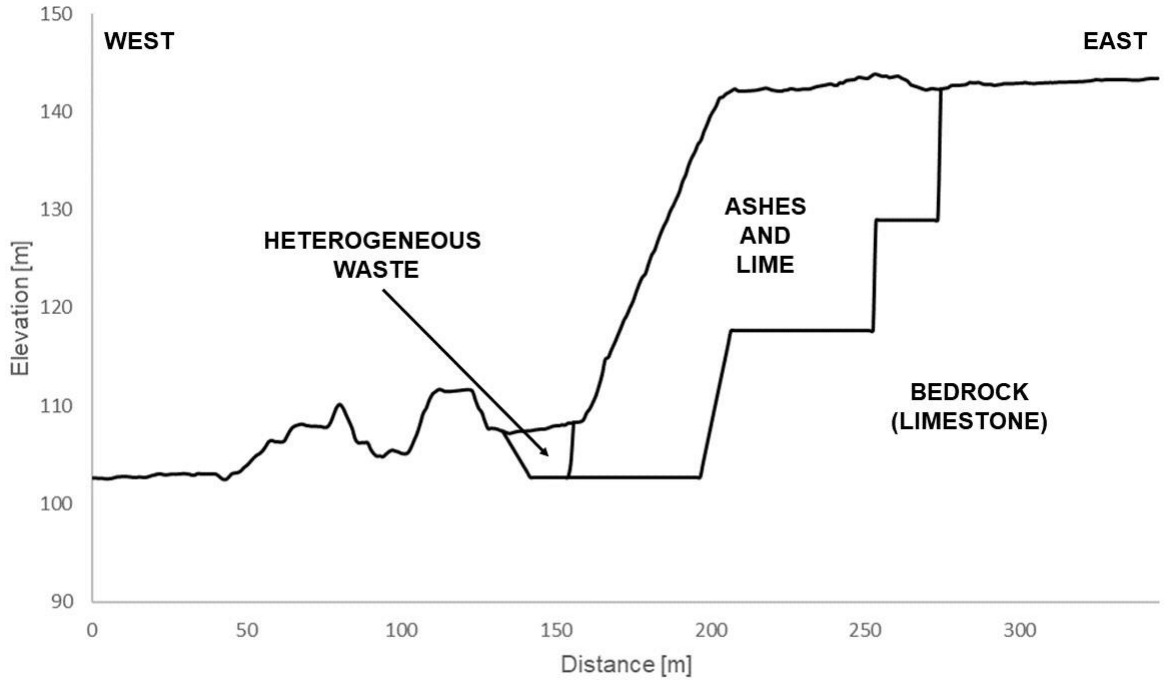

Figure 77. W-E cross-section

The N-S cross-section also displays interesting results (***Figure 78***). One abrupt step in the middle part of the ashes and lime body shows once again the limitation of using Voronoi diagram. Indeed, it is only due to the influence of a point taken relatively far from the cross-section, but whose diagram still impacts the cross-section. Furthermore, the lower depth in the northern end of the body is once again probably due to the overestimation of the influence zone of a bordering measurement point. Further north, as it was previously assumed, soil and backfill probably occur. Nevertheless, the lateral limits as well as the depth remains unknown.

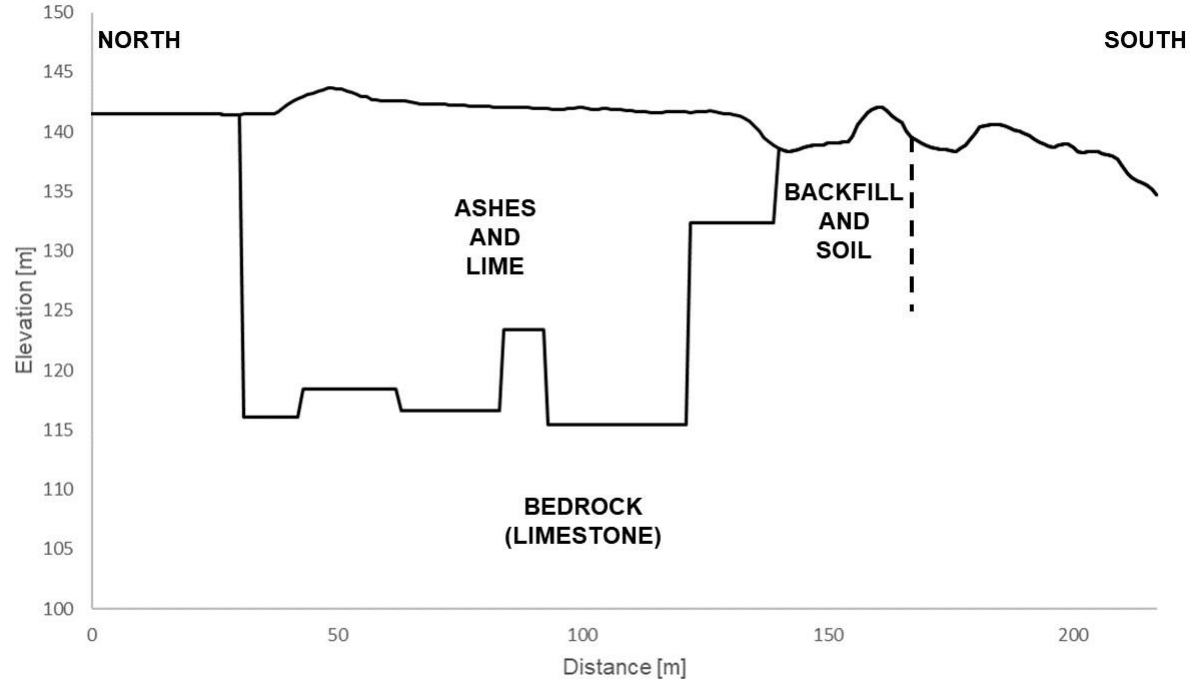

Figure 78. N-S cross-section

7 PERSPECTIVES AND CONCLUSION

The first aim of this report was to provide an appropriate 3D model of the waste distribution in the landfill using ERT and IP By the previous invasive and non-invasive surveys, it was already known that a body of lime and ashes occurred in this zone. Due to the pollutants contained in these materials and regarding the previous electrical investigations in Onoz and previous studied on other sites (Caterina et al., 2017), a highly conductivity layer was expected. One of the limitations of those type of layer generated by the model was that it could distort or unable the detection of the bedrock (Dumont et al., 2017). A 3D synthetic model, with the actual designed survey, was subsequently performed, previously to the actual data inversion, in order to observe the impact of such a layer on the model. It showed that the conductive layer had clearly impacted the bedrock detection, detected much deeper than it should have been. Unfortunately, this effect was also observed in the actual data model. However, the information provided by the synthetic model helped for a proper interpretation of the resulting images. It was also possible to approximately delineate the different materials in the surficial part of the model.

Moreover, the inversion parameters also showed to play an important role, with the “blocky” inversion being closer to the actual reality than the smooth inversion. However, the roughness of the images obtained from the sharp inversion rendered the lecture of the model more complicated. The main problem of this part of the study was the lack of a correct model appraisal. In fact, having distorted information is not optimal but is only a problem if the model appraisal indicates that the displayed information is suitable. Unfortunately, this was the case for the present 3D model. The only model appraisal obtainable was the DOI. As the rest of the results, the DOI was strongly affected by the highly conductive layer, which enforced the all models to converge to lower resistivities, especially below the thickest conductive layer, and even in cases of highly resistive reference models. It would have been interesting to get an appropriate sensitive model from E4D. Unfortunately, this could not be achieved in the frame of this report.

In terms of chargeability, the surficial waste could also be well defined, while the thickness of the lime and ashes layer, showing higher chargeability than the rest of the materials occurring in Onoz, was, once again, overestimated.

Furthermore, the four 2D profiles derived from the 3D in-line measurements, corroborated the 3D model information and showed the same distortion, near the thickest conductive layer.

To get accurate information on the bedrock depth different solutions could be considered. Another geometry of ERT lines for the 3D model could be performed. However, the site renders this solution difficult. A second solution could be to test another array of measurement. Indeed, a 3D gradient array, instead of the present dipole-dipole, could give better results, considering that it is more sensitive to vertical changes than the dipole-dipole. The third proposed solution is the use of a seismic method. Seismic methods have always been the most suitable techniques to detect the depth of the bedrock. Nevertheless, as mentioned in ***section 4.4***, a seismic investigation was already performed by the ULiège team and the BGS and the complexity of the results induces a long and difficult processing of the results.

The third method used during this thesis was the HVNSR. Many outcomes were expected from this method and the results were dependent of the site of measurement. Firstly, in the lower part of the site, the HVNSR was used to delineate the different waste zones, by simply crossing the information from the H/V graphs obtained with the boreholes and trenches. Relatively flat graphs, with small peak at a high frequency, around 30 Hz, could be related to zones where the bedrock was only overlaid by a thin silty layer. Another zone, outlined by two well-distinct peaks differing in frequencies on the graph, could be linked to area where the bedrock was overlaid by a lime and ashes layer and heterogenous waste. It should be distinguished from two embankments showing the same H/V pattern, but which were probably made of backfill and soil. Other locations displayed multiple peaks that were caused by the heterogeneity of the occurring waste. Several areas induced completely distorted graphs, generated by the nearby structures, i.e. quarry walls, embankments and trees. This outcome was defined as the “structure effect”. A way to more precisely define the different wastes and the thickness of their layer, would be to perform a MASW survey to get the V_S of each material. Combined with the HVNSR, this would allow to compute the thickness of the different occurrences.

In the upper part of the site, the HVNSR was combined with two available boreholes in order to compute their approximate V_S which were relatively close to each other. Following some assumptions, it was possible to calculate the thickness of the layers of lime and ashes, eventually allowing the approximation of the total volume of the waste in this zone. The use of HVNSR was, in this zone, the only possible geophysical method to compute the depth of each layer. Indeed, compared to the space available for a usual seismic profile, the bedrock was way too deep to be detected. Furthermore, by simply observing the different H/V graphs and the soil during the fieldworks, it was possible to properly delineate the lateral extension of the lime and ashes, once again emphasising the potential interest of HVNSR for this application.

7.1 On the site future development

One of the potential final outcome of the Onoz landfill is a complete sanitation and rehabilitation of the site, along with the maximal revalorization of the waste. The fact that most of the waste is located in a Natura 2000 zone named “Vallée de l’Orneau” may complicate the whole process. Indeed, following the Walloon government decree relative to the rehabilitation plans of 2007 (Section 2, Art 3), modified in 2017 and 2018, besides the normal procedures defined for a rehabilitation plan, it is necessary to provide a complete impact assessment, concerning the effects on species and on habitats of interests on the site. In the present case, the rehabilitation of the site would imply a complete removal of the ashes and lime massif which would, in turn, impede most of the fauna and flora in the zone, if no special prevention limits were applied. Furthermore, the noise generated during the rehabilitation would be quite deafening. Given the previous issues, it would be necessary to show that no alternative exist to better handle the problem occurring in Onoz and to show how impacting would be the situation if the landfill was kept in the remaining state. As demonstrated by the analyses performed during the different investigations and although the situation was not defined as urgent (IRCO, 2018), the pollutants present in the soil could have, at long-term, an important impact on the environment. However, as yet discussed, the rehabilitation

plan would have to be designed properly to limit the impact on the wildlife that developed in Onoz, especially in the *GBI* zone.

Furthermore, it is imperative to find suitable application for the waste that would be extracted in Onoz. Three major categories of waste stand out: the lime, the ashes and the heterogenous waste.

A panel of applications could be outlined for the lime layer. It could be used in the steel industry to remove impurities or in environmental applications, e.g. as reagent in the Flue Gas Treatment under the form of an alkaline slurry to remove sulphur dioxide (Hosansky, 2019). Furthermore, lime could be valorised in the chemical industry and more precisely in the plastic industry, but also in the agricultural sector, as acidity corrector for the soil (IMA Europe, 2014). However, considering the different pollutants present in the lime in Onoz, e.g. hydrocarbons and heavy metals, only one sector seems to be appropriate to the reuse of Onoz's lime within the constraint. Indeed, lime could be reused in the production of concrete or bricks as well as in the fabrication of mortars. The question of its application in soil stabilization remains open, due once again to the inner pollutants. The European Industrial Gases Association agrees with most of these applications (EIGA,2017), even if the lime is present as carbide lime, by-products of the acetylene production, as it is the case in Onoz. However, it is worth mentioning that due to the variability of the characteristics of such a type of lime, its use in not always endorsed (OCDE, 1977).

We hypothesized that the ashes discarded in Onoz were coming from the coal plant of "*Auvelais*", probably resulting of fly ashes. The application of fly ashes in the construction sector has been demonstrated for a long time. It can be used as filler in asphalt concrete, as light aggregate or also in the Portland cement (OCDE, 1977). Moreover, fly ashes could also be useful in embankment as fill material (Vipulanandan et al., 1996; OCDE, 1977).

One essential point is the pozzolanic property of fly ashes. Indeed, in the presence of lime and water, the fly ashes would fix the lime and then strengthen (OCDE, 1977).

The heterogeneity of waste in the lower part of the site renders its treatment and the forecast of future applications more complex. Indeed, the biggest problem will be an optimal sorting of the waste before its reuse. It would probably not be cost-effective in the present case, due to the high heterogeneity and the relatively small amount of waste.

Besides having a positive environmental impact while remaining non-invasive, the use of multiple geophysical methods in landfill were proved to be economically favourable. Indeed, the study performed by ATRASOL (2018, Unpublished) pinpointed, that in the case of Onoz, the survey costs could be reduced by more than 40% for the same information. This further highlights the added value of geophysical methods in these types of fields. However, it was also demonstrated that the invasive methods, i.e. boreholes and trenches, cannot be completely abandoned, but could optimally be located thanks to the information provided by the geophysical investigations.

8 REFERENCES

- Abdel Aal, G.Z., Atekwana, E.A., Slater, L.D., Atekwana, E.A. (2004) 'Effects of microbial processes on electrolytic and interfacial electrical properties of unconsolidated sediments', Geophys. Res. Lett. 31. doi:10.1029/2004GL020030

- ADEME (2016) Guides des méthodes géophysiques pour la détection d'objets enfouis sur les sites pollués.

- Aenergies (2013) Réhabilitation du dépotoir de la carrière d'Onoz.

- Aster, R. C., Borchers, B. and Thurber, C. H. (2013a) 'Chapter One - Introduction', in Aster, R. C., Borchers, B., and Thurber, C. H. B. T.-P. E. and I. P. (Second E. (eds). Boston: Academic Press, pp. 1–23. doi: https://doi.org/10.1016/B978-0-12-385048-5.00001-X.

- Aster, R. C., Borchers, B. and Thurber, C. H. (2013b) 'Chapter Two - Linear Regression', in Aster, R. C., Borchers, B., and Thurber, C. H. B. T.-P. E. and I. P. (Second E. (eds). Boston: Academic Press, pp. 25–53. doi: https://doi.org/10.1016/B978-0-12-385048-5.00002-1.

- Athanasiou, E. N., Tsourlos, P. I., Vargemezis, G. N., Papazachos, C. B. and Tsokas, G. N. (2007) 'Non-destructive DC resistivity surveying using flat-base electrodes', Near Surface Geophysics. John Wiley & Sons, Ltd, 5(4), pp. 263–272. doi: 10.3997/1873-0604.2007008.

- ATRASOL SPRL (2018) Enhanced inventory framework sampling plan.

- Balia, R. (2018) 'Old municipal and industrial waste landfills: Examples of possible application of geophysical survey techniques for assessment prior to reclamation', Detritus, 1, pp. 110–115.

- Bentley, L. and Gharibi, M. (2004) 'Two-and three-dimensional electrical resistivity imaging at a heterogeneous remediation site', Geophysics, 69, pp. 674–680. doi: 10.1190/1.1759453.

- Binley, A. and Kemna, A. (2005) 'DC resistivity and induced polarization methods', in Hydrogeophysics. Springer, pp. 129–156.

- Bonnefoy-Claudet, S., Cornou, C., Bard, P.-Y., Cotton, F., Moczo, P., Kristek, J. and Fah, D. (2006) 'H/V ratio: A tool for site effects evaluation. Results from 1-D noise simulations', Geophysical Journal International, 167, pp. 827–837. doi: 10.1111/j.1365-246X.2006.03154.x.

- Brûlé, S. and Javelaud, E. (2013) 'Méthode H/V en géotechnique. Applcation à un modèle bicouche', Revue française de géotechnique, 142, p. 13.

- Carlson, N., Bouzid, N. and Byrd, R. (2015) 'Environmental applications of the IP method: Surveys of subsurface waste', The Leading Edge, 34, pp. 214–220. doi: 10.1190/tle34020214.1.

- Caterina, D., Beaujean, J., Robert, T. and Nguyen, F. (2013) 'Comparison of image appraisal tools for electrical resistivity tomography', Near Surface Geophysics, 11, pp. 357–639. doi: 10.3997/1873-0604.2013022.

- Caterina, D., Flores Orozco, A. and Nguyen, F. (2017) 'Long-term ERT monitoring of biogeochemical changes of an aged hydrocarbon contamination', Journal of Contaminant Hydrology, 201, pp. 19–29. doi: https://doi.org/10.1016/j.jconhyd.2017.04.003.

- Caterina, D., Isunza Marinque, I., Inauen, C., Watlet, A., Dashwood, B., De Rijdt, R., Dumont, G., Chambers, J. and Nguyen, F. (2019) 'Contribution of geophysical methods to the study of old landfills: A case study in Onoz (Belgium)', in 17th International waste management and landfill symposium, p. 15.

- Chambers, J., Kuras, O., Meldrum, P., D. Ogilvy, R. and Hollands, J. (2006) 'Electrical resistivity tomography applied to geologic, hydrogeologic, and engineering investigations at a former waste-disposal site', Geophysics, 71. doi: 10.1190/1.2360184.

- Chavez, R., Andrade, A., Cifuentes-Nava, G., argote-espino, D. and Hernandez-Quintero, E. (2018) 'Karst Detection Beneath the Pyramid of El Castillo, Chichen Itza, Mexico, by Non-Invasive ERT-3D Methods', Scientific Reports, 8. doi: 10.1038/s41598-018-33888-9.

- Clément, R., Oxarango, L. and Descloitres, M. (2011) 'Contribution of 3-D time-lapse ERT to the study of leachate recirculation in a landfill', Waste Management, 31(3), pp. 457–467. doi: https://doi.org/10.1016/j.wasman.2010.09.005.

- Council of the European Union (1999) 'Council Directive 1999/31/EC of 26 April 1999 on the landfill of waste', Official Journal of the European Communities, 182, p. 19.

- Dahlin, T. (2000) 'Short note on electrode charge-up effects in DC resistivity data acquisition using multi-electrode arrays', Geophysical Prospecting, 48, pp. 181–187. doi: 10.1046/j.1365-2478.2000.00172.x.

- Dahlin, T., Bernstone, C. and Loke, M. H. (2002) 'A 3-D resistivity investigation of a contaminated site at Lernacken, Sweden3-D Resistivity Contaminant Investigation', Geophysics, 67(6), pp. 1692–1700. doi: 10.1190/1.1527070.

- Dahlin, T., Zhou, B. (2004) 'A numerical comparison of 2D resistivity imaging with 10 electrode arrays', Geophys. Prospect. 52, 379–398. doi:10.1111/j.1365-2478.2004.00423.x

- Dahlin, T., Rosqvist, H. and Leroux, V. (2010) 'Resistivity-IP mapping for landfill applications', First Break, 28, pp. 101–105.

- Daily, W., Ramirez, A., Binley, A. and LaBrecque, D. (2005) '17. Electrical Resistance Tomography—Theory and Practice', in, pp. 525–550. doi: 10.1190/1.9781560801719.ch17.

- Delcambre, B. and Pingot, J.-L. (2008) Carte géologique de Wallonie : Fleurus-SPY (Notice explicative).

- Delgado, J., López Casado, C., Giner, J., Estévez, A., Cuenca, A., Molina, S. (2000) 'Microtremors as a Geophysical Exploration Tool: Applications and Limitations', pure Appl. Geophys. 157, 1445–1462. doi:10.1007/PL00001128

- Dumont, G., Pilawski, T., Dzaomuho-Lenieregue, P., Hiligsmann, S., Delvigne, F., Thonart, P., Robert, T., Nguyen, F. and Hermans, T. (2016) 'Gravimetric water distribution assessment from geoelectrical methods (ERT and EMI) in municipal solid waste landfill', Waste Management, 55, pp. 129–140. doi: https://doi.org/10.1016/j.wasman.2016.02.013.

- Dumont, G., Robert, T., Marck, N. and Nguyen, F. (2017) 'Assessment of multiple geophysical techniques for the characterization of municipal waste deposit sites', Journal of Applied Geophysics, 145, pp. 74–83. doi: https://doi.org/10.1016/j.jappgeo.2017.07.013.
- EIGA (2017) Guide to carbide lime applications.
- Elis, V., Ustra, A., Hidalgo-Gato, M., José Pejon, O. and Yukio Hiodo, F. (2016) 'Application of induced polarization and resistivity to the environmental investigation of an old waste disposal area', Environmental Earth Sciences, 75. doi: 10.1007/s12665-016-6157-5.
- Eurostat (2018) Landfill rate of waste excluding major mineral wastes. Available at: https://ec.europa.eu/eurostat/tgm/table.do?tab=table&plugin=1&language=en&pcode=t2020_rt110 (Accessed: 3 March 2019).
- Farquharson, C. G. (2007) 'Constructing piecewise-constant models in multidimensional minimum-structure inversions', GEOPHYSICS. Society of Exploration Geophysicists, 73(1), pp. K1–K9. doi: 10.1190/1.2816650.
- Fiandaca, G., Martorana, R., Messina, P. and Cosentino, P. (2010) 'The MYG methodology to carry out 3D Electrical Resistivity Tomography on media covered by vulnerable surfaces of artistic value', Il Nuovo Cimento B, 125, pp. 711–718. doi: 10.1393/ncb/i2010-10885-3.
- Gouvernement Wallon (2008) 20 décembre 2007- Arrêté du gouvernement wallon relatif aux plans de réhabilitation.
- Guéguen, P., Chatelain, J.-L., Guillier, B., Yepes, H. and Egred, J. (1998) 'Site effect and damage distribution in Pujili (Ecuador) after the 28 March 1996 earthquake', Soil Dynamics and Earthquake Engineering, 17(5), pp. 329–334. doi: https://doi.org/10.1016/S0267-7261(98)00019-0.
- Günther, T. and Rucker, C. (2018) Boundless Electrical Resistivity Tomography BERT { the user tutorial.
- Haghshenas, E., Bard, P.-Y., Theodoulidis, N., Atakan, K., Cara, F., Cornou, C., Cultrera, G., Di Giulio, G., Dimitriu, P., Fäh, D., De Franco, R., Marcellini, A., Pagani, M., Rovelli, A., Savvaidis, A., Tento, A., Vidal, S. and Zacharopoulos, S. (2008) 'Empirical evaluation of microtremor H/V spectral ratio', Bulletin of Earthquake Engineering, 6, pp. 75–108. doi: 10.1007/s10518-007-9058-x.
- Harjito, H., Suntoro, S., Gunawan, T. and Maskuri, M. (2018) 'Underground Leachate Distribution Based on Electrical Resistivity in Piyungan Landfill, Bantul', Indonesian Journal of Geography, 50, p. 34. doi: 10.22146/ijg.18315.
- Hermans, T.J. (2014) Integration of near-surface, geological and hydrogeological data with multiple-point geostatistics in alluvial aquifers, PhD Thesis. University of Liège.
- Hogland, W., Hogland, M. and Marques, M. (2011) 'Enhanced Landfill Mining: Material recovery, energy utilisation and economics in the EU (Directive) perspective', Proceedings International Academic Symposium on Enhanced Landfill Mining.
- Van Hoorde, M., Hermans, T., Dumont, G. and Nguyen, F. (2017) '3D electrical resistivity tomography of karstified formations using cross-line measurements', Engineering Geology, 220, pp. 123–132. doi: https://doi.org/10.1016/j.enggeo.2017.01.028.

- Hosansky, D. (2019) Flue gas treatment. Available at: https://www.britannica.com/technology/flue-gas-treatment (Accessed: 8 June 2019).
- IMA Europe (2014) Lime Recycling.
- IRCO SPRL (2018) Rapport: DSE1801 'Etude de caractérisation avec dispense d'étude d'orientation-Décret sols'.
- Isunza Marinque, I., Caterina, D., Van de Vijver, E., Dumont, G. and Nguyen, F. (2019) 'Assessment of geophysics as a characteriztion and monitoring tool in the dynamic landfill management (DLM) context: Opportunities and challenges', in 17th International waste management and landfill symposium, p. 11.
- Johnson, T. C. (2014) E4D: A distributed memory parallel electrical geophysical modelling and inversion code.
- Johnson, T. C., Versteeg, R. J., Ward, A., Day-Lewis, F. D. and Revil, A. (2010) 'Improved hydrogeophysical characterization and monitoring through parallel modeling and inversion of time-domain resistivity and induced-polarization data', GEOPHYSICS. Society of Exploration Geophysicists, 75(4), pp. WA27-WA41. doi: 10.1190/1.3475513.
- Jones, P. T., Geysen, D., Tielemans, Y., Van Passel, S., Pontikes, Y., Blanpain, B., Quaghebeur, M. and Hoekstra, N. (2013) 'Enhanced Landfill Mining in view of multiple resource recovery: a critical review', Journal of Cleaner Production, 55, pp. 45–55. doi: https://doi.org/10.1016/j.jclepro.2012.05.021.
- Kearey, P., Brooks, M. and Hill, I. (2002) An Introduction to Geophysical Exploration.
- Kemna, A. (2000) Tomographic inversion of complex resistivity- Theory and application, PhD Thesis. Bochum Ruhr-Univ.
- Koestel, J., Kemna, A., Javaux, M., Binley, A. and Vereecken, H. (2008) 'Quantitative imaging of solute transport in an unsaturated and undisturbed soil monolith with 3-D ERT and TDR', Water Resources Research. John Wiley & Sons, Ltd, 44(12). doi: 10.1029/2007WR006755.
- Konno, K. and Ohmachi, T. (1998) 'Ground-motion characteristics estimated from spectral ratio between horizontal and vertical components of microtremor', Bulletin of the Seismological Society of America, 88(1), pp. 228–241.
- LaBrecque, D. J., Miletto, M., Daily, W., Ramirez, A. and Owen, E. (1996) 'The effects of noise on Occam's inversion of resistivity tomography data', GEOPHYSICS. Society of Exploration Geophysicists, 61(2), pp. 538–548. doi: 10.1190/1.1443980.
- Leroux, V., Dahlin, T. and Svensson, M. (2007) 'Dense resistivity and induced polarization profiling for a landfill restoration project at Harlov, Southern Sweden', Waste management & research : the journal of the International Solid Wastes and Public Cleansing Association, ISWA, 25, pp. 49–60. doi: 10.1177/0734242X07073668.
- Li, Y. and Oldenburg, D. W. (2000) '3-D inversion of induced polarization data', GEOPHYSICS. Society of Exploration Geophysicists, 65(6), pp. 1931–1945. doi: 10.1190/1.1444877.

- Loke, M., Acworth, R., Dahlin, T. (2003) 'A comparison of smooth and blocky inversion methods in 2D electrical imaging surveys', Explor. Geophys. 34, 182–187. doi:10.1071/EG03182

- Loke, M. H. (2018) Tutorial : 2D and 3D electrical imaging surveys.

- Loke, M. H., Chambers, J. E., Rucker, D. F., Kuras, O. and Wilkinson, P. B. (2013) 'Recent developments in the direct-current geoelectrical imaging method', Journal of Applied Geophysics, 95, pp. 135–156. doi: https://doi.org/10.1016/j.jappgeo.2013.02.017.

- Di Maio, R., Fais, S., Ligas, P., Piegari, E., Raga, R. and Cossu, R. (2018) '3D geophysical imaging for site-specific characterization plan of an old landfill', Waste Management, 76, pp. 629–642. doi: https://doi.org/10.1016/j.wasman.2018.03.004.

- Martin, T. and Günther, T. (2013) 'Complex resistivity tomography (CRT) for fungus detection on standing oak trees', European Journal of Forest Research, 132, pp. 765–776. doi: 10.1007/s10342-013-0711-4.

- Maurya, P. K., Rønde, V. K., Fiandaca, G., Balbarini, N., Auken, E., Bjerg, P. L. and Christiansen, A. V (2017) 'Detailed landfill leachate plume mapping using 2D and 3D electrical resistivity tomography - with correlation to ionic strength measured in screens', Journal of Applied Geophysics, 138, pp. 1–8. doi: https://doi.org/10.1016/j.jappgeo.2017.01.019.

- Merriam, J. B. (2005) 'Injection Electrode Overprinting', Journal of Environmental and Engineering Geophysics. Environmental & Engineering Geophysical Society, 10(4), pp. 365–370. doi: 10.2113/JEEG10.4.365.

- Nakamura, Y. (1989) 'A method for dynamic characteristics estimation of subsurface using microtremor on the ground surface', Quarterly Report of Railway Technical research, 30, pp. 25–33.

- Nguyen, F., Kemna, A., Antonsson, A., Engesgaard, P., Kuras, O., Ogilvy, R., Gisbert, J., Jorreto, S. and Pulido, A. (2009) 'Characterization of seawater intrusion using 2D electrical imaging', Near Surface Geophysics, 7. doi: 10.3997/1873-0604.2009025.

- Nguyen, F., Van Rompaey, G., Teerlynck, H., Van Camp, M., Jongmans, D. and Camelbeeck, T. (2004) 'Use of microtremor measurement for assessing site effects in Northern Belgium interpretation of the observed intensity during the MS = 5.0 June 11 1938 earthquake', Journal of Seismology, 8, pp. 41–56. doi: 10.1023/B:JOSE.0000009498.84531.71.

- Nguyen, F., Ghose, R., Isunza Manrique, I., Robert, T., Dumont, G. (2018) 'Managing past landfills for future site development: A review of the contribution of geophysical methods', in: 4th International Symposium on Enhanced Landfill Mining. Mechelen, pp. 27–36.

- Nyquist, H. (1928) 'Certain Topics in Telegraph Transmission Theory', Trans. Am. Inst. Electr. Eng. 47, 617–644. doi:10.1109/T-AIEE.1928.5055024

- OCDE (1977) Utilisation des déchets et sous-produits en technique routière.

- Oldenborger, G., Routh, P. and Knoll, M. (2007) 'Model reliability for 3D electrical resistivity tomography: Application of the volume of investigation index to a time-lapse monitoring experiment', Geophysics, 72, pp. F167–F175. doi: 10.1190/1.2732550.

- Oldenburg, D. W. and Li, Y. (1994) 'Inversion of induced polarization data', GEOPHYSICS. Society of Exploration Geophysicists, 59(9), pp. 1327–1341. doi: 10.1190/1.1443692.

- Oldenburg, D. W. and Li, Y. (1999) 'Estimating depth of investigation in dc resistivity and IP surveys', GEOPHYSICS. Society of Exploration Geophysicists, 64(2), pp. 403–416. doi: 10.1190/1.1444545.

- Oubaiche, E. H., Chatelain, J.-L., Bouguern, A., Ben Salem, R., Machane, D., Hellel, M., Khaldaoui, F. and Guillier, B. (2012) 'Experimental Relationship Between Ambient Vibration H/V Peak Amplitude and Shear-wave Velocity Contrast', Seismological Research Letters, 83. doi: 10.1785/0220120004.

- Parasnis, D. . (1988) 'Reciprocity theorems in geoelectromagnetic work', Geoexploration, 25, pp. 177–198. doi: http://dx.doi.org/10.1016/0016-7142(88)90014-2.

- Park, H. (2015) 'Polytope bounded Voronoi diagram in 2D and 3D'. GITHUB.

- Parker, R. L. (1994) Geophysical inverse theory. Princeton: Princeton University Press.

- Van Passel, S., Dubois, M., Eyckmans, J., de Gheldere, S., Ang, F., Tom Jones, P. and Van Acker, K. (2013) 'The economics of enhanced landfill mining: private and societal performance drivers', Journal of Cleaner Production, 55, pp. 92–102. doi: https://doi.org/10.1016/j.jclepro.2012.03.024.

- Piña-Flores, J., Perton, M., García-Jerez, A., Carmona, E., Luzón, F., Molina Villegas, J. and J Sánchez-Sesma, F. (2016) 'The inversion of spectral ratio H/V in a layered system using the Diffuse Field Assumption (DFA)', Geophysical Journal International, 208. doi: 10.1093/gji/ggw416.

- RECOsol SPRL (2012) Etude interne. Site étudié: Rue de Montolivet 5190 Jemeppe-sur-Sambre.

- Reynolds, J. M. (2011) An introduction to Applied and Environmental Geophysics. Chichester: John Wiley & Sons, Ltd.

- Rucker, D. F., Levitt, M. T. and Greenwood, W. J. (2009) 'Three-dimensional electrical resistivity model of a nuclear waste disposal site', Journal of Applied Geophysics, 69(3), pp. 150–164. doi: https://doi.org/10.1016/j.jappgeo.2009.09.001.

- Ruthy, I. and Dassargues, A. (2014) Carte hydrogéologique de Wallonie : Fleurus-SPY (Notice explicative).

- Särkkä, H., Coulon, F., Kaartinen, T., Hannus, E., Hirvonen, S., Valjus, T., Lerssi, J., Dino, G., Rossetti, P., Griffiths, Z. and Wagland, S. (2018) 'INVESTIGATION OF MUNICIPAL SOLID WASTE (MSW) AND INDUSTRIAL LANDFILLS AS A POTENTIAL SOURCE OF SECONDARY RAW MATERIALS', 01-2018. doi: 10.26403/detritus/2018.3.

- Seigel, H. O. (1959) 'MATHEMATICAL FORMULATION AND TYPE CURVES FOR INDUCED POLARIZATION', GEOPHYSICS. Society of Exploration Geophysicists, 24(3), pp. 547–565. doi: 10.1190/1.1438625.

- Service Public de Wallonie (Cartographer) (2018) WalOnMap. Available at: http://geoportail.wallonie.be/walonmap

- SESAME European research project (2004) Guidelines for the implementation of the H/V spectral ratio technique on ambient vibrations. Measurements, processing and interpretation.

- Sigmund, U. (2018) 'Sorting with ballistic separators', in: 4th International Symposium on Enhanced Landfill Mining. Mechelen, pp. 89–94.

- Singh, A. P., Parmar, A. and Chopra, S. (2017) 'Microtremor study for evaluating the site response characteristics in the Surat City of western India', Natural Hazards, 89(3), pp. 1145–1166. doi: 10.1007/s11069-017-3012-2.

- Slater, L., Binley, A. M., Daily, W. and Johnson, R. (2000) 'Cross-hole electrical imaging of a controlled saline tracer injection', Journal of Applied Geophysics, 44(2), pp. 85–102. doi: https://doi.org/10.1016/S0926-9851(00)00002-1.

- Slater, L. and S. Reeve, A. (2002) 'Investigating Peatland Stratigraphy and Hydrogeology Using Integrated Electrical Geophysics', 67.

- Snapp, M., Tucker-Kulesza, S. and Koehn, W. (2017) 'Electrical resistivity of mechanically stabilized earth wall backfill', Journal of Applied Geophysics, 141. doi: 10.1016/j.jappgeo.2017.04.011.

- Soupios, P. and Ntarlagiannis, D. (2017) 'Characterization and Monitoring of Solid Waste Disposal Sites Using Geophysical Methods: Current Applications and Novel Trends', in Modelling Trends in Solid and Hazardous Waste Management. Singapore: Springer, pp. 75–103.

- Soupios, P., Papadopoulos, N., Papadopoulos, I., Kouli, M., Vallianatos, F., Sarris, A. and Manios, T. (2007) 'Application of Integrated Methods in Mapping Waste Disposal Areas', Journal of Environmental Geology, 53, pp. 522–531. doi: 10.1007/s00254-007-0681-2.

- Soupios, P., Vallianatos, F., Papadopoulos, I. and Makris, J. P. (2005) 'Determination of a landfill structure using HVSR, SPT's & geoelectrical tomographies', in Agioutantis, Z. and Komnitsas, Z. (eds) Proceedings of the International Workshop in Geoenvironment and Geotechnics. Athens: Heliotopos Conferences LTD, p. 10.

- SPAQuE (2009) Banque de donnees WALSOLS. Nr 2306-001 - 'CARRIERE D'ONOZ' à Jemeppe-sur-Sambre.

- Sudibyo, M., I Fattah, E., Suhendi, C. and Rizki, R. (2019) 'Horizontal-to-vertical spectral ratio of ambient noise vibrations for local site effects estimation in ITERA', IOP Conference Series: Earth and Environmental Science, 258, p. 12041. doi: 10.1088/1755-1315/258/1/012041.

- Telford, W. M., Geldart, L. P. and Sheriff, R. E. (1990) Applied Geophysics Second Edition.

- Vargemezis, G., Tsourlos, P. I., Giannopoulos, A. and Trilyrakis, P. (2015) '3D electrical resistivity tomography technique for the investigation of a construction and demolition waste landfill site', Studia Geophysica et Geodaetica, 59. doi: 10.1007/s11200-014-0146-5.

- Verdi (1995) Audit technique du site du 'DEPOTOIR D'ONOZ' (Province de Namur).

- Vipulanandan, C., Basheer, M. and O'Neill, M. W. (1996) Recycled materials in embankments, except glass.

- Wilkinson, P. B., Loke, M. H., Meldrum, P. I., Chambers, J. E., Kuras, O., Gunn, D. A. and Ogilvy, R. D. (2012) 'Practical aspects of applied optimized survey design for electrical resistivity tomography', Geophysical Journal International. John Wiley & Sons, Ltd (10.1111), 189(1), pp. 428–440. doi: 10.1111/j.1365-246X.2012.05372.x.

- Winterstetter, A., Laner, D., Rechberger, H. and Fellner, J. (2015) 'Framework for the evaluation of anthropogenic resources: A landfill mining case study – Resource or reserve?', Resources, Conservation and Recycling, 96, pp. 19–30. doi: https://doi.org/10.1016/j.resconrec.2015.01.004.

- Yan, P., Li, Z., Li, F., Yang, Y., Hao, W. and Bao, F. (2017) 'Antarctic ice sheet thickness estimation using the H/V spectral ratio method with single-station seismic ambient noise', The Cryosphere Discussions, pp. 1–25. doi: 10.5194/tc-2017-164.

- Yannah, M., Martens, K., Van Camp, M. and Walraevens, K. (2017) 'Geophysical exploration of an old dumpsite in the perspective of enhanced landfill mining in Kermt area, Belgium', Bulletin of Engineering Geology and the Environment, pp. 1–13. doi: 10.1007/s10064-017-1169-2.

- Zhou, B. and Dahlin, T. (2003) 'Properties and effects of measurement errors on 2D resistivity imaging', Near Surface Geophysics - NEAR SURF GEOPHYS, 1, pp. 105–117. doi: 10.3997/1873-0604.2003001

9 ANNEXES

9.1 Previous investigations

9.1.1 Invasive investigations

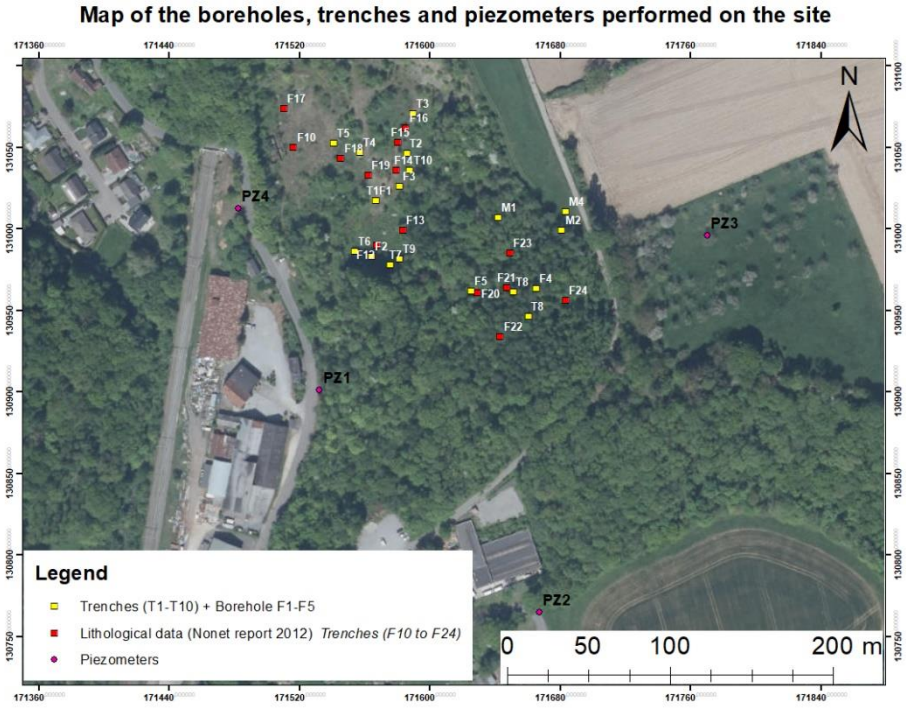

Figure 79. Map from the previous invasive investigations (Adapted from Service Public de Wallonie, 2018)

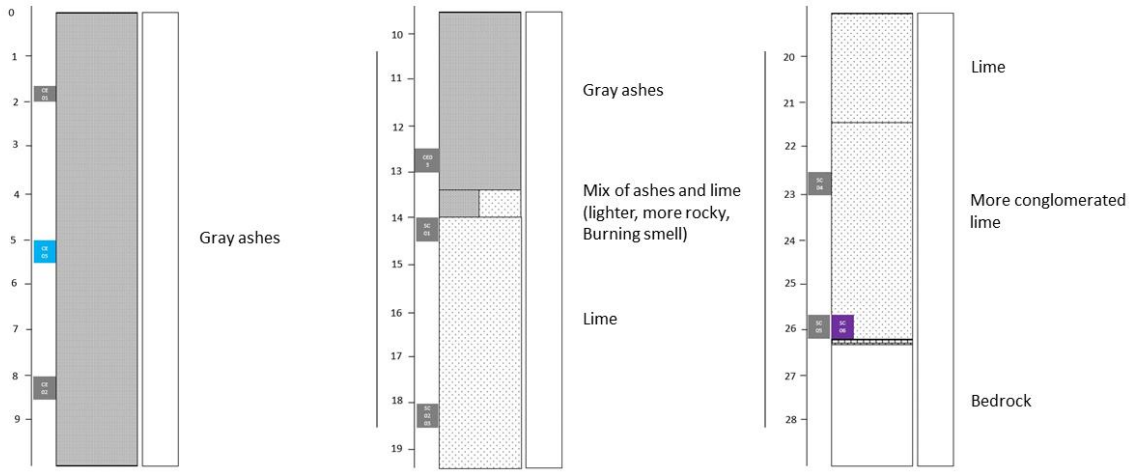

Figure 80. Borehole n° 4 (Adapted from IRCO, 2018)

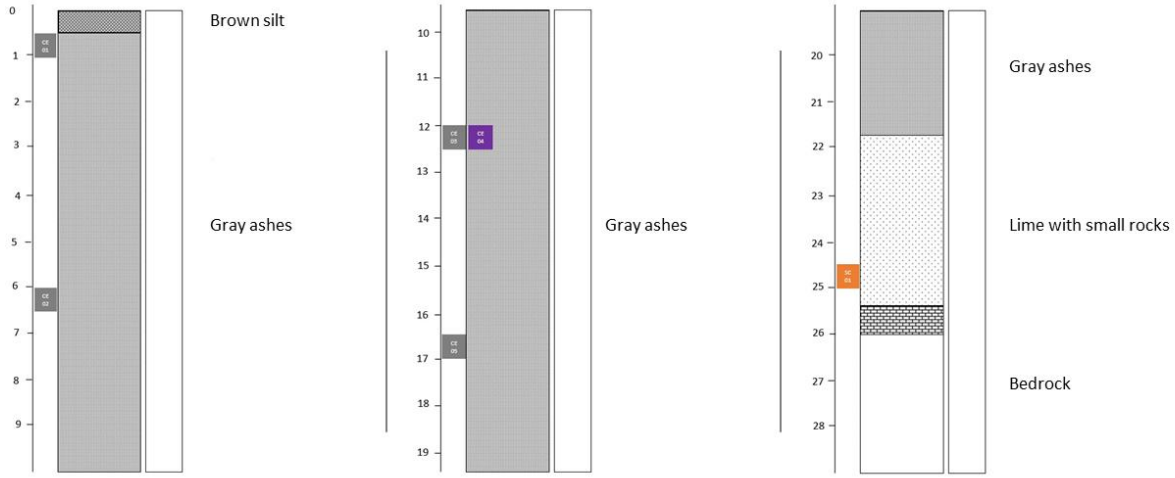

Figure 81. Borehole n° 4 (Adapted from IRCO, 2018)

9.1.2 FDEM mapping

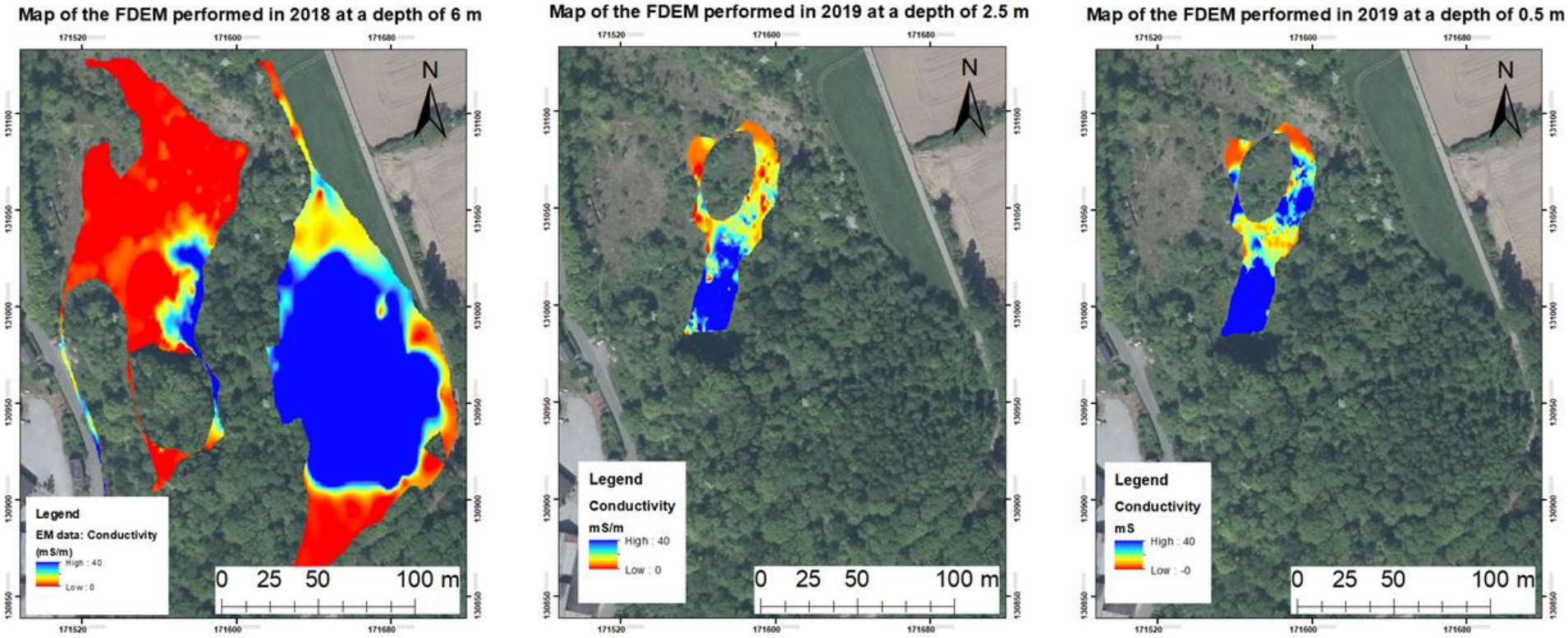

Figure 82. Map of both EM campaigns (Adapted from Caterina et al, 2019)

9.1.3 ERT profiles and corresponding results

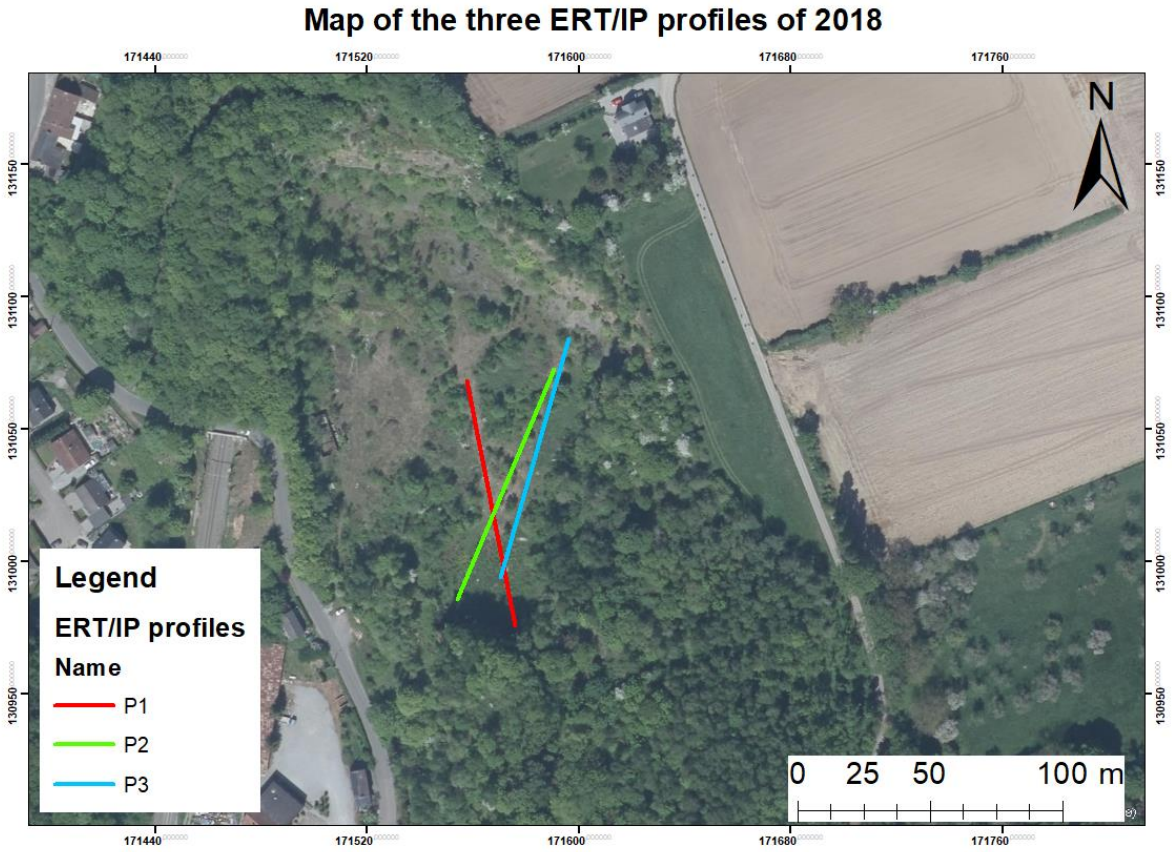

Figure 83. Map of the ERT profiles from 2018 (Adapted from Caterina et al., 2019)

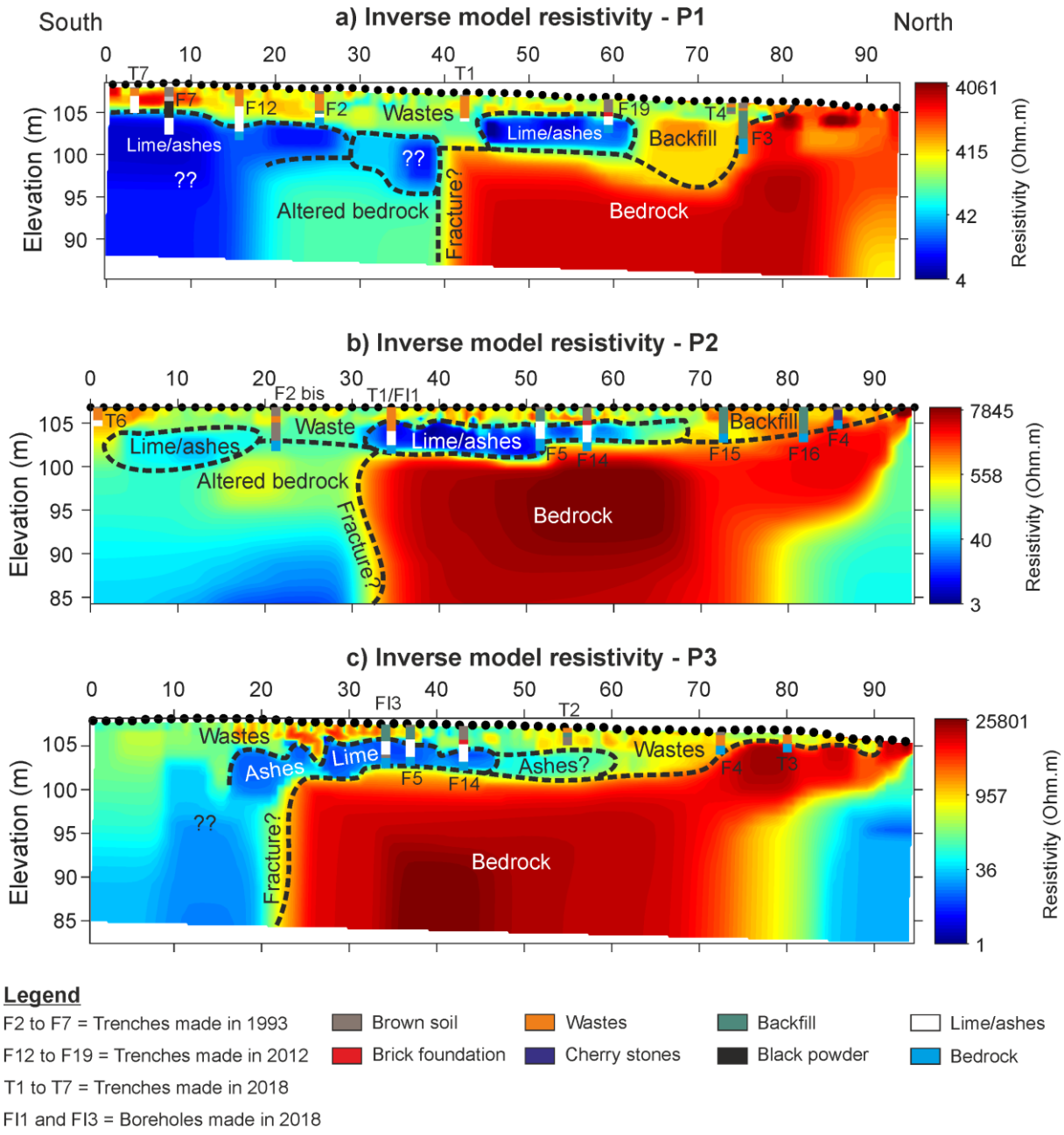

Figure 84. Results of the ERT profiles from 2018 (From Caterina et al., 2019)

9.2 Parametric analyses on the forward model

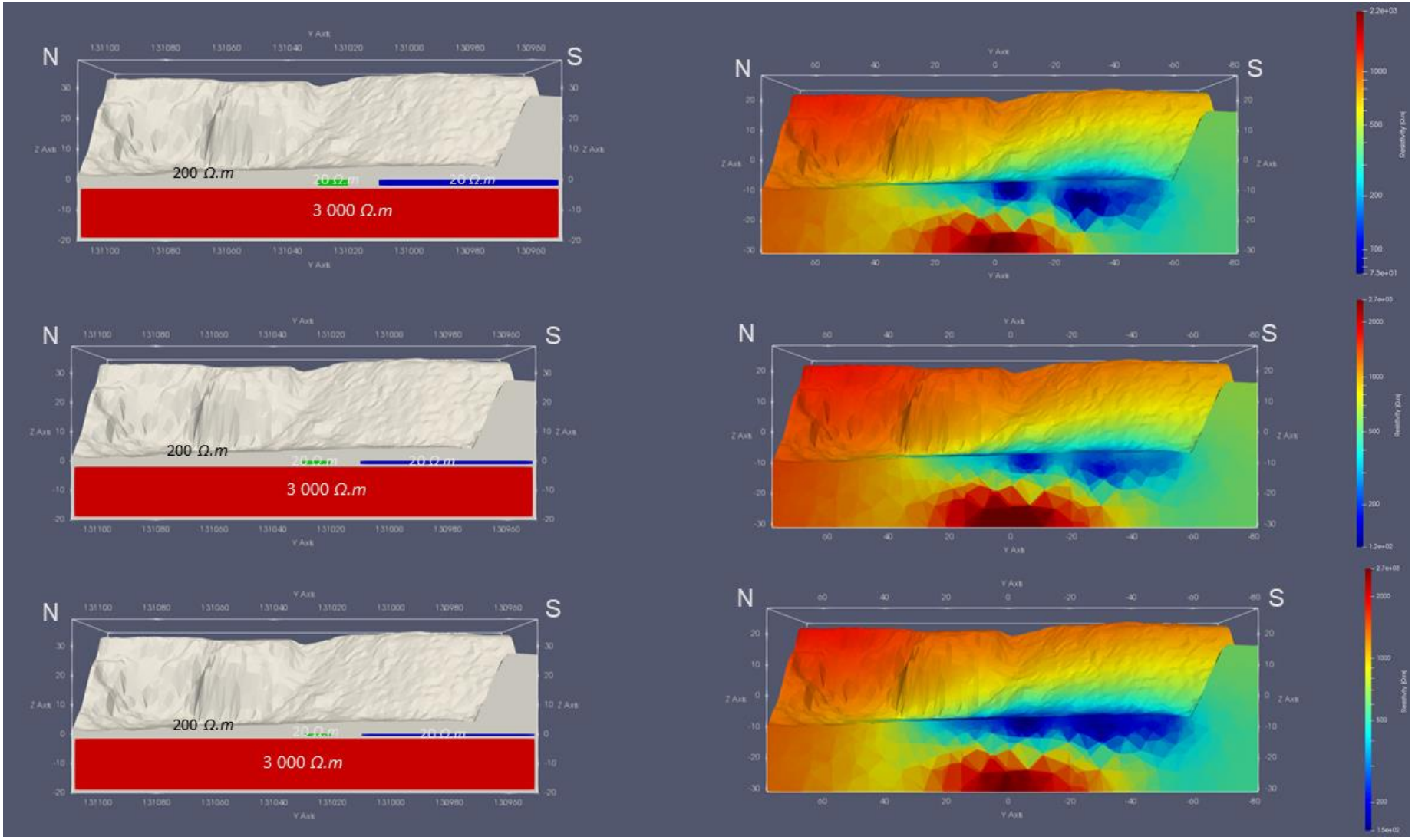

Figure 85. Results of the parametric analysis, considering a change in the thickness of the conductive layers

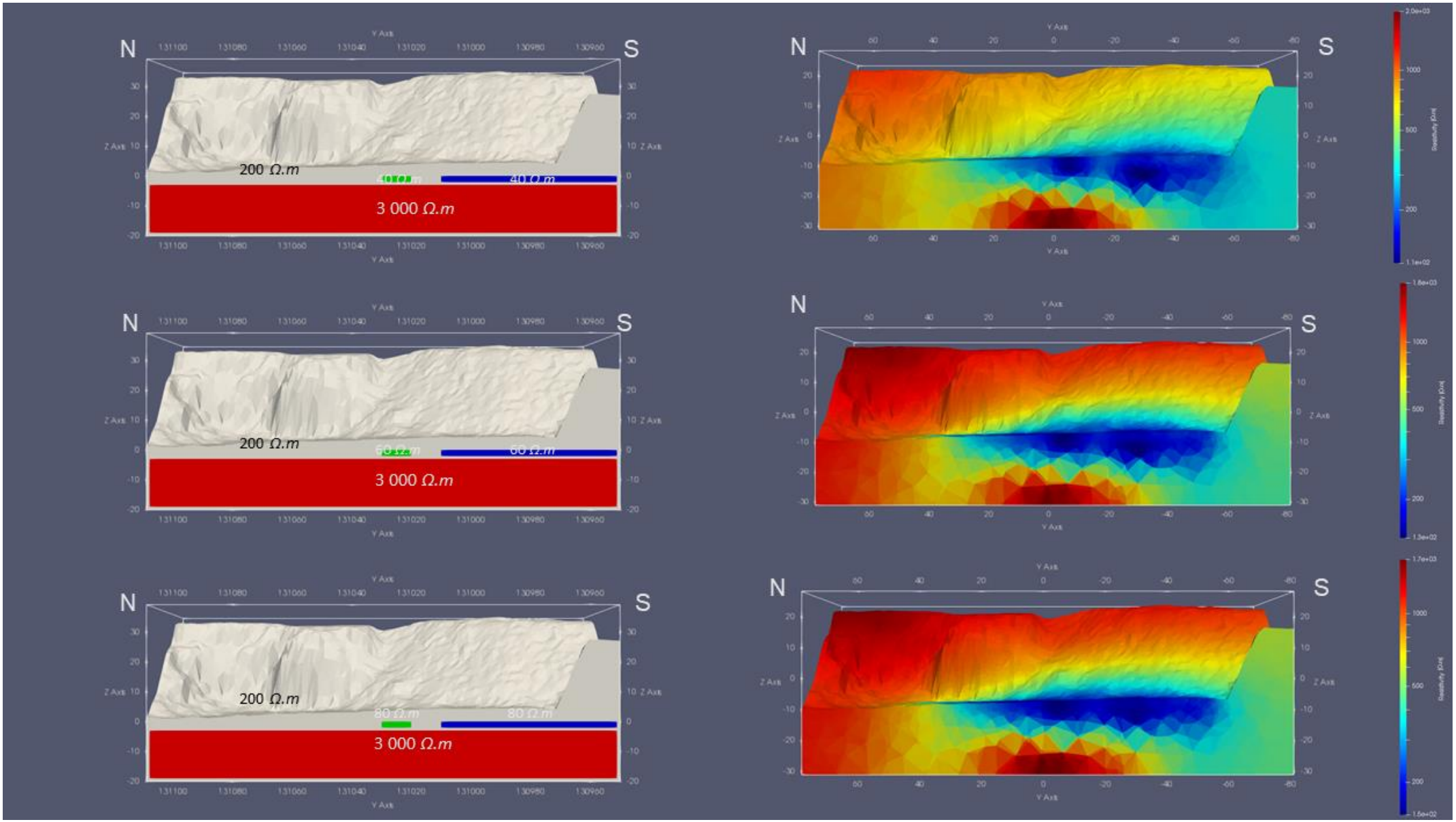

Figure 86. Results of the parametric analysis, considering a change in the resistivity of the conductive layers

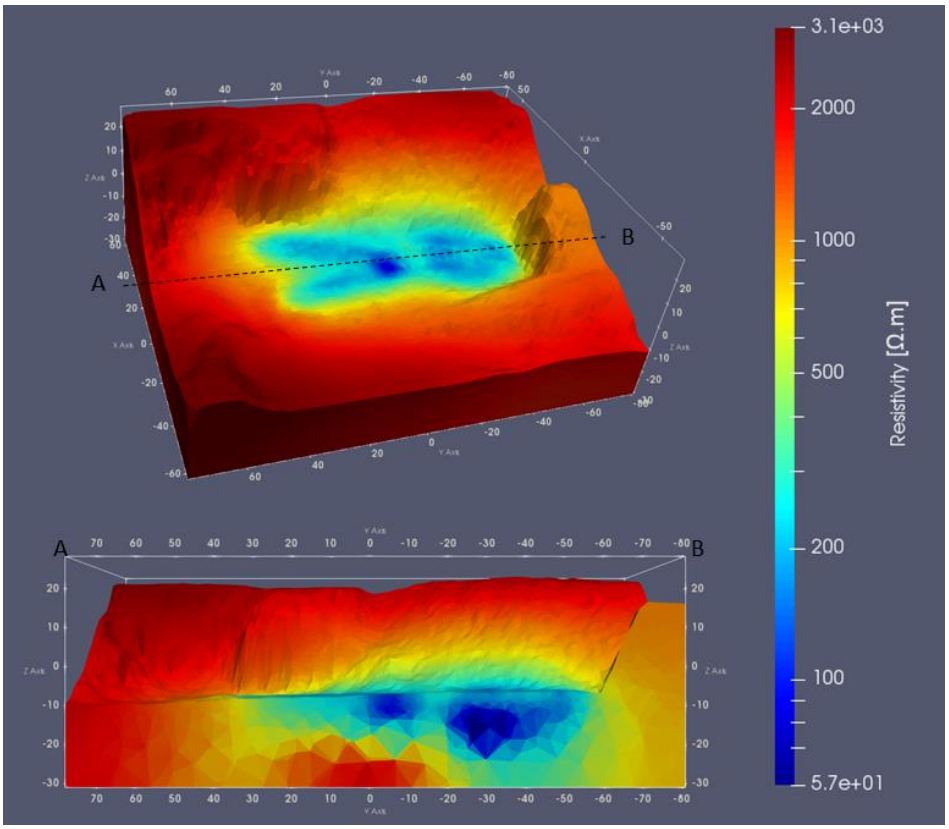

Figure 87. Resulting model for a relative weight of 0.5

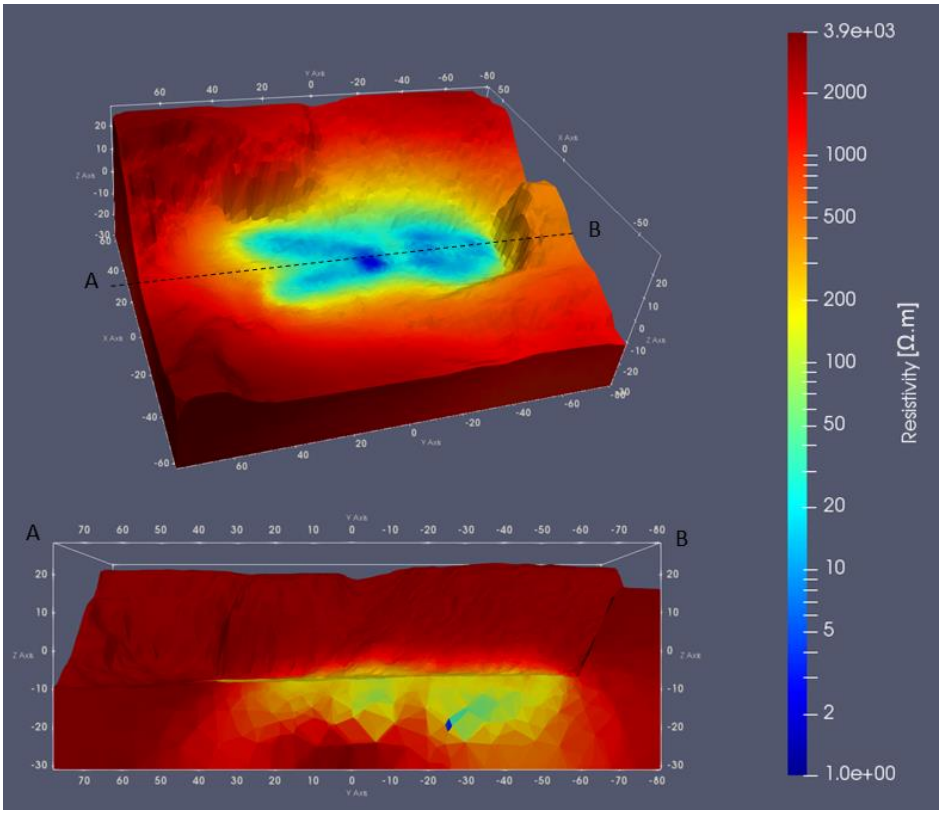

Figure 88. Resulting model for a relative weight of 0.2

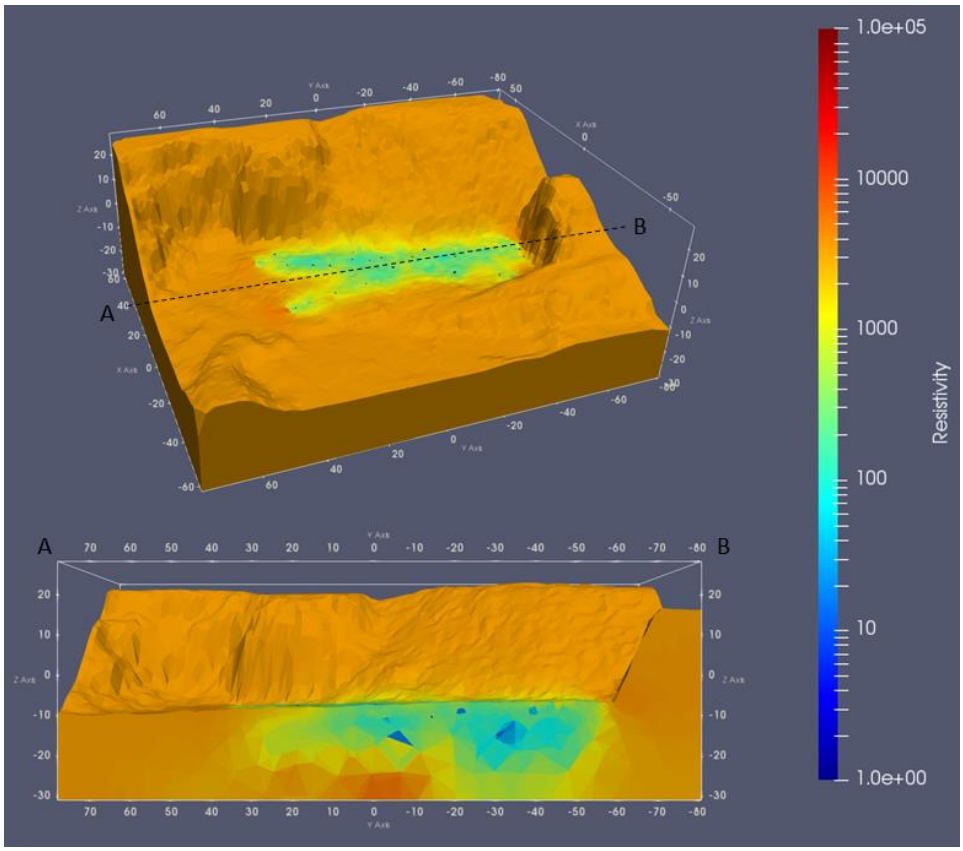

Figure 89. Resulting model for a relative weight of 0.1

9.3 Resulting DOI from the different types of inversion

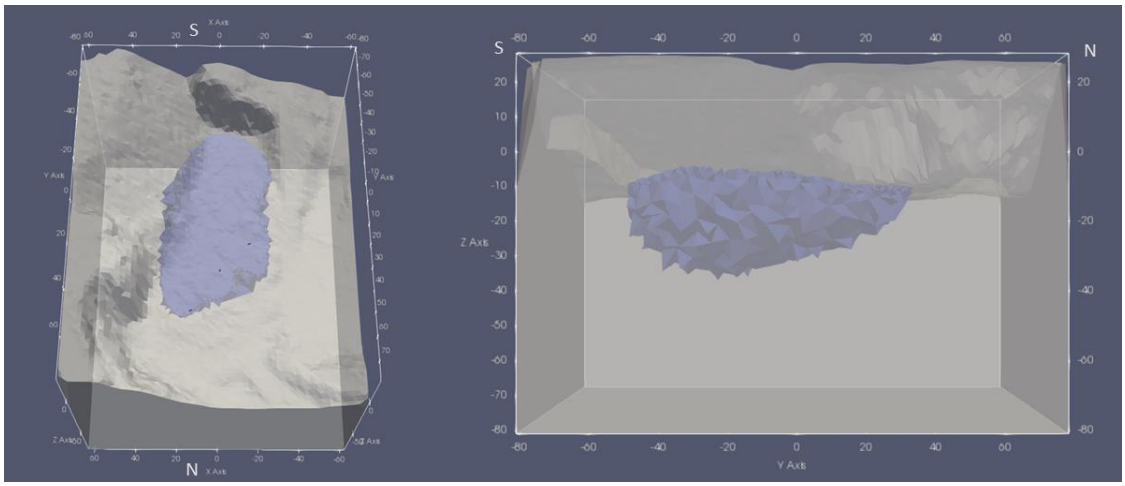

Figure 90. DOI of the smooth constrained inversion

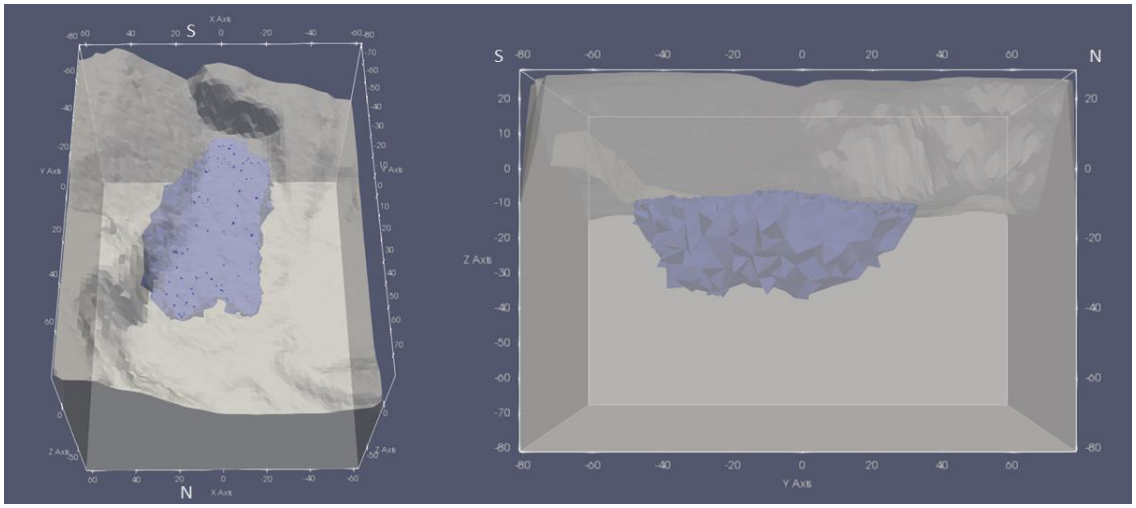

Figure 91. DOI of the inversion applied with a relative of 0.2

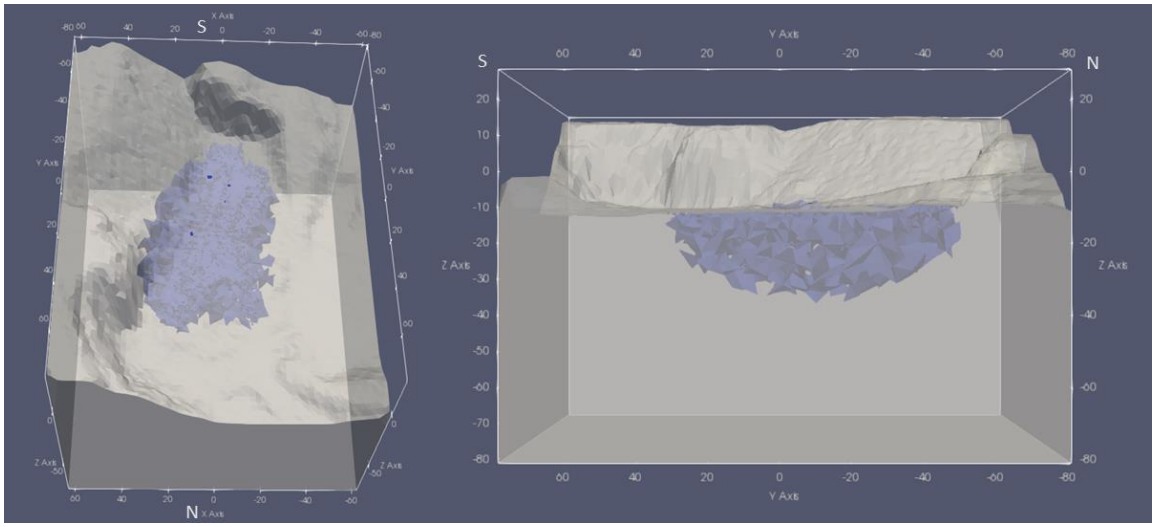

Figure 92. DOI of the blocky inversion

9.4 HVNSR maps

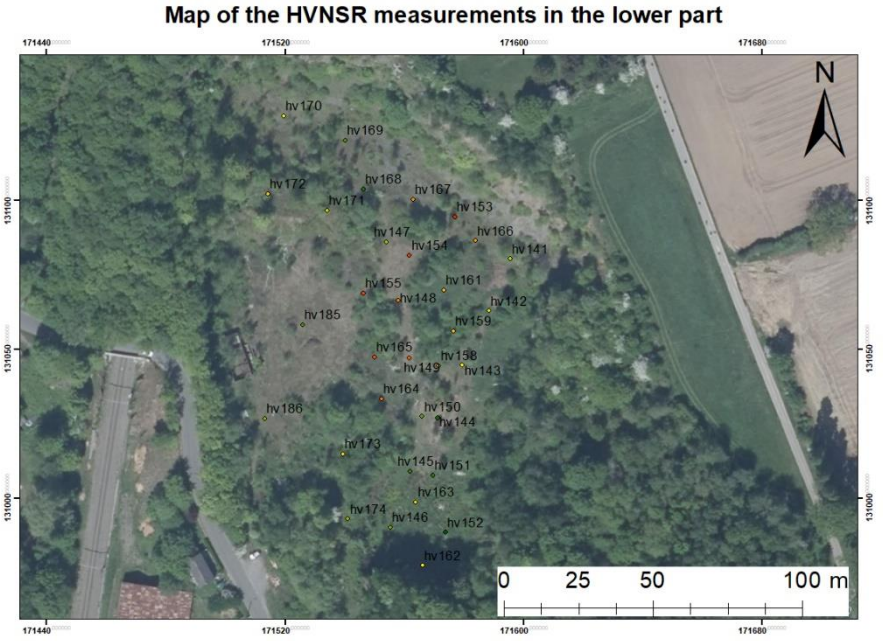

Figure 93. Map of the HVNSR measurements in the lower part of the site (Adapted from Service Public de Wallonie, 2018)

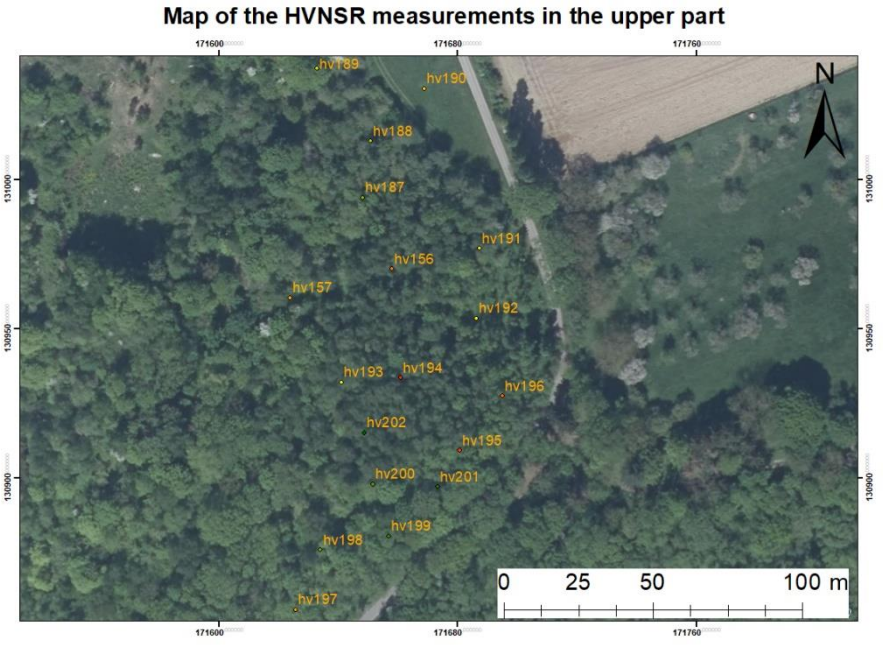

Figure 94. Map of the HVNSR measurements in the upper part of the site (Adapted from Service Public de Wallonie, 2018)

9.5 H/V graphs of the entire measurements

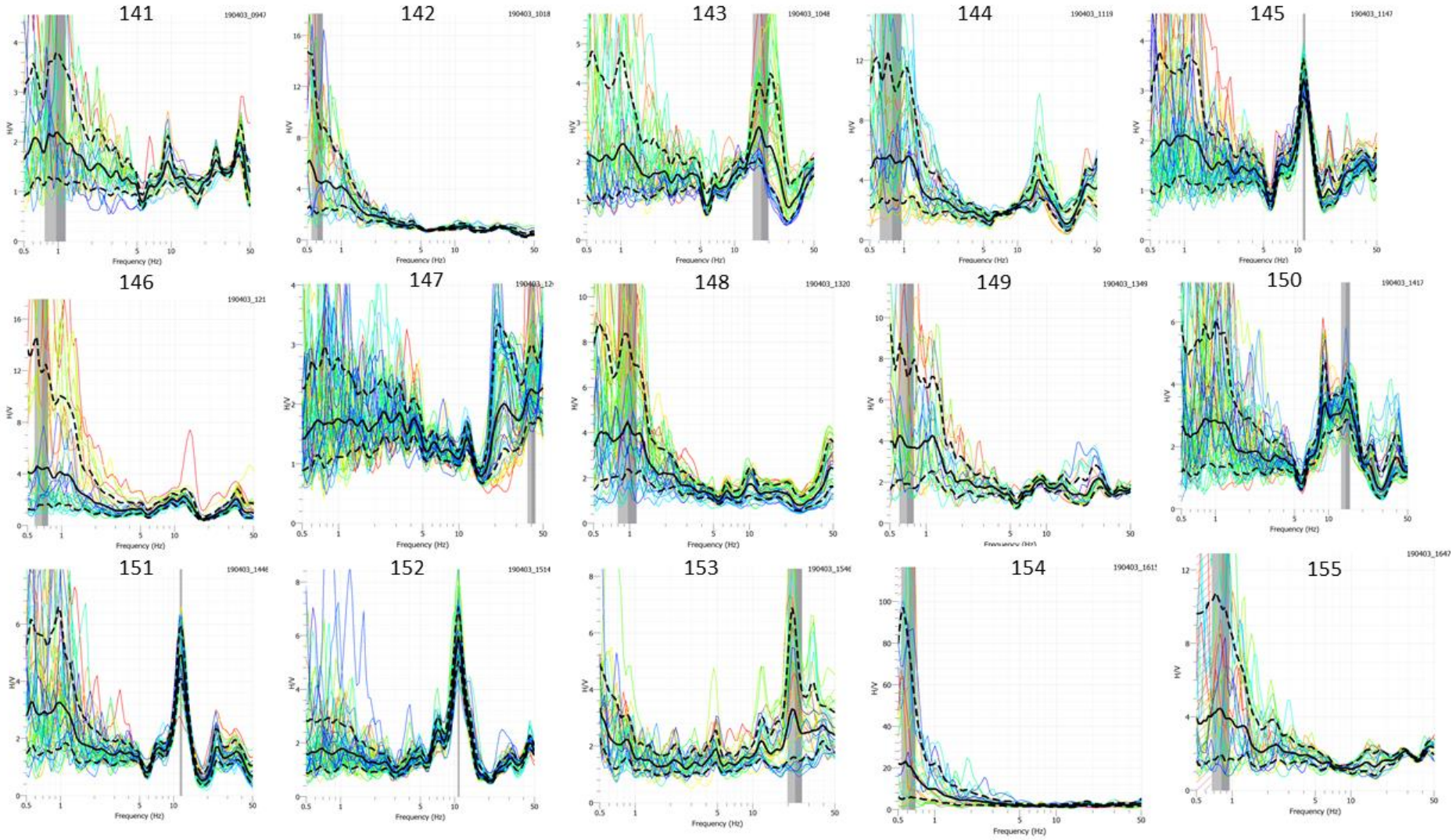

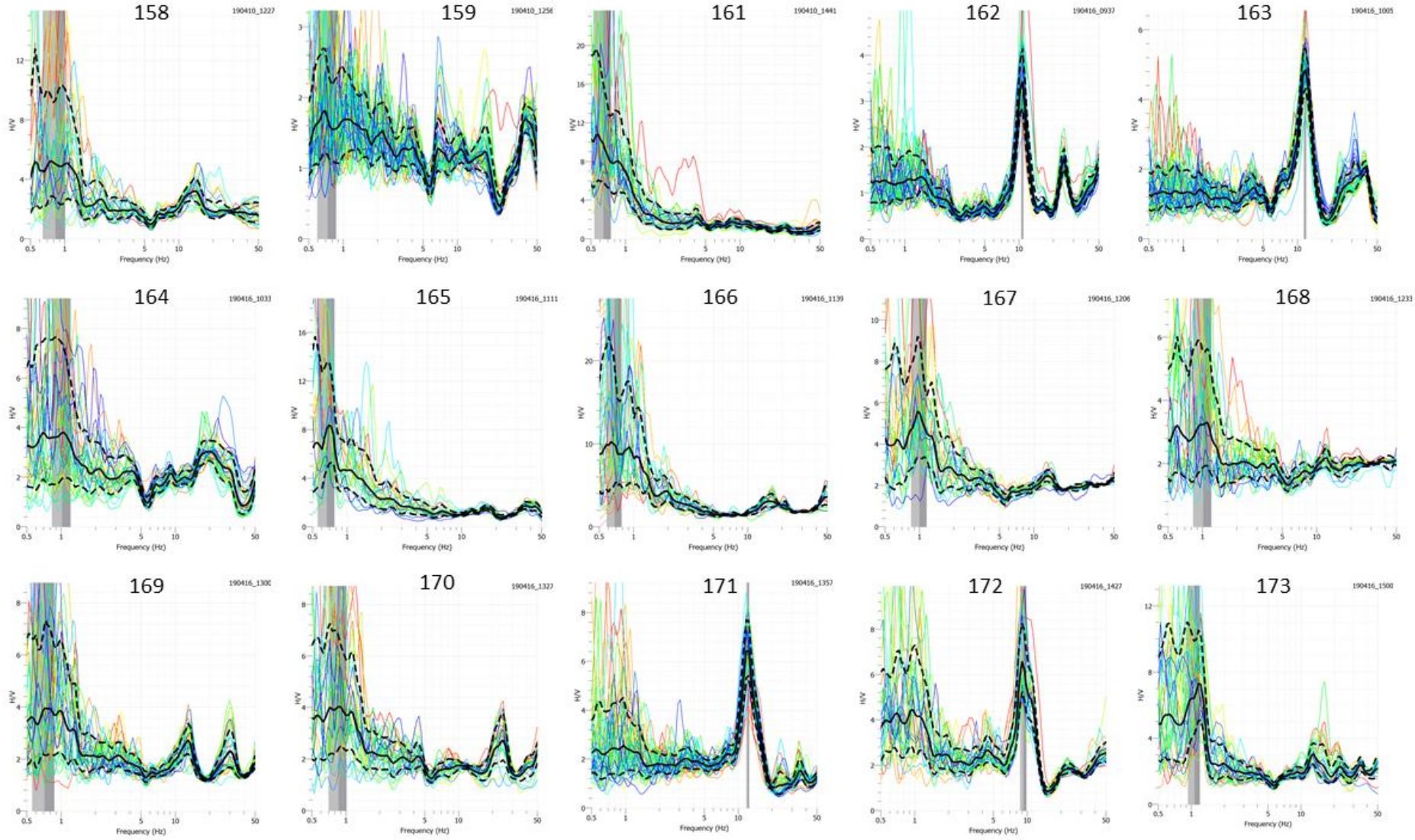
158
159
161
162
163
164
165
166
167
168
169
170
171
172
173
H/V
Frequency (Hz)

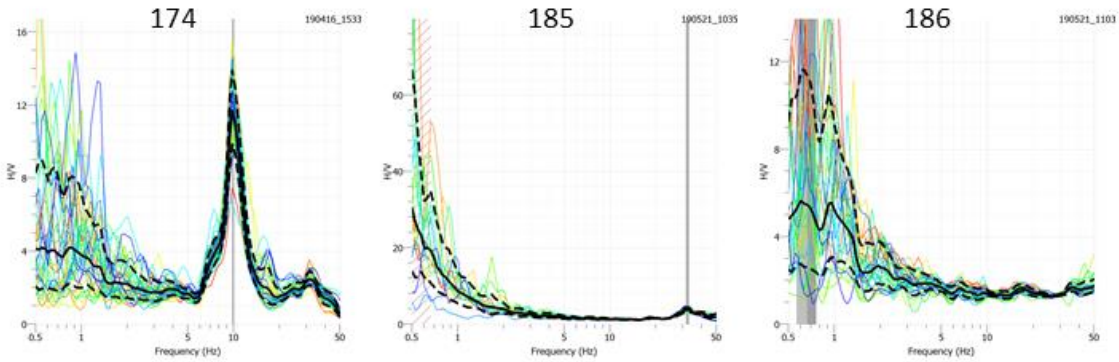

Figure 95. H/V graphs of the HVNSR measurements in the lower part of the site

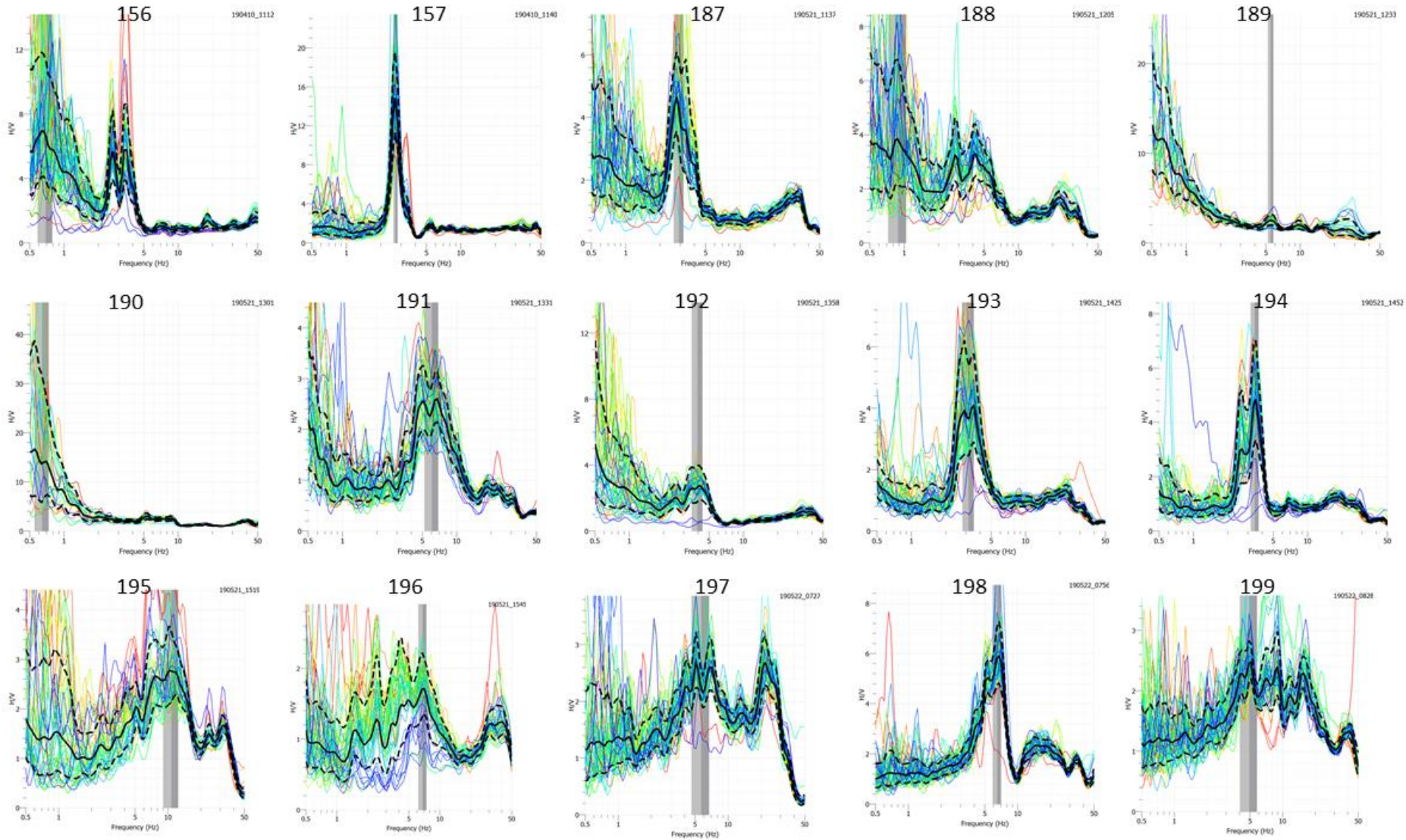
156
157
187
188
189
190
191
192
193
194
195
196
197
198
199
H/V
Frequency (Hz)

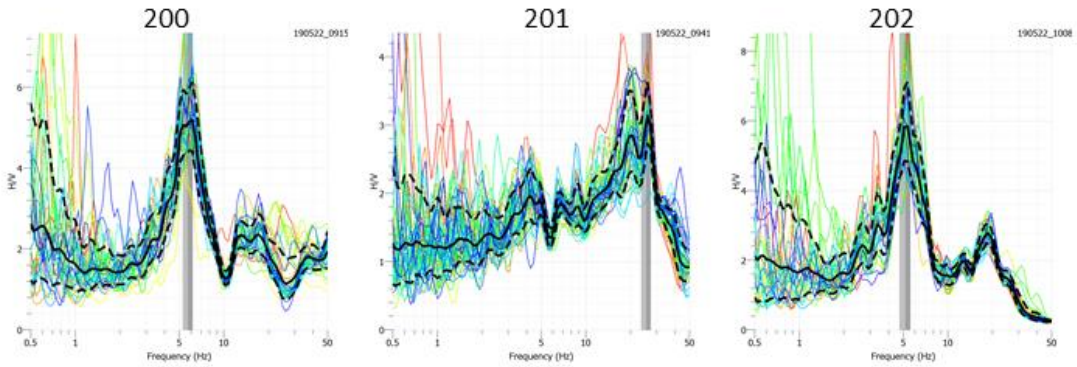

Figure 96. H/V graphs of the HVNSR measurements in the upper part of the site